

---

Doctoral Dissertations

Student Theses and Dissertations

---

Summer 2019

## Numerical modeling study of a neutron depth profiling (NDP) system for the Missouri S&T reactor

Mubarak Mohammed Albarqi

Follow this and additional works at: [https://scholarsmine.mst.edu/doctoral\\_dissertations](https://scholarsmine.mst.edu/doctoral_dissertations)



Part of the [Nuclear Engineering Commons](#)

Department: Nuclear Engineering and Radiation Science

---

### Recommended Citation

Albarqi, Mubarak Mohammed, "Numerical modeling study of a neutron depth profiling (NDP) system for the Missouri S&T reactor" (2019). *Doctoral Dissertations*. 3121.

[https://scholarsmine.mst.edu/doctoral\\_dissertations/3121](https://scholarsmine.mst.edu/doctoral_dissertations/3121)

This thesis is brought to you by Scholars' Mine, a service of the Missouri S&T Library and Learning Resources. This work is protected by U. S. Copyright Law. Unauthorized use including reproduction for redistribution requires the permission of the copyright holder. For more information, please contact [scholarsmine@mst.edu](mailto:scholarsmine@mst.edu).

NUMERICAL MODELING STUDY OF A NEUTRON DEPTH PROFILING (NDP)  
SYSTEM FOR THE MISSOURI S&T REACTOR

by

MUBARAK MOHAMMED ALBARQI

A DISSERTATION

Presented to the Faculty of the Graduate School of the  
MISSOURI UNIVERSITY OF SCIENCE AND TECHNOLOGY

In Partial Fulfillment of the Requirements for the Degree

DOCTOR OF PHILOSOPHY

in

NUCLEAR ENGINEERING

2019

Approved by:

Joseph Graham, Advisor  
Shoaib Usman  
Ayodeji Alajo  
Xin Liu  
Jaradat Safwan

© 2019

MUBARAK MOHAMMED ALBARQI

All Rights Reserved

## ABSTRACT

For decades, Neutron Depth Profiling has been used for the non-destructive analysis and quantification of boron in electronic materials and lithium in lithium ion batteries. NDP is one of the few non-destructive analytical techniques capable of measuring the depth profiles of light elements to depths of several microns with nanometer spatial resolution. The technique, however, is applicable only to a handful of light elements with large neutron absorption cross sections. This work discusses the possibility of coupling Particle Induced X-ray Emission spectroscopy with Neutron Depth Profiling to yield additional information about the depth profiles of other elements within a material. The technical feasibility of developing such a system at the Missouri University of Science and Technology Reactor (MSTR) beam port is discussed.

This work uses a combination of experimental neutron flux measurements with Monte Carlo radiation transport calculations to simulate a proposed NDP-PIXE apparatus at MSTR. In addition, the possibility of implementing an Artificial Neural Network to perform automated data analysis of NDP is presented. It was found that the performance of the Artificial Neural Network is at least as accurate as traditional processing approaches using stopping tables but with the added advantage that the Artificial Neural Network method requires fewer geometric approximations and accounts for all charged particle transport physics implicitly.

## ACKNOWLEDGMENTS

I would like to thank my advisor, Dr. Joseph Graham, for his tremendous efforts, support, patience, guidance, and encouragement that he provided and continues to provide during my research. His help was much appreciated as he has contributed significantly to guide me through the path. I would also like to thank my dissertation committee members: Dr. Shoaib Usman, Dr. Ayodeji Alajo, Dr. Xin Liu and Dr. Safwan Jaradat for their input and valued comments through the project.

I also would like to thank my family for their support through my education. My progress would not be possible without them.

Finally, I would like to thank my friends, for not only supporting me, but for providing a different perspective on both my project and life in general. Also, I would like to thank my friend Raed Alsulami; with his support I was able to complete this project.

## TABLE OF CONTENTS

	Page
ABSTRACT.....	iii
ACKNOWLEDGMENTS .....	iv
LIST OF ILLUSTRATIONS.....	vii
LIST OF TABLES.....	ix
 SECTION	
1. INTRODUCTION.....	1
1.1. NEUTRON DEPTH PROFILING.....	1
1.2. THE MISSOURI S&T RESEARCH REACTOR (MSTR).....	7
1.3. NEUTRON ACTIVATION ANALYSIS.....	13
1.4. ARTIFICIAL NEURAL NETWORKS .....	16
1.4.1. Training Algorithms.....	17
1.4.2. Activation Function.....	20
1.5. PARTICLE INDUCED X-RAY EMISSION.....	20
1.6. OUTLINE OF THE DISSERTATION.....	23
2. LITERATURE REVIEW.....	24
2.1. NEUTRON DEPTH PROFILING.....	24
2.2. ARTIFICIAL NEURAL NETWORK.....	30
2.3. PARTICLE INDUCED X-RAY EMISSION.....	31
3. NEUTRON FLUX CHARACTERIZATION OF THE BEAM PORT OF THE MISSOURI UNIVERSITY OF SCIENCE AND TECHNOLOGY REACTOR ....	33
3.1. OVERVIEW .....	33

3.2. BEAM FLUX CHARACTERIZATION USING NEUTRON ACTIVATION ANALYSIS.....	34
3.3. METHODOLOGY .....	35
3.3.1. Experimental Procedure. ....	38
3.3.2. Monte Carlo N-particle Code.....	43
3.4. RESULTS AND DISCUSSION.....	45
4. EVALUATION OF NDP CAPABILITY AT MSTR.....	50
5. AUTOMATED DATA PROCESSING OF NEUTRON DEPTH PROFILING SPECTRA USING AN ARTIFICIAL NEURAL NETWORK.....	56
5.1. OVERVIEW .....	56
5.2. METHODOLOGY .....	56
5.2.1. Modeling. ....	56
5.2.2. Artificial Neural Network. ....	57
5.3. RESULTS AND DISCUSSION.....	58
6. NIXE: NEUTRON DEPTH PROFILING COUPLED WITH PARTICLE INDUCED X-RAY EMISSION .....	64
6.1. OVERVIEW .....	64
6.2. THEORY .....	65
6.3. METHODOLOGY .....	71
6.3.1. Monte Carlo Radiation Transport.....	71
6.3.2. Data Analysis. ....	71
6.4. RESULT AND DISCUSSION .....	73
7. CONCLUSIONS .....	79
BIBLIOGRAPHY.....	82
VITA.....	92

## LIST OF ILLUSTRATIONS

Figure	Page
1.1. Schematic of a Neutron Depth Profiling (NDP) Apparatus.....	4
1.2. NDP Process. ....	5
1.3. Schematic of NDP System of Ohio State University.....	5
1.4 Schematic of Penn State Reactor Beam Port #4 and NDP Chamber.....	6
1.5. Outside View of Ohio State University NDP Instrument. ....	6
1.6. Side View of the MSTR.....	9
1.7. MSTR Core Configuration 128 W.....	10
1.8. MSTR Core Configuration 120 W.....	10
1.9. Legend Description of Core Configuration. ....	11
1.10. The MSTR Beam Port Schematic.....	12
1.11. Neutron Capture Reaction and Emission of Prompt and Delayed Neutrons. ....	15
1.12. Example of a Simple Artificial Neural Network (ANN). ....	18
1.13. PIXE Spectrum. ....	21
1.14. Particle Induced X-Ray Emission Process.....	22
1.15. (a) Charged Particle Impact Ionization of a K-Shell Electron (b) X-Ray Emission and (c) Auger Electron Emission. ....	22
2.1. Illustration of NIST Cold Neutron Depth Profiling Chamber. ....	26
2.2. Schematic of Neutron Depth Profiling-Time of Flight (TOF-NDP). ....	27
2.3. Li Profile in LiFePO <sub>4</sub> /Graphite Cell Measured with NDP.. ....	29
2.4. Illustration of an In Situ NDP Apparatus for Studying Li Ion Batteries. ....	29
3.1. Gold Foil Positions.. ....	43

3.2. Top Down Cross Section of the MSTR. ....	46
3.3. The Total Neutron Fluence per Activation Foil Normalized by the Average Fluence for all Foils.....	48
4.1. Basic Design of the NDP Instrument.....	51
4.2. Alpha Energy Spectrum of the SRM-93a NIST Standard. ....	52
4.3. BPSG Alpha Energy Spectrum.....	53
4.4. Concentration of BPSG as a Function of Depth Obtained from MCNP. ....	54
5.1. Artificial Neural Network Design for Analyzing <sup>10</sup> B NDP Spectra. ....	58
5.2. The Alpha Energy Spectrum of NIST Standard SRM-2137. ....	59
5.3. Crossplot of Predicted and Actual Datasets of the Boron Samples for Training, Validation, Testing, and all Datasets. ....	60
5.4. Mean Squared Error Values During Training.....	61
5.5. The Boron Depth Profile for SRM-2137.. ....	62
6.1. Depiction of the NDP and PIXE Acquisition Process. ....	66
6.2. Alpha Spectrum from Boron NDP of a Multilayer Glass Specimen. ....	74
6.3. K-Shell Coincidence Count Rate for (a) Si (b) P (c) Na and (d) O. ....	76
6.4. Depth Profile of (a) Si (b) P (c) Na and (d) O. ....	77

**LIST OF TABLES**

Table	Page
1.1. Summary of the Light-Element That Could be Used for NDP.....	7
1.2. Common Activation Function.....	19
3.1. Gold Foil Masses. ....	38
3.2. Cross Section Parameters of 25 $\mu\text{m}$ Thick Au Foil and a 1 mm Thick Cd Filter. ....	40
3.3. Experimental and MCNP Neutron Flux at the Gold Foils.....	47
6.1. Possible Nuclear Reactions for NDP Analysis. ....	65
6.2. Sample Thickness and Composition.....	72

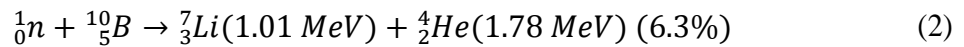
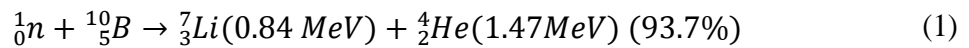
# 1. INTRODUCTION

## 1.1. NEUTRON DEPTH PROFILING

Neutron Depth Profiling is a non-destructive technique for characterizing the depth profile of certain light elements such as  $^{10}\text{B}$  and  $^6\text{Li}$  in a material. NDP is one of a few non-destructive techniques that can accurately measure boron concentration in the surface of a material [1]. It is an important technique for measuring the concentration and distribution of light elements in several technologically important materials, along with Auger Electron Spectroscopy (AES), Secondary Ion Mass Spectroscopy (SIMS), and Rutherford Backscattering Spectrometry (RBS) [2, 3].

Auger Electron Spectroscopy has good spatial resolution and sensitivity to low-Z elements but is limited to nanometer depths (without ion milling, which modifies the surface being analyzed). Secondary Ion Mass Spectroscopy is standard method for characterizing elemental depth profiles but it requires sputtering the surface and is therefore a destructive technique. Rutherford Backscattering Spectrometry is a non-destructive technique capable of measuring heavy element depth profiles to micron or tens of micron ranges though it relatively insensitive to light elements. A technique related to RBS is Elastic Recoil Detection Analysis (ERDA). Light element analysis is substantially easier with ERDA though detection limits are likewise high. NDP offers the advantages of nanometer depth resolution, range of depth profile, low detection limits (i.e. high sensitivity), without modifying the surface of the sample. That said, most NDP analysis is specific to a small number of light elements. In NDP, a well-collimated beam of low energy neutrons passes through a thin sample in vacuum.

Some light elements, such as boron and lithium, contain naturally abundant isotopes with large cross sections for thermal neutron absorption ( $^{10}\text{B}$  and  $^6\text{Li}$ ). When these reactions produce a light charged particle (e.g. a proton or an alpha) the depth of the interaction can be determined by NDP. For example, in neutron capture by  $^{10}\text{B}$ , an  $\alpha$  particle and  $^7\text{Li}$  ion are emitted. These particles can be emitted with two possible energies since the  $^7\text{Li}$  nucleus can be formed in either the ground state or an excited state. Ignoring energy loss mechanisms, the target nuclide is uniquely identified from the Q-value of its reaction. This Q-value can be inferred from the measured kinetic energy of either emitted charged particle. The reactions for boron-10 are:



Reactions (1) and (2) have branching ratios of 93.7% and 6.3%, respectively. Either of these charged particles, emitted near the surface, may escape before being stopped. The range of these particles depends on their energy, mass, charge, and the stopping power of the matrix. The charged particle loses energy on its way out of the specimen, primarily through electronic energy loss processes, though nuclear stopping becomes the dominant contributor to the energy loss at low energies. Ignoring straggling effects, distance traveled and energy lost are in an essentially one-to-one correspondence. The elemental depth profile can be determined from the energy loss of the charged particle and knowledge of the material's stopping power through the following relation based on the Continuous Slowing down Approximation (CSDA).

The difference between the reaction Q-value(s) and measured particle kinetic energy gives the energy loss. From energy loss, one can infer the depth of the nuclear

reaction and therefore the concentration depth profile of the element of interest. To prevent the particle from losing the rest of its energy after leaving the sample surface and before hitting the detector, the sample and the detector are kept under vacuum. Figure 1.1 shows a schematic view of a standard NDP apparatus.

$$x = \int_{E(x)}^{E_0} \frac{1}{S(E)} dE \quad (3)$$

Here,  $E_0$  is the particle's initial energy,  $x$  is the particle's path-length in the material,  $S(E)$  is the stopping power of the matrix, and  $E(x)$  is the remaining particle energy which is deposited in the detector after leaving the sample surface [4]. Note that this Equation does not take into account straggling effects and is therefore only accurate for high energy charged particles. To account for stopping in the target matrix, stopping tables or numerical calculations of the stopping power are generally used.

Charged particles travel a distance on the order of microns in most condensed matter. This range depends on the type of emitted charged particle and its energy as well as the stopping power of the stopping medium. The energy loss of the particles after leaving the sample is measured with a charged particle detector (see Figure 1.2).

Today, NDP systems are applied in a small number of different nuclear research reactor facilities around the world. For example, there are NDP facilities in the U.S. at the National Institute of Standards and Technology (NIST), Texas A&M, University of Texas-Austin, Penn State University (Figure 1.4), and Ohio State University (Figures 1.3 and 1.5) [5-7]. Although many nuclei undergo charged-particle-producing neutron-nuclear interactions, cross sections for these interactions, and therefore detection limits span several orders of magnitude for thermal neutrons.

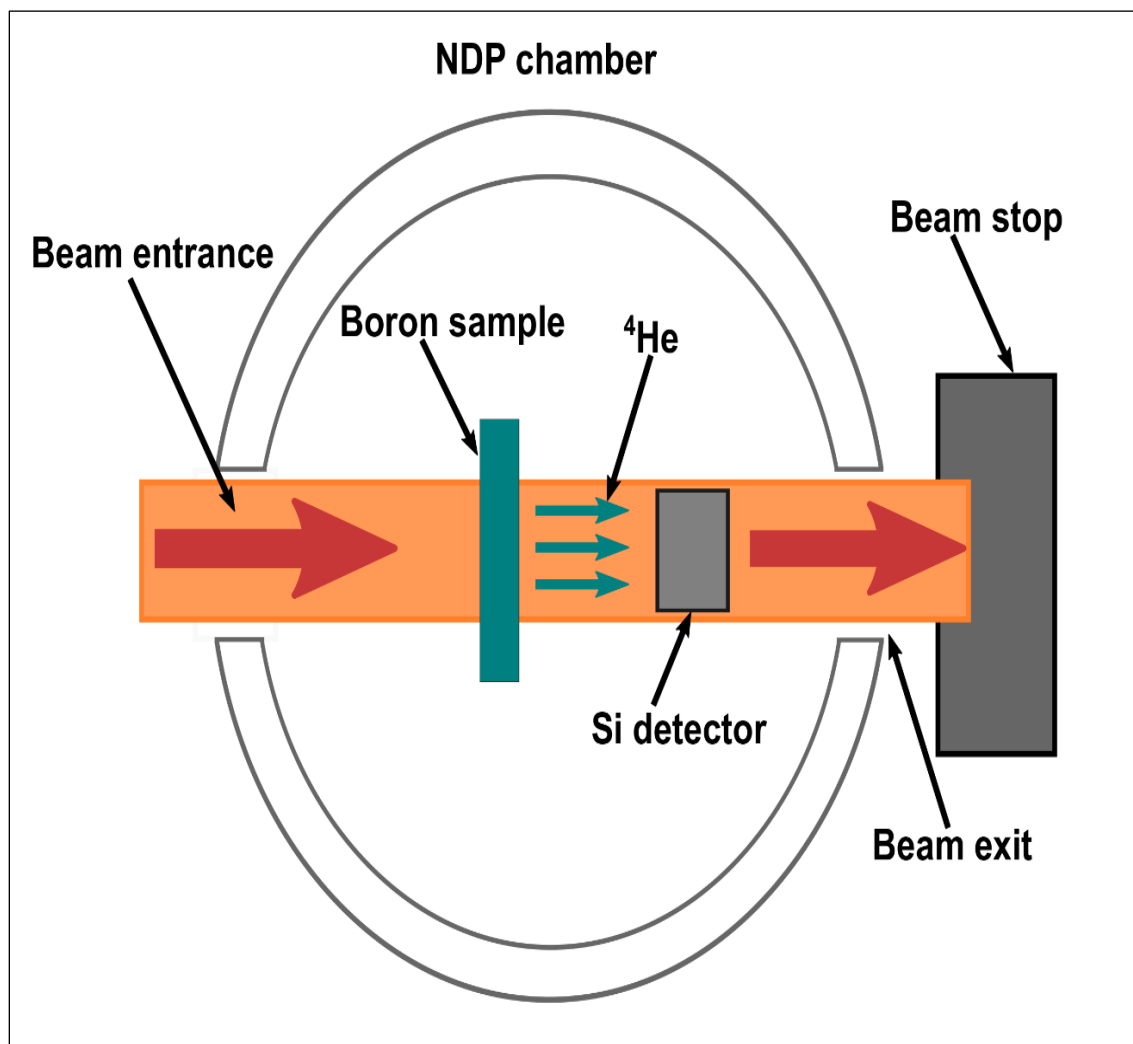


Figure 1.1. Schematic of a Neutron Depth Profiling (NDP) Apparatus.

Therefore, only a few nuclei with especially large cross section have been commonly used for NDP analysis. Table 1.1 has a list of these isotopes. Elements up to and including boron are generally well suited for NDP. Nitrogen and oxygen can be measured with NDP but have higher detection limits. Therefore, NDP analysis for those elements is only possible with longer acquisition times, a strong neutron source and when their concentration is high in the material.

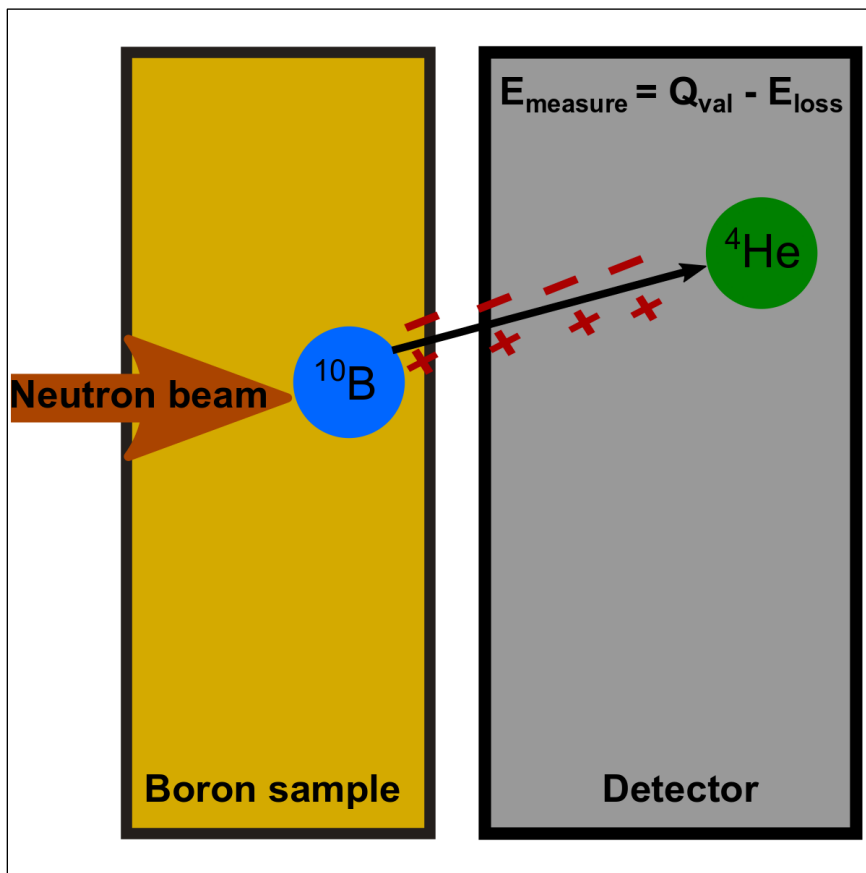


Figure 1.2. NDP Process.

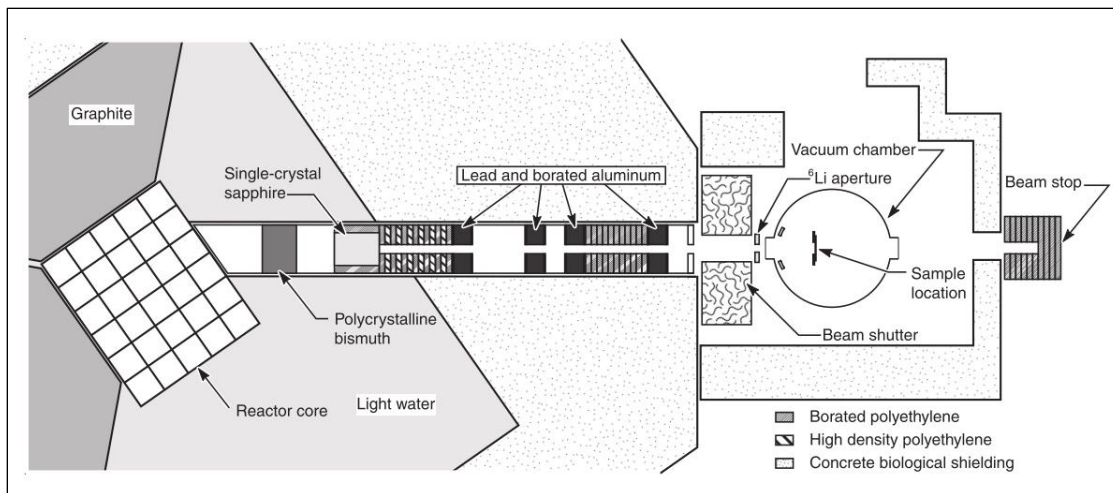


Figure 1.3. Schematic of NDP System of Ohio State University (from [8]).

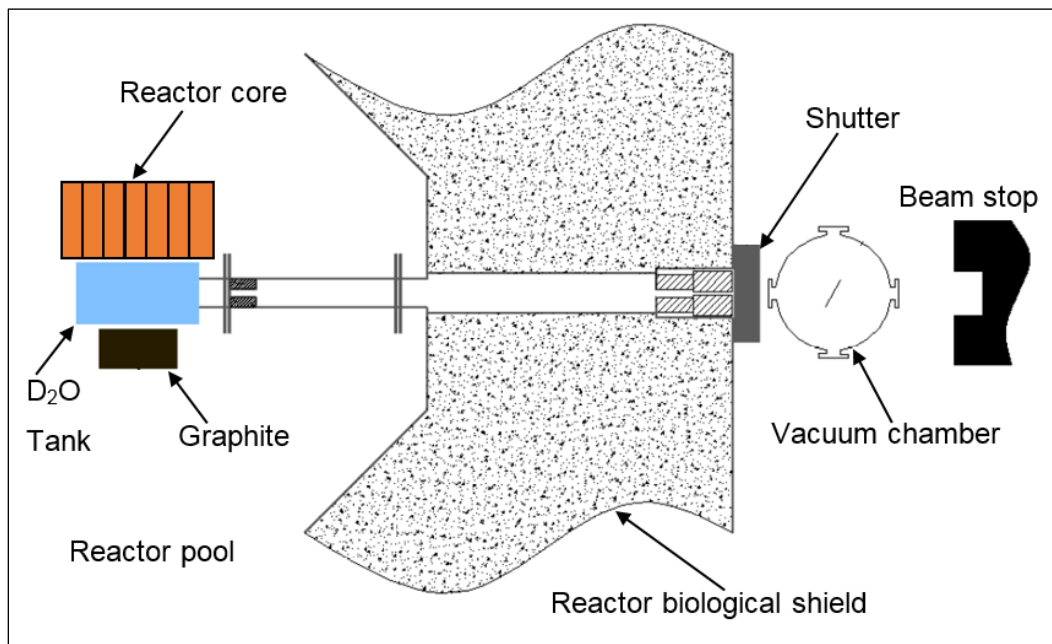


Figure 1.4. Schematic of Penn State Reactor Beam Port #4 and NDP Chamber (from [7]).



Figure 1.5. Outside View of Ohio State University NDP Instrument (from [8]).

Table 1.1. Summary of the Light-Element That Could be Used for NDP.

Nuclide	Reaction	Cross section (barns)	Energy of emitted particles (keV)		% Abundance or (atoms/mCi)	Detection Limit (atoms/cm <sup>2</sup> )
<sup>3</sup> He	<sup>3</sup> He(n,p) <sup>3</sup> H	5333	572	191	0.00014	4.2×10 <sup>14</sup>
<sup>6</sup> Li	<sup>6</sup> Li(n,α) <sup>3</sup> H	940	2055	2727	7.5	2.4×10 <sup>15</sup>
<sup>7</sup> Be	<sup>7</sup> Be(n,p) <sup>7</sup> Li	48000	1438	207	(2.5×10 <sup>14</sup> )	4.7×10 <sup>13</sup>
<sup>10</sup> B	<sup>10</sup> B(n,α) <sup>7</sup> Li	3837	1472(94%) 1776(6%)	840(94%) 1013(6%)	19.9	5.9×10 <sup>14</sup>
<sup>14</sup> N	<sup>14</sup> N(n,p) <sup>14</sup> C	1.83	584	42	99.6	1.2×10 <sup>18</sup>
<sup>17</sup> O	<sup>17</sup> O(n,α) <sup>14</sup> C	0.24	1413	404	0.038	9.4×10 <sup>18</sup>
<sup>22</sup> Na	<sup>22</sup> Na(n,p) <sup>22</sup> Ne	31000	2247	103	(4.4×10 <sup>15</sup> )	7.3×10 <sup>13</sup>
<sup>33</sup> S	<sup>33</sup> S(n,α) <sup>30</sup> Si	0.19	3081	411	0.75	1.2×10 <sup>19</sup>
<sup>35</sup> Cl	<sup>35</sup> Cl(n,p) <sup>35</sup> S	0.49	598	17	75.8	4.6×10 <sup>18</sup>
<sup>40</sup> K	<sup>40</sup> K(n,p) <sup>40</sup> Ar	4.4	2231	56	0.012	5.1×10 <sup>17</sup>
<sup>59</sup> Ni	<sup>59</sup> Ni(n,α) <sup>56</sup> Fe	12.3	4757	340	(1.3×10 <sup>20</sup> )	1.8×10 <sup>17</sup>

## 1.2. THE MISSOURI S&T RESEARCH REACTOR (MSTR)

The Missouri University of Science and Technology Research Reactor (MSTR) is an open pool research reactor that operates at a maximum thermal power of 200 kW with a corresponding maximum flux of about  $5 \times 10^{12} \text{ cm}^{-2} \text{ s}^{-1}$  [9] (see Figure 1.6). The MSTR has been in operation since 1961 and has been used in different research projects spanning a range of subjects including materials science, nuclear medicine, reactor

physics and radiochemistry. MSTR is routinely used for Neutron Activation Analysis (NAA), in-core irradiations, criticality experiments, and measurements of the temperature and void coefficients of reactivity [9]. Recently the reactor has also been used for neutron spectroscopy and neutron tomography measurements [10, 11]. The reactor also contains an internet accessible hot-cell facility for conducting high dose irradiation and activation experiments [12].

The MSTR uses light-water moderation and natural convection cooling. The fuel is 19.75% enriched MTR plate fuel composed of  $U_3Si_2$  dispersed in an Al matrix and clad in Al. The current reactor core configuration comprises 4 control rods, 12 full fuel elements, and 3 half-fuel elements. The MSTR has four control rods: three of them are shim (safety) rods while the fourth is a regulating rod. The shim rods are composed of stainless steel with a 1.5% natural boron addition and are used for coarse reactivity control and to shut down the reactor. The regulating rod is made of stainless steel (SS304) and is used for finer reactivity insertions and to automatically maintain steady state reactor power. A plutonium–beryllium (PuBe) neutron source is used for low-power and subcritical operations.

The MSTR has a  $1.1 \times 1.1 \times 1.75$  m graphite thermal column assembly located to the rear of the reactor core. The MSTR core can be positioned close to the thermal column, in which case it is in thermal-column-reflector mode (T mode). On the other hand, when water surrounds the core on all sides it is in water-reflector mode (W mode) [9, 13, 14]. Throughout the history of MSTR, the fuel has been reconfigured many times starting with core configuration 101 W and followed with increasing configuration numbers for each mode.

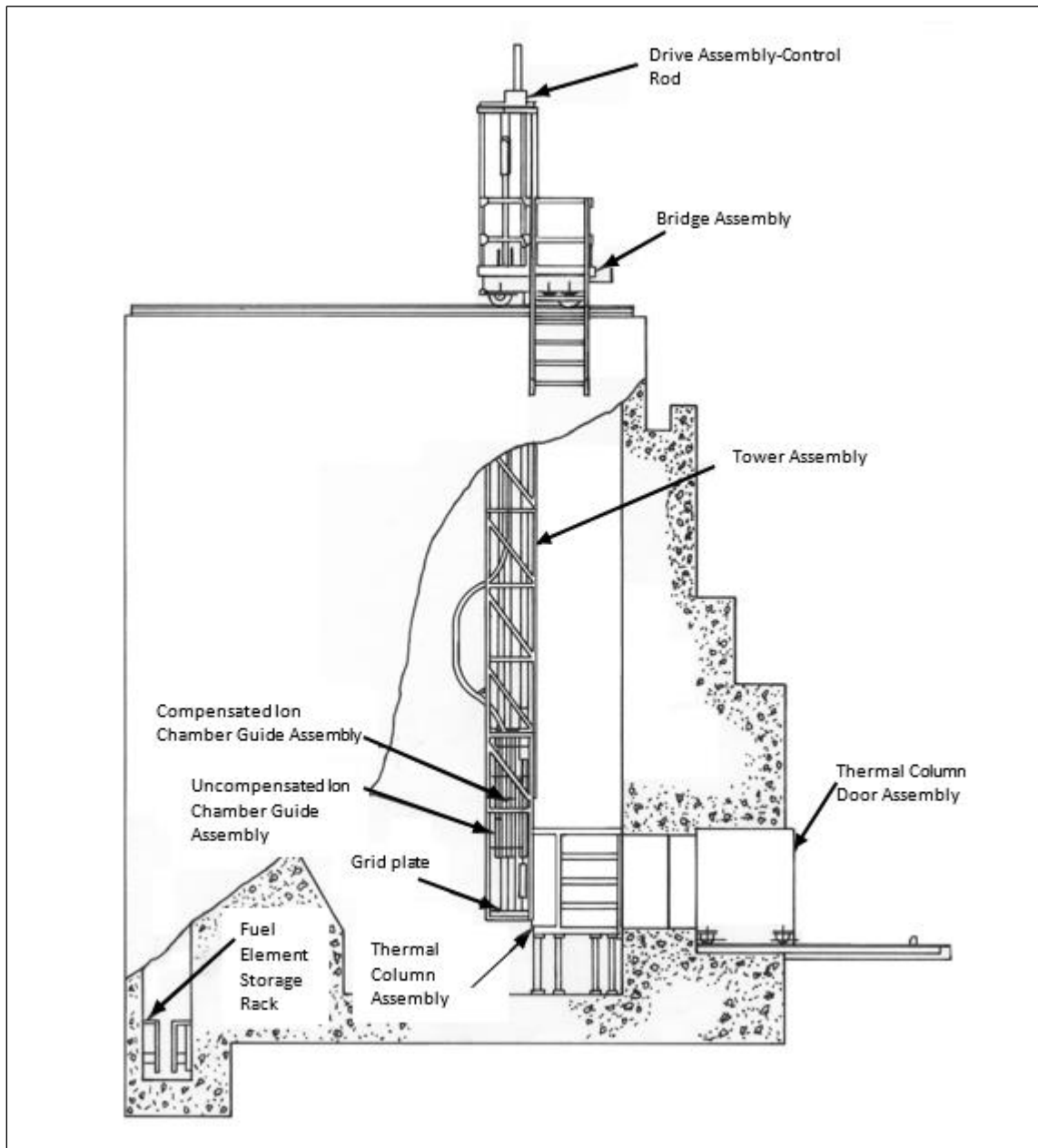


Figure 1.6. Side View of the MSTR.

The current configuration, 128 W, and the previous configuration, 120 W, are shown in Figures 1.7 and 1.8 below. The key in Figure 1.9 indicates the meaning of each colored rectangle.

	1	2	3	4	5	6	7	8	9
A					S				
B					HR2		F2		
C				F4	C4	F17	C1	F5	
D				F16	F13	F11	F14	F18	
E				F8	C5	F15	C2	F9	
F				CRT	HF1	HC	HF2	BRT	

Figure 1.7. MSTR Core Configuration 128 W.

	1	2	3	4	5	6	7	8	9
A									
B						S			
C					C4	F5	F1	F17	
D				F4	F8	F14	C1	F10	F2
E				F9	C3	F12	C2	F7	F3
F				CRT	F15	HC	F13	BRT	F6

Figure 1.8. MSTR Core Configuration 120 W.

The core irradiation facilities in the MSTR include bare and cadmium lined rabbit pneumatic tubes for lower activity samples, a bare pneumatic rabbit tube connected to the

hot cell for high activity samples. In these facilities, the samples are brought to and from the reactor core using compressed nitrogen.

<b>Legend</b>	
<b>F</b>	<b>Fuel Element</b>
<b>HF/HR</b>	<b>Half front/ Half Rear Fuel Element</b>
<b>C</b>	<b>Control Rod</b>
<b>CRT</b>	<b>Cadmium Rabbit Tube</b>
<b>BRT</b>	<b>Bare Rabbit Tube</b>
<b>HC</b>	<b>Hot Cell</b>
<b>S</b>	<b>Source Holder</b>

Figure 1.9. Legend Description of Core Configuration.

The bare rabbit tube allows irradiation with fast, epithermal, and thermal neutrons. The cadmium rabbit tube is used to filter out the thermal neutron component. Movable void tubes, an isotope production element and a core access element can also be positioned in the core grid plate depending on research needs. Other irradiation facilities include a source holder tube, a neutron beam tube, and the thermal column mentioned above. The beam port provides a beam of neutrons for ex-core irradiations and experiments.

The MSTR beam tube consists of a sealed, air-filled aluminum tube protrude through the pool wall into the reactor pool to the edge of the core grid plate. The portion of the tube that penetrates through the pool wall terminates at an opening in a basement

experimental area. A stainless-steel shutter assembly is used to provide a collimated neutron beam, and consists of a fixed plug and a rotating shutter. An off-axis 70×44 mm Boral-lined rectangular duct passes through both plug and shutter. When the shutter assembly is closed, the middle segment of the shutter is rotated so as to break the neutron beam path. The plug in this case acts as a shield. In the open position, the shutter rotates such that the rectangular ducts align and form a path from the air-filled aluminum tube to the basement experimental area, separated only by a lead shield. The lead shield is 5.7 cm thick and is positioned before the beam path to reduce the prompt gamma flux in the basement experimental area. A cross-sectional view of the beam tube is shown in Figure 1.10 [14].

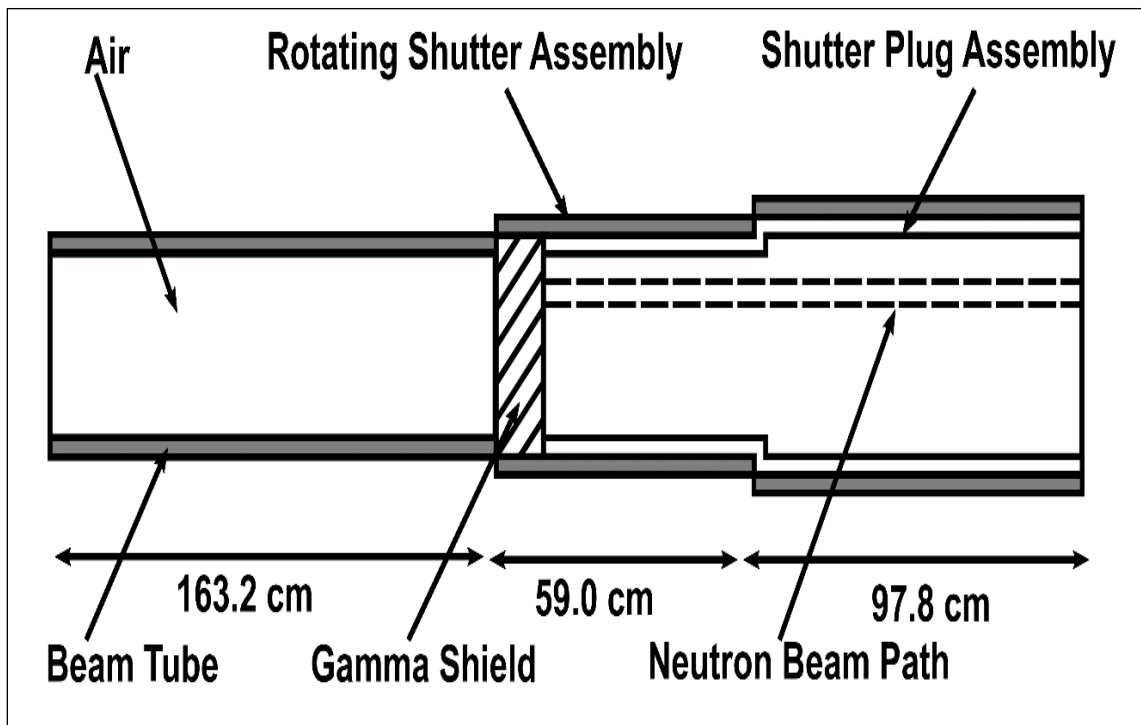


Figure 1.10. The MSTR Beam Port Schematic. Dimension Details were Obtained from the Original Blueprints.

### 1.3. NEUTRON ACTIVATION ANALYSIS

Neutron Activation Analysis (NAA) is a nuclear analytical technique used for determining the isotopic concentrations in pure elements or elemental concentrations in a compound or mixture. NAA is an exceptionally sensitive non-destructive technique for trace elemental analysis in a wide variety of materials. The first NAA experiment was conducted in 1936 by Hevesy et al. [15]. Since then, NAA has been further developed into a number of highly valuable analytical techniques and is routinely performed at a number of research reactors. Though NAA sometimes uses ( $\alpha,n$ ) neutron sources and neutron generators, the much higher neutron fluxes available at research reactors allow for a large number of elements in small volumes of material to be identified with exceptionally low detection limits [16].

In NAA, neutrons activate the sample material producing radionuclides. In a thermal spectrum nuclear reactor, neutrons are grouped into three main energy ranges: thermal, epithermal and fast. Thermal neutrons have an energy distribution described by the Boltzmann statistics of a non-interacting gas. The average thermal neutron at room temperature has an energy of 0.0253 eV and a speed of 2200 m s<sup>-1</sup>. Thermal neutrons are most often used in NAA experiments owing to the tendency for absorption cross sections to go as the inverse neutron velocity making them favorable reactions at low neutron energies. Epithermal neutrons are found in an approximate energy range from 0.5 eV to 100 keV and have a characteristic slowing down spectrum described by an approximately 1/E energy dependence. Fast neutrons range in energy from about 100 keV to 20 MeV [17]. Their energy spectrum is usually described with a semi-empirical Watt fission spectrum.

NAA is used for both qualitative and quantitative identification of elements in a specimen. In qualitative analysis, one identifies radionuclei in the activated specimen using one or more spectroscopic techniques. The characteristic decay radiations identify the radionuclei in the specimen. From this information, one can infer the target element or elements in the sample. Gamma ray spectroscopy is commonly used for this task as many activation products can be uniquely identified from the energies of their characteristic gamma rays. With the advent of High Purity Germanium Detectors, gamma spectroscopy has become a very powerful technique. Alpha, beta and X-ray spectroscopy are also used in certain circumstances.

In quantitative analysis, the number or intensities of specific gamma rays (or other radiations) emitted from the specimen can be related to a number of target atoms present in the sample. Analysis can be conducted based on the type of radiation, energy of radiation, intensity of radiation, and half-life of produced radioisotopes [18]. To permit quantitative analysis, one must also know, at the bare minimum, the mass of the specimen, the efficiency of the detector(s), the neutron flux, and the irradiation, decay and count times. Standards are sometimes used when the flux (or flux spectrum) is not well characterized. There are two types of gamma rays analysis depending on the timescale of the measurement. These are Prompt Gamma NAA and Delayed NAA. In Prompt Gamma Neutron Activation Analysis (PGNAA) the prompt gamma rays emitted during neutron irradiation are simultaneously detected by placing a detection system next to the specimen under irradiation. In Delayed Neutron Activation Analysis, the measurements are performed after irradiation while the specimen is undergoing radioactive decay [19].

To summarize the entire NAA process, first, the target nucleus becomes unstable when it captures a neutron. This requires that the next heaviest isotope to the target is unstable. For the unstable nuclide to become stable again, the nucleus will usually undergo  $\alpha$ ,  $\beta^-$ ,  $\beta^+$ , electron capture,  $\gamma$  decay, or any combination of these decay modes. Information about the neutron flux and concentration of the target can be known by measuring the activity of the unstable isotope [18]. Figure 1.11 illustrates the processes involved in neutron activation.

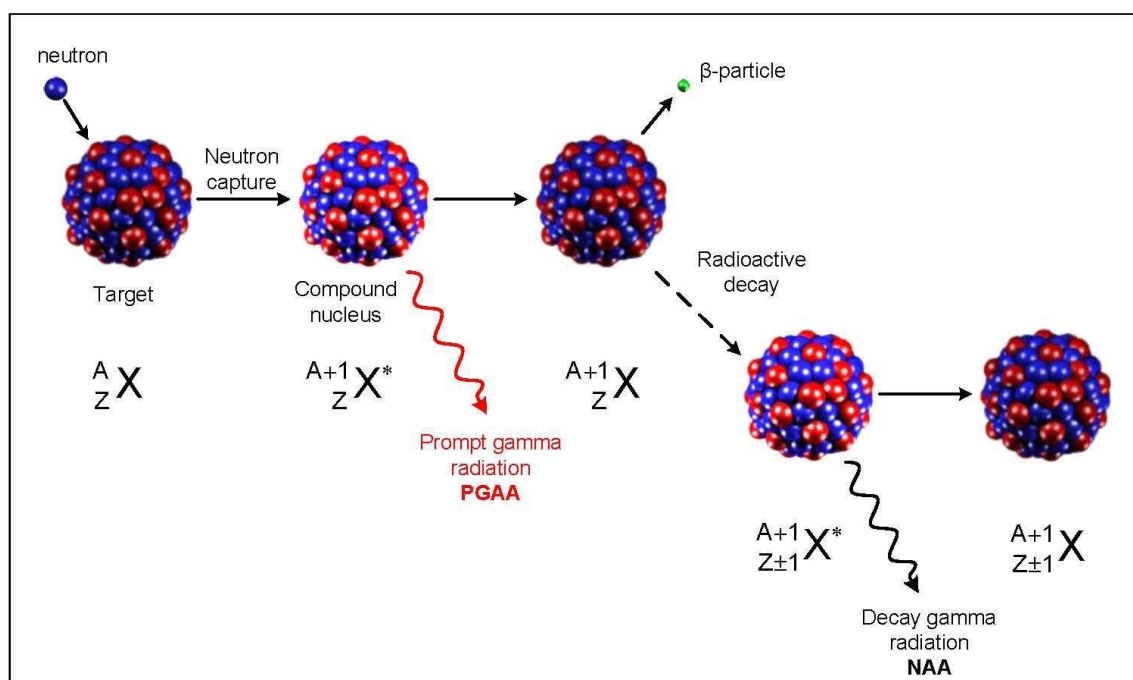


Figure 1.11. Neutron Capture Reaction and Emission of Prompt and Delayed Neutrons [20].

Due to the high sensitivity of NAA and its ability to determine trace elemental concentrations, the technique has seen use in many different fields. These fields include: biology, medicine, geology, archeology, mining, and environmental research. NAA is

considered an ideal technique for determining the concentrations of a wide variety of trace elements in materials due to its sensitivity and accuracy [21].

In a traditional NAA experiment, an uncharacterized specimen is placed in a well characterized neutron flux. The known flux and measured activity are used to determine the target concentration. If the flux is not known but the target concentration is known, the same techniques can be used to measure the flux. This principle is used to characterize the flux in nuclear reactors. This approach is discussed further in Section 3 where beam port characterization using gold foils was performed.

#### **1.4. ARTIFICIAL NEURAL NETWORKS**

Machine learning is a subset of artificial intelligence that incorporates a number of different algorithms to teach a computer to perform certain tasks without explicit instructions. In machine learning, algorithms learn from experience by modifying their response to input data. Artificial Neural Networks (ANN) represent a class of machine learning systems that use learning algorithms to mimic how an animal brain solves problems. Such algorithms can be classified into supervised and unsupervised learning algorithms. Supervised learning algorithms are the most generally used, while unsupervised learning algorithms are applicable to particular problems. In supervised learning an ANN trains itself using known pairs of input and output datasets. In unsupervised learning, networks have the ability to learn on their own without reference to known outputs [22].

ANNs are inspired by the nervous system of the animal brain. The idea of artificial neurons was first posed by Warren McCulloch and Walter Pitts [23]. They used

it to simulate a biological nervous system. Since then, ANNs have been used in different fields. ANNs are a powerful tool used to solve diverse problems in science [24], mathematics [25], engineering [26], economics [27], and other fields [28]. An ANN is a non-linear modeling tool that can have a high accuracy in prediction and is able to identify relationships within large and complex datasets. For example, babies learn to identify objects by touching them. They learn to distinguish hard from soft and cold from hot through a continuous process of mapping sensory input (e.g. touch) to a subjective experience. Neurons in the human brain and their connections carry out the learning process in a similar way. A neuron receives signals from other neurons through connections. These signals are summed and passed through a threshold function. If higher than the threshold, the signal will pass towards the next connection. In an ANN, the threshold is referred to as an activation function. The activation function sets the criteria for deciding if the signal passes or not. Each connection has a weight associated with it. The weight is essentially a multiplication factor that scales the signal going into a neuron. The weighted signals in the neuron are summed and the resulting sum passes into the activation function. During the ANN learning process, weights are adjusted to minimize the error between known outputs and calculated outputs [29, 30].

**1.4.1. Training Algorithms.** The neural network updates connection weights during training using some metric of accuracy or error. The Mean Squared Error (MSE) between the known output and calculated output is usually used as a standard performance function.

Optimum weights can be found when this error is minimized. An ANN's learning process consists of three steps which are: training, validation, and testing.

An ANN usually contains one input layer, one or more hidden layers, and one output layer. Each layer comprises one or more neurons. The neuron number in the input and output layers depend on the problem. Figure 1.12 represents an ANN with 2 input neurons, 3 hidden neurons, and 1 output neuron, and their associated connections.

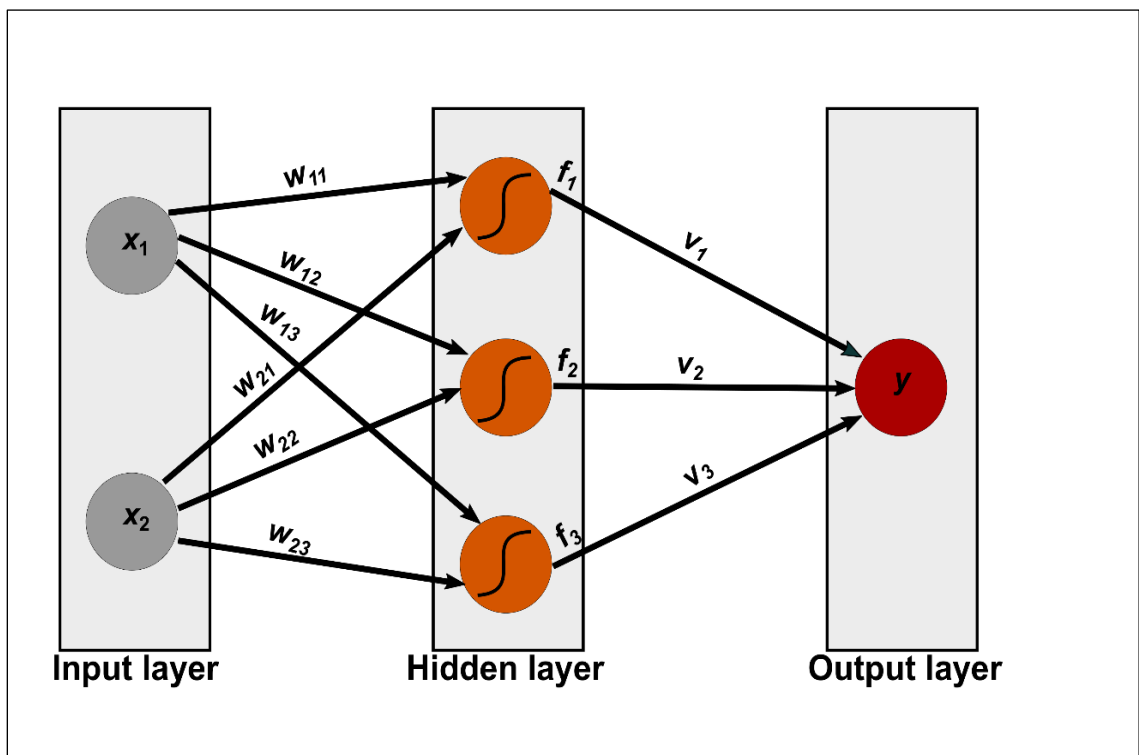


Figure 1.12. Example of a Simple Artificial Neural Network (ANN).

The type of training algorithm chosen depends on the problem type, number of data points, and the complexity of the problem. There are different types of algorithms used for finding the correct weights between connections, including Levenberg-Marquardt (LM), Bayesian Regularization (BR), and Scaled Conjugate Gradient (SCG) algorithms.

Table 1.2. Common Activation Function [29].

Function name	Input-output relation
Hard limit	$a = 0$ when $n < 0$ $a = 1$ when $n \geq 0$
Symmetrical hard limit	$a = -1$ when $n < 0$ $a = +1$ when $n \geq 0$
Linear	$a = n$
Saturating linear	$a = 0$ when $n < 0$ $a = n$ when $0 \leq n \leq 1$ $a = 1$ when $n > 1$
Symmetric saturating linear	$a = -1$ when $n < -1$ $a = n$ when $-1 \leq n \leq 1$ $a = 1$ when $n > 1$
Log-Sigmoid	$a = \frac{1}{1+exp^{-n}}$
Hyperbolic tangent sigmoid	$a = \tanh n$
Positive linear	$a = 0$ when $n < 0$ $a = n$ when $n \geq 0$

LM is the fastest algorithm using a numerical approach to find the weights.

However, for large networks, LM is less efficient due to memory requirements. Whereas, a probabilistic approach used in BR to reduce the performance index. There is no over fitting problem in the BR algorithm due to the probabilistic approach. In addition to LM

and BR methods, the SCG is the best method to use for large data sets due to its small memory requirements. A more comprehensive discussion of these algorithms can be found in [29, 31, 32].

**1.4.2. Activation Function.** The linear combination of the weighted neuron inputs pass through an activation function within the hidden layer neurons. Selection of the activation function depends on the problem in question. There are several types of functions that can be used as activation functions. The functions can be linear or nonlinear depending on the problem. Table 1.2 has commonly used activation functions.

## 1.5. PARTICLE INDUCED X-RAY EMISSION

Particle Induced X-ray Emission (PIXE) is an analytic method used to quantitatively determine the elemental composition in the surface of a material (see Figure 1.13). PIXE can provide compositional information about a material to depths on the order of a few microns to hundreds of microns, depending the ion specie used (e.g. H or He), the ion energy and the stopping power of the material. Light ions (H and He) with energies on the order of a few MeV are usually used in this analysis. Typical sources range from a radioactive source (i.e. an alpha source) to a medium energy van de Graff ion accelerator, to high energy proton cyclotrons.

The basic interaction with of ions with target atoms is shown in Figure 1.14. Ions incident on matter may undergo elastic scattering (Rutherford scattering) with the nuclei or inelastic scattering (ionization and excitation) with the orbital electrons. When inelastic scattering results in the ionization of a core-shell electron, the excited target atom seeks to attain a lower energy state by reverting to its original electron

configuration, i.e. the ground state. It can do so when an outer shell electron fills the core-shell vacancy resulting from the ionization collision. The resulting electronic transition can be accompanied by the emission of electromagnetic radiation in the form of X-rays. For low-Z elements, non-radiative Auger emission can also occur. X-ray emission and Auger are therefore competitive processes. These processes are shown in Figure 1.15.

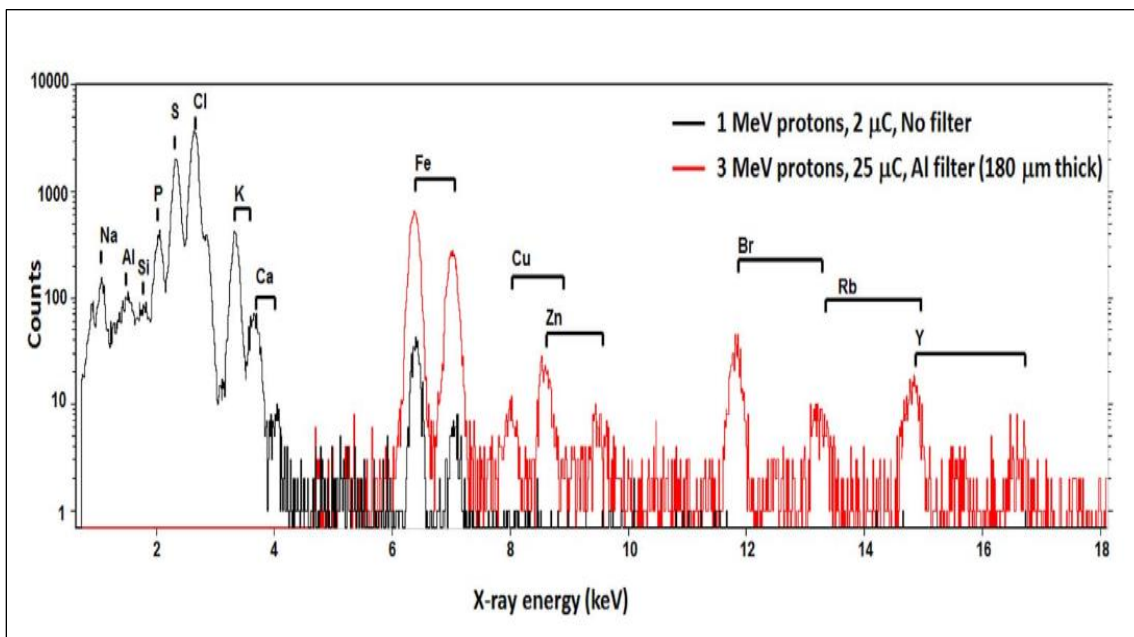


Figure 1.13. PIXE Spectrum [33].

While the Auger electrons are also useful for analytical purposes, it is the characteristic X-rays that provide information on the elemental composition of the film during irradiation in the PIXE technique [34]. Among the ion beam analytical techniques PIXE is a highly sensitive, multi-elemental technique and is routinely used in to characterize: thin films [35, 36], water [37], archaeological [38], and biological samples [33], to name just a few applications.

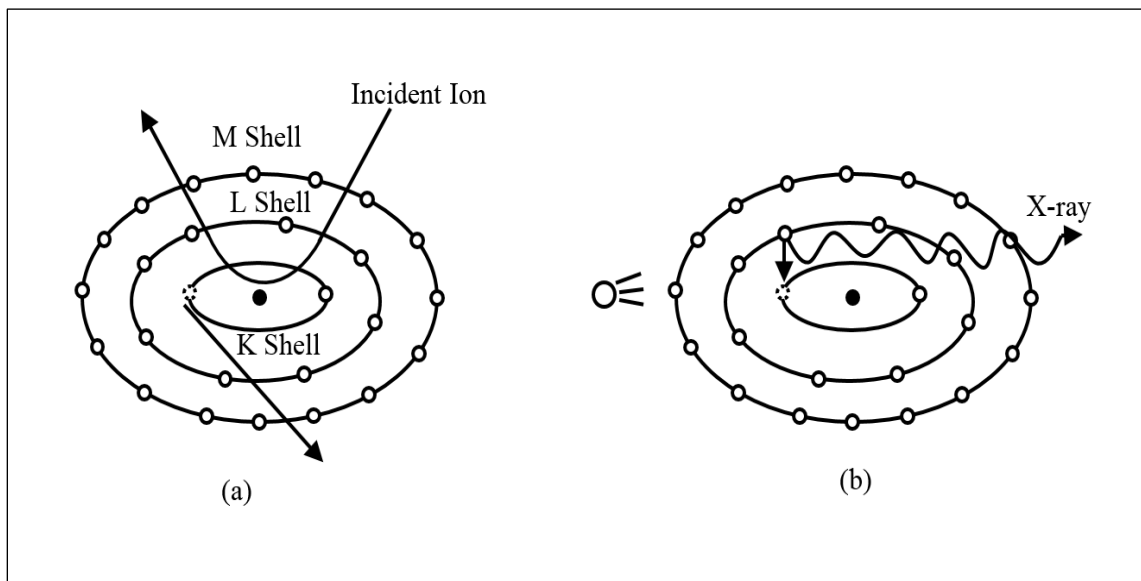


Figure 1.14. Particle Induced X-Ray Emission Process. (a) an Ion Ionizes a K-Shell Electron. (b) an L-Shell Electron Falls into the Resulting Vacancy Releasing a K-shell X-Ray.

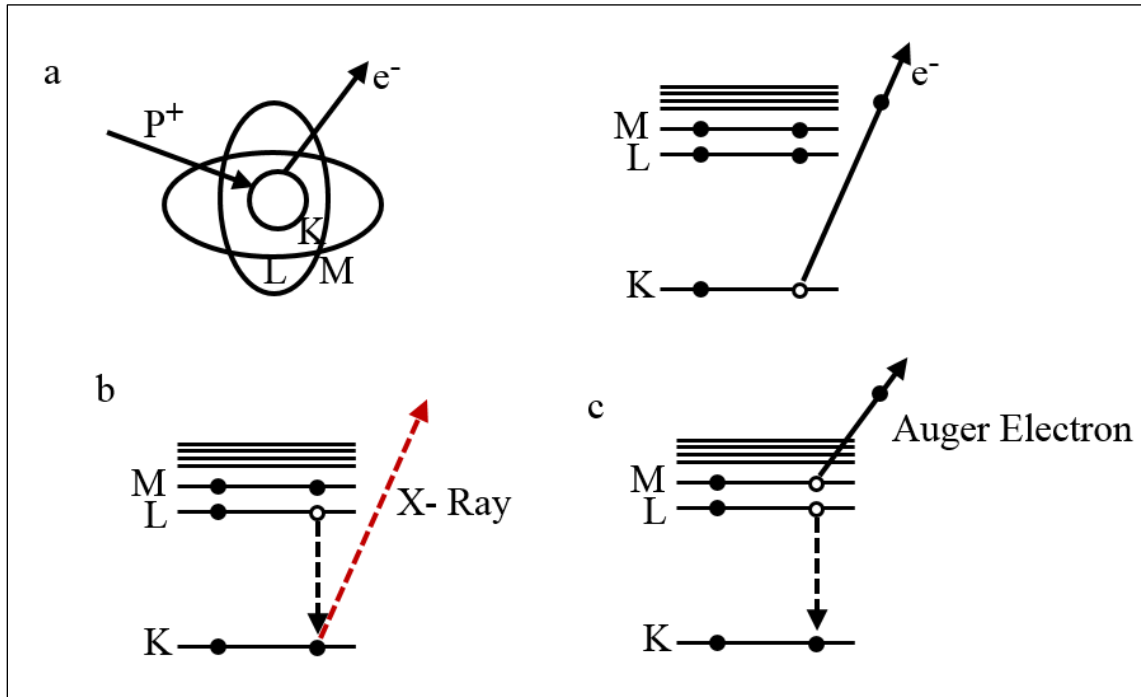


Figure 1.15. (a) Charged Particle Impact Ionization of a K-Shell Electron (b) X-Ray Emission and (c) Auger Electron Emission.

## **1.6. OUTLINE OF THE DISSERTATION**

The remainder of this dissertation proceeds as follows. Section 2 presents a review of the relevant literature on Neutron Depth Profiling, Artificial Neural Networks and Particle Induced X-Ray Emission along with many applications of these tools and techniques. Sections 3-6 recount the main experimental, theoretical and numerical modeling tasks of this doctoral research project. Section 3 summarizes the experimental work done to characterize the neutron flux at the MSTR beam port. In Section 4 results from radiation transport calculations are used to evaluate the viability of building a NDP apparatus at the facility. Section 5 explores the use of an Artificial Neural Network for automated processing of NDP data and compares that approach with traditional data analysis methods. Section 6 demonstrates a concept for a new technique that couples NDP and PIXE to provide additional compositional information about a specimen.

## 2. LITERATURE REVIEW

### 2.1. NEUTRON DEPTH PROFILING

The NDP technique was introduced by Ziegler et al. [4] to study the boron concentration in semiconductors and other materials. This original measurements were performed at a neutron beam port of the Brookhaven National Laboratory High Flux Reactor (HFBR). The neutron flux from that beam port was  $2.3 \times 10^8 \text{ cm}^{-2} \text{ s}^{-1}$ . A well-collimated beam of thermal neutrons passed into a vacuum chamber and through a Si sample. The boron concentration profile in the sample was determined from the energy spectrum of the emitted alpha particles. The authors' demonstrated that NDP was a different and more accurate alternative to the traditional electrical measurements used at the time to address the problem of determining boron concentration in silicon. NDP had the ability to profile boron with a depth resolution of 20 nm. Boron is an important p-type dopant for silicon and it is commonly added to silicon through ion implantation which produces heterogeneous boron concentrations in the surface. Therefore, measurement of the boron distribution in the semiconductor industry is of great importance as it affects a number of electronic and device properties.

Muller et al. [39] introduced the use of a silicon surface barrier detector for more accurate NDP measurements. This detector has been widely adopted since then in different NDP facilities such as The University of Texas at Austin and National Institute of Standards and Technology (NIST).

Later, Biersack et al. [40] applied the NDP technique to light elements other than boron. These included  ${}^6\text{Li}$ ,  ${}^3\text{He}$ ,  ${}^{22}\text{Na}$ , and  ${}^7\text{Be}$ . They also profiled isotopes implanted in

materials other than silicon, such as molybdenum and niobium. Downing et al. [41-43] also applied the NDP technique to boron, nitrogen, and lithium. Biersack and Fink also studied boron and lithium implanted in semiconductors [44].

Since then, NDP has been used extensively to profile Li in lithium-ion batteries, boron implanted silicon, and few other materials [7, 41, 42, 45-47]. To improve the sensitivity and resolution of the technique, various instrumentation modifications have been developed. A cold neutron [48] beam was used at NIST to improve the detection limits of NDP. A cold neutron beam is used instead of a thermal neutron beam to increase the probability of absorbing a neutron by the specimen. Most absorption reaction cross sections are inversely proportional to the neutron velocity. Thus absorption reaction rates tend to increase with decreasing neutron temperature. This modifications made led to both an increase in the neutron fluence in the beamline and a four-fold improvement in the detection limit over the previous depth profiling system. An illustration of the NIST cold neutron depth profiling chamber is shown in Figure 2.1

Time-of-flight (TOF) measurements [7, 49, 50] have been used to decrease the uncertainty in the charged particle energy. Traditional spectroscopy using a barrier detector and TOF measurements have been compared [7]. In TOF-NDP, there is a timing start and stop signal to determine the velocity (hence energy) of the emitted alpha while in traditional NDP, residual kinetic energy of the charged particle is measured directly. In TOF-NDP, secondary electrons produced when the charged particle leaves the surface were detected with a microchannel plate (MCP) as shown in Figure 2.2.

The signal was used as the TOF start trigger. A second microchannel plate was used to acquire the stop signal from the alpha.

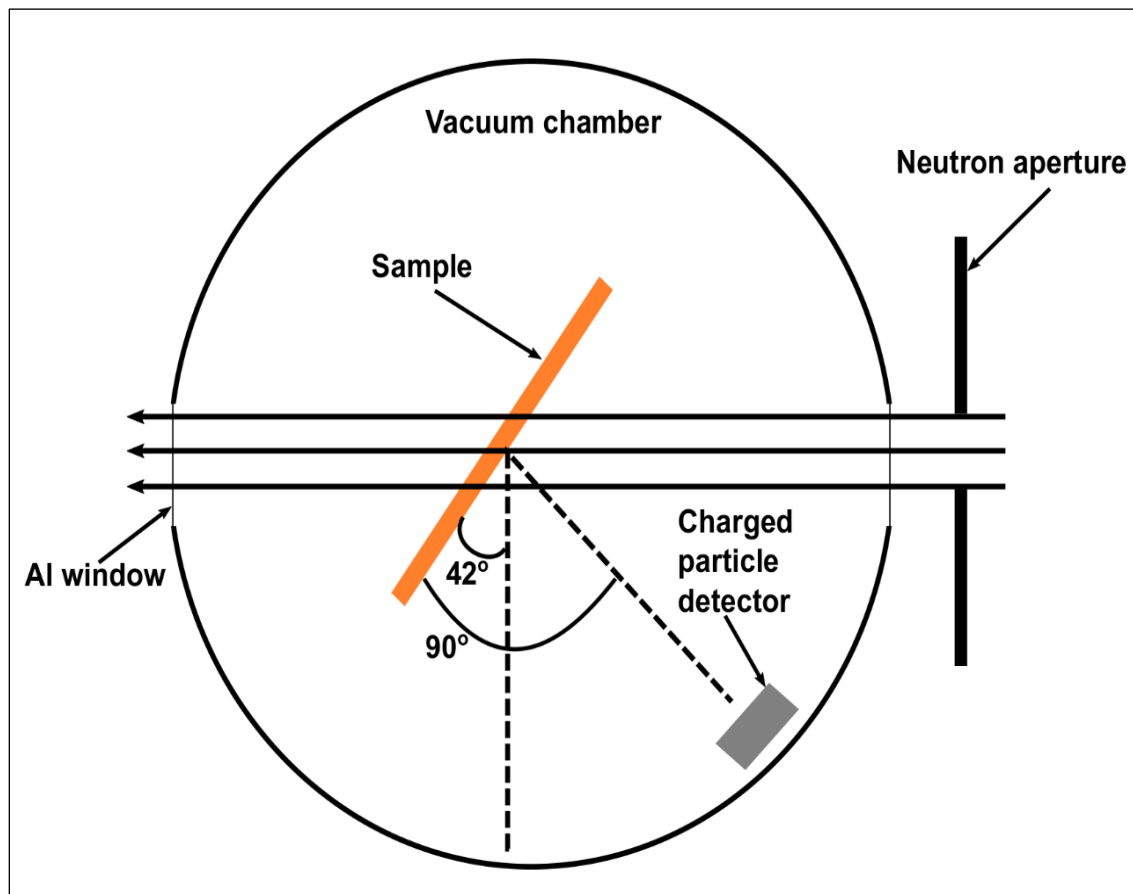


Figure 2.1. Illustration of NIST Cold Neutron Depth Profiling Chamber (from [51]).

The time-of-flight of the charged particle is the time elapsed between the start signal and when the particle hits the stop detector. The TOF apparatus had a significant resolution improvement over the traditional spectroscopy methods used in NDP. The reason for this improvement is that the energy uncertainty introduced from a timing measurement using microchannel plates is relatively small compared to the energy resolution of semiconductor detectors.

Vacík et al. [52] used pulse shape discrimination to reduce the NDP background noise. This signal processing resulted in significantly less low energy noise. To increase

the count rate for a low flux reactor, large angle coincidence spectrometry was used without corrupting depth resolution [53]. However, for this method to be viable, the sample should be thin enough for both charged particles to exit the sample.

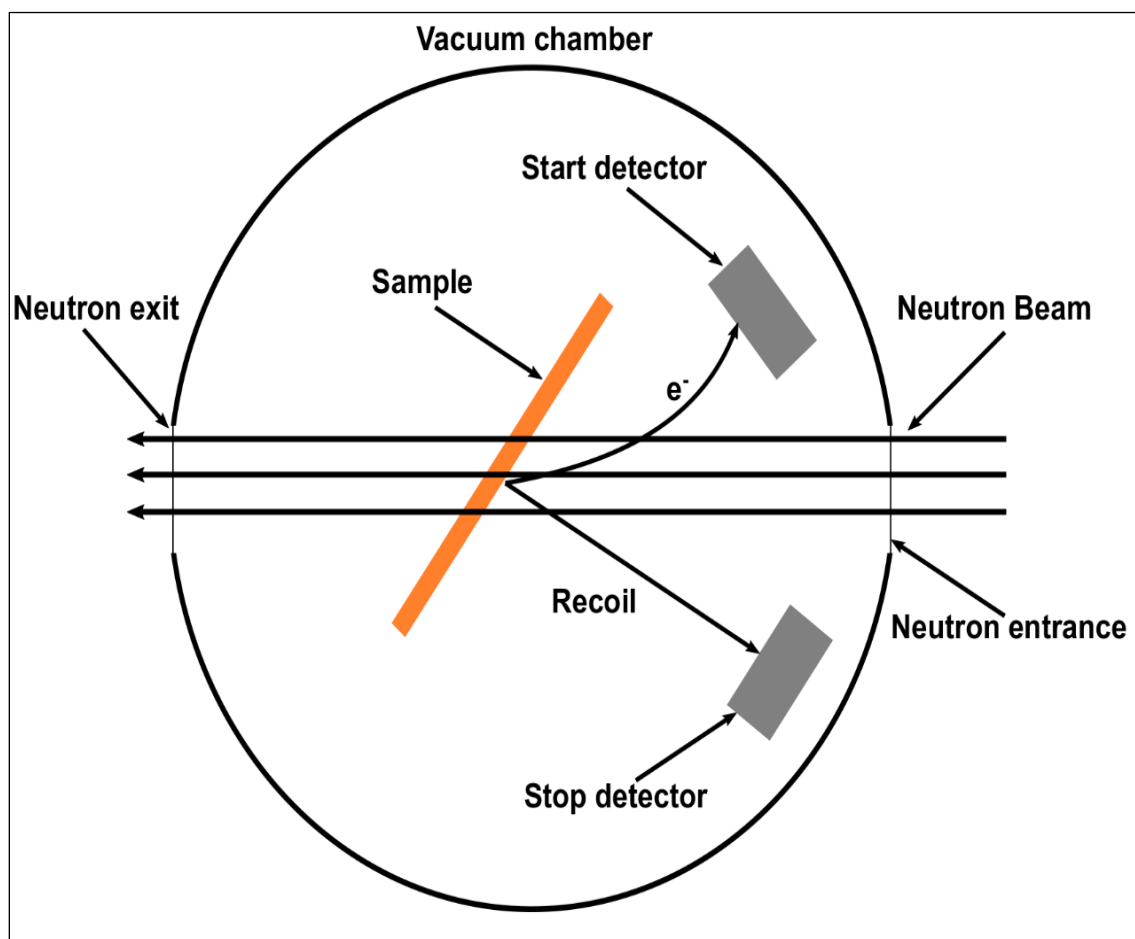


Figure 2.2. Schematic of Neutron Depth Profiling-Time of Flight (TOF-NDP) (from [50]).

$^6\text{Li}$  depth profiling has been emerging in recent years. In situ measurements of lithium movement in thin film electrochromic coatings was conducted by Lamaze et al. using cold neutron depth profiling [54]. In this study, different bias voltages on the film

layers were taken for in situ measurements. Simultaneous optical transmission data and lithium NDP spectra were taken. Measurement of lithium migration was conducted on a complete, active device. This device was installed in the sample position in the neutron beam and electrodes were connected to either batteries or a power supply via electrical feedthroughs in the vacuum chamber.

Benchmarking between two NDP facilities at NIST and UT-Austin, was conducted using lithium ion cell electrodes [55]. Cathodes of differing composition in lithium batteries were analyzed. These materials included:  $\text{LiMn}_{1/3}\text{Ni}_{1/3}\text{Co}_{1/3}\text{O}_2$  and  $\text{LiFePO}_4$ . Shape, concentration, and depth of the lithium were measured and yielded similar results at each facility.

NDP was used to study the aging of lithium ion batteries [56]. To understand the loss of active lithium as a battery ages, lithium concentration measurements within a  $\text{LiFePO}_4$  cathode and graphite anode were conducted over the operational lifetime and correlated with ageing mechanisms. The effect of charging and discharging current rates (C-rate) was also studied in the lithium ion cell. The graphite anode was bonded to a copper substrate while the cathode was bonded to aluminum substrate. The electrolyte used in the cell was lithium hexafluorophosphate ( $\text{LiPF}_6$ ). The evolution of the lithium concentration profile before and after ageing is shown in Figure 2.3.

In situ Neutron Depth Profiling has been used to provide temporal and spatial measurements of Li concentration and transport during charging and discharging [57]. The apparatus used is shown in Figure 2.4. In situ NDP provides exceptional sensitivity in both temporal and spatial domains and is a powerful technique for studying battery technology.

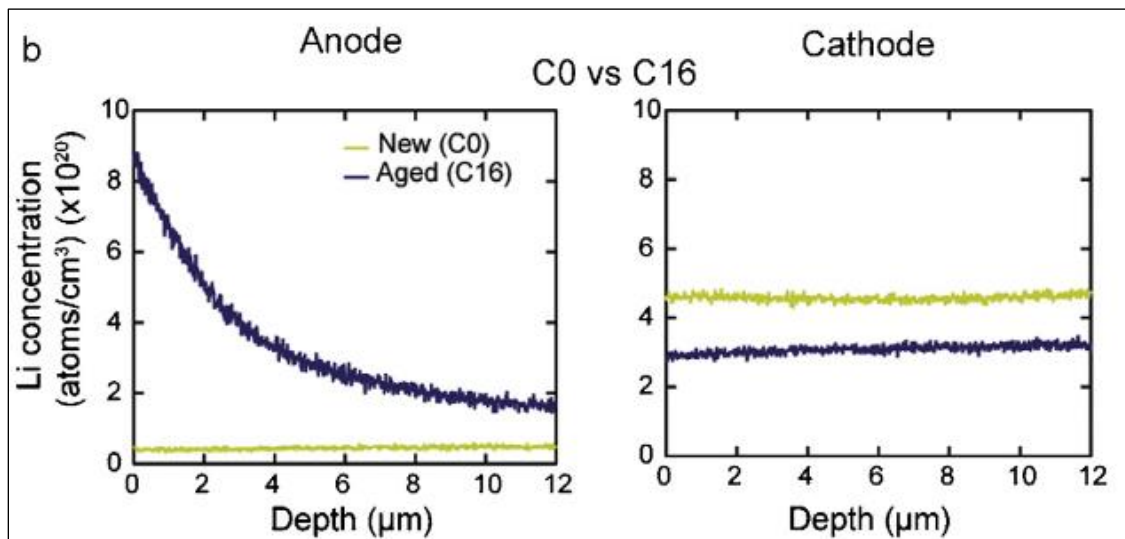


Figure 2.3. Li Profile in  $\text{LiFePO}_4/\text{Graphite}$  Cell Measured with NDP. The Figure on the Left Shows the Li Profile in the Graphite Anode Before and After Ageing. The Figure on the Right Shows the Same for the  $\text{LiFePO}_4$  Cathode (from [56]).

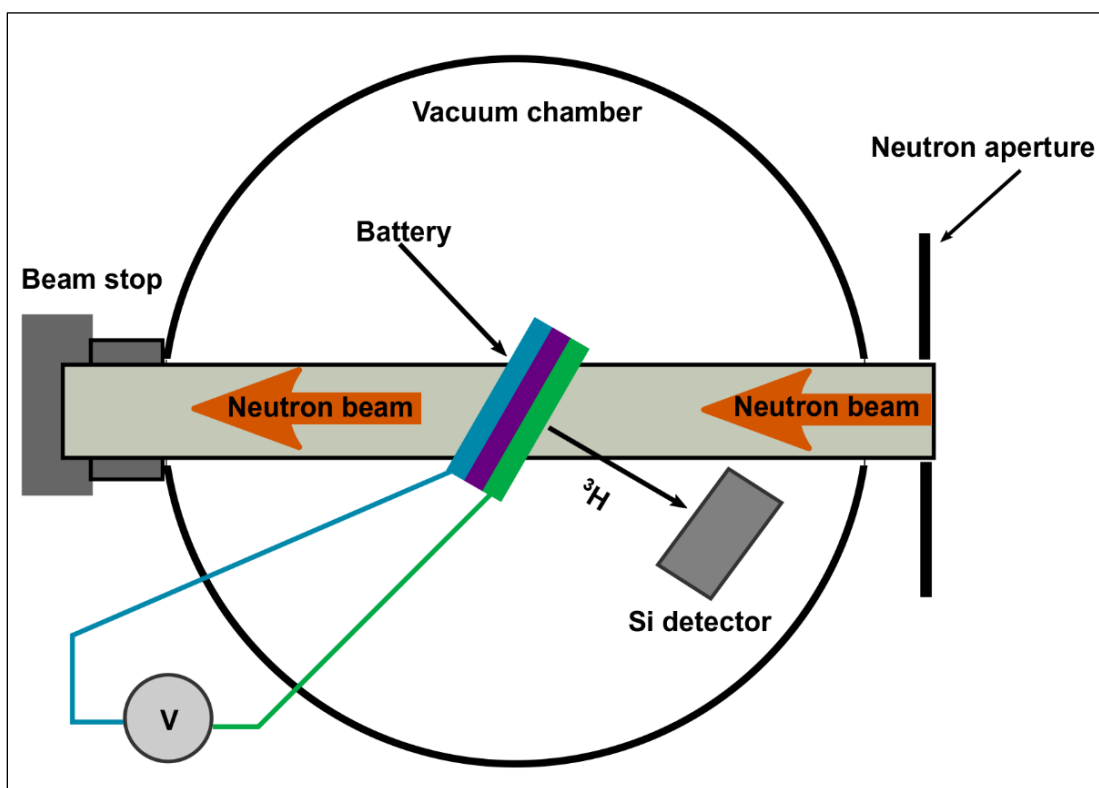


Figure 2.4. Illustration of an In Situ NDP Apparatus for Studying Li Ion Batteries (from [57]).

## 2.2. ARTIFICIAL NEURAL NETWORK

The first use of artificial neurons was in the 1940s by McCulloch and Pitts to model real biological neurons. They consisted of two inputs and one output [23]. The authors demonstrated that an ANN can be used in computation. Rosenblatt [58] developed the perceptron network used in learning. He used randomly connected perceptrons to change the weights of the network. A mathematical method for adapting connection weights was developed by Nguyen and Widrow [59] to reduce training time. They used a gradient search method to minimize the mean squared error. This algorithm later became known as Least Mean Squares (LMS).

Ghal-Eh et al. [60] investigated the use of ANNs for analyzing Prompt Gamma Neutron Activation Analysis (PGNAA) data. Their measurements involved the determination of NaCl content in a NaCl aqueous solution using an AmBe neutron source, and BGO detector. They trained their neural network using MCNPX-simulated spectra.

Skrypnyk [61] used a combination of MCNP and Geant4 simulations to model the CdZnTe detector response to  $^{75}\text{Co}$ ,  $^{137}\text{Sc}$ ,  $^{131}\text{I}$ ,  $^{133}\text{Ba}$  and  $^{241}\text{Am}$  sources. The spectra obtained were used to train a neural network.

Detection of illicit drugs and plastic explosives using ANN was demonstrated by Ferreira et al. [62]. Their network had the ability to recognize illicit materials with an automated response in approximately 1 min.

Varley et al. [63] developed a method to reliably characterize the spatial distribution of radon contamination in an area. Medhat [64] used an ANN to identify the naturally occurring radionuclides,  $^{226}\text{Ra}$ ,  $^{232}\text{Th}$  and  $^{40}\text{K}$  in soil samples.

Kardan et al. [65] trained a neural network to unfold fast neutron spectra from threshold activation detectors. Their results showed that neural networks are efficient in predicting neutron spectra. Doostmohammadi et al. [66] also used a neural network trained with simulated prompt gamma spectra to identify elements a sample. They used MCNP to simulate the prompt gamma spectra produced by thermal neutron absorption in TNT sample. Their ANN model had the ability to identify elements correctly 96% of the time.

Zadeh et al. [67] used an ANN for analyzing gamma spectra to determine the composition of cement. They used MCNP simulations to simulate neutron capture delayed gamma-ray spectra of samples with variable concentrations of Ca, Si, Al and Fe.

Sang Hai-feng et al. [68] studied the carbon, hydrogen and oxygen contents in coal using the Pulsed Fast-Thermal Neutron Analysis method (PFTNA). A  $\text{Bi}_4\text{Ge}_3\text{O}_{12}$  (BGO) detector was used to measure the elemental makeup of coal. A neural network back-propagation (BP) model was used to process the data. Their study showed that a 15 min acquisition time was needed when traditional data analysis was performed, while similar results could be obtained within a matter of seconds by the trained neural network.

### **2.3. PARTICLE INDUCED X-RAY EMISSION**

X-rays were first discovered by Roentgen [69] using a cathode ray tube. Birks et al.[70] compared characteristic X-ray production from different specimens of Ti, Cr, Fe, Cu, Ge, Zr, and Au using protons and electron impact. Chadwick [71] was the first to reported X-rays emission from alpha particle bombardment. He concluded that X-ray

emission was not practical for analytical purposes due to the low intensities observed. The use of Ion-Induced X-rays (IIX) for analytical purposes was first reported by Khan et al. [72] in 1965. In their experiments, a 100 keV proton beam was used to induce X-ray emission in thin films. A proportional counter was used to detect the X-rays. The low energy resolution on that early detector type prevented clear separation of certain elements. The historical name IIX later changed to Particle Induced X-ray Emission (PIXE). It is now regarded as a powerful and standard method for quantitative trace elemental analysis. It is used in diverse fields including biology, environmental science, and archaeology [38, 73, 74].

Johansson et al. [75] were the first to combine a several MeV proton beam with a much higher energy resolution Si(Li) photon detector. They showed that PIXE is a highly sensitive multi-element technique capable of 10-12 g detection limits. Alpha particles were also explored as an excitation source by Watson et al. [76] and Flocchini et al. [77]. Heavy ions were used as an excitation source as early as 1970 [75]. Widespread adoption of heavy ion techniques, however, only became more common with the commodification of ion beams. The possibility of producing X-ray using heavy ions was reported by Garcia et al. [78]. They found that heavy ions were good at characterizing trace high-Z elements. Heavy ions produce very complicated X-ray spectra however. For this reason, they have not been pursued for multi-elemental analysis to the same extent as light ions. Moreover, fewer heavy ion impact cross section data libraries exist making quantitative analysis difficult. Accelerators that produce particle beams of energetic protons, alpha particles and heavy ions have made trace element analysis with PIXE possible in many different materials [76, 79].

### **3. NEUTRON FLUX CHARACTERIZATION OF THE BEAM PORT OF THE MISSOURI UNIVERSITY OF SCIENCE AND TECHNOLOGY REACTOR**

#### **3.1. OVERVIEW**

The primary purposes of the Missouri University of Science and Technology reactor (MSTR) are education, training, and research [80]. MSTR has various experimental facilities including: an isotope production element, in-core irradiation void tubes, bare and Cd-lined pneumatic irradiation systems (rabbit system), and a moveable core access element. Neutron beamlines are routinely used in fields of materials science, physics, polymer science, manufacturing, analytical chemistry and structural biology [81]. Neutron Depth Profiling (NDP) [55, 82, 83], Prompt Gamma Activation Analysis (PGAA) [84, 85], neutron radiography/tomography [86, 87], and Positron Annihilation Spectroscopy (PAS) [88, 89] are a few examples of techniques developed at beamlines of small research reactors [6].

For the purposes of designing most beam port apparatus, it is necessary to know the magnitude and angular/spatial distribution of the neutron flux exiting a beam port. Neutron-sensitive radiograph imaging plates and gold foils have been used for characterizing the total flux at the Oregon State University TRIGA reactor beam port [84]. The neutron beam profile may be determined using a regular array of gold foils [90, 91]. The combination of activation techniques and neutron imaging has also been used for characterizing the neutron beam profile at other facilities [6, 92, 93].

Though most neutron beam line experiments utilize a primarily thermal or cold neutron spectrum, it is important to quantify both the thermal and epithermal flux in order to assess the possible influence of higher energy neutron interactions and interferences in

the experimental apparatus as well as to protect detectors and other sensitive electronics equipment. This section presents the experimental work performed to characterize the neutron flux spatial distribution and two group energy spectrum of the MSTR beam port. Information about the neutron flux at the beam port is needed in the simulations presented in Sections 4-6.

### **3.2. BEAM FLUX CHARACTERIZATION USING NEUTRON ACTIVATION ANALYSIS**

Neutron Activation Analysis is a method that is routinely used to determine the concentration of trace elements in a matrix given prior knowledge about the neutron source strength and its spectrum or, indirectly, by comparing to the activation rates for a suitable set of comparable standards. The same approach can also be used to precisely characterize a neutron source given a known target (usually referred to as flux monitor), its mass, composition and appropriately weighted group cross sections and correction factors describing its activation and self-shielding [90, 94]. Indeed several methods relying on activation of metallic foils, wires and solutions can be used to characterize a reactor flux [95-97]. Briefly, a flux monitor is irradiated in a neutron field to activate nuclei producing characteristic decay radiations that can be quantified using spectroscopic techniques, such as gamma ray spectroscopy. Gold (Au) foils were irradiated at the beam port of the MSTR which is commonly used for measuring the neutron flux using the Neutron Activation Analysis (NAA). This method was used to determine the thermal and epithermal neutron flux and its spatial distribution at the opening of the Missouri University of Science and Technology Research Reactor (MSTR) beam port.

### 3.3. METHODOLOGY

The neutron flux was experimentally determined using a foil activation method and compared to simulated results from an MCNP model of the MSTR beam port. The sample activity after irradiation is given by the basic form of the neutron activation Equation.

$$A(t_{ir}) = N\sigma\phi(1 - e^{-\lambda t_{ir}}) \quad (4)$$

where  $A(t_{ir})$  is the sample activity at the end of irradiation,  $N$  is the number of target nuclei,  $\sigma$  is the effective one-group microscopic cross section of the target nuclei,  $\phi$  is the one-group neutron flux,  $\lambda$  is the decay constant of the activated nuclei, and  $t_{ir}$  is the irradiation time. The number ( $N$ ) of target nuclei is given by:

$$N = \frac{a_i m_i N_A}{A_i} \quad (5)$$

where  $a_i$  is the natural isotopic abundance of the target nuclide (at.%),  $N_A$  is Avogadro's number,  $m_i$  is the target isotope mass, and  $A_i$  is the isotope atomic weight. The sample activity after a decay time  $t_d$  following irradiation is given by

$$A(t_d) = A(t_{ir})e^{-\lambda t_d} \quad (6)$$

Equation (4) is deceptively simple in that the effective one-group cross section can depend quite sensitively on the neutron spectral shape, the dimensions of the flux monitor, and self-shielding effects. Failing to accurately account for these effects can result in large systematic errors in the measured flux. A less error-prone approach to quantifying the beam port flux considers the contribution from both thermal neutrons and epithermal neutrons and various correction factors for the foil material, its geometry and the irradiation geometry.

The thermal flux and epithermal flux parameter at the MSTR beam port were calculated using a modification of ASTM standard E262-13 [98]. This method compares the activation of a bare flux monitor to the activation of a flux monitor in a cadmium filtered spectrum to determine the thermal flux and epithermal flux parameter (magnitude of the 1/E slowing down flux), effectively breaking Equation (4) into two Equations, each with a different effective one-group cross section and flux. The method accounts for departures from non-ideal  $1/v$  behavior as well as the effects of neutron self-shielding in highly absorbing activation foil materials, such as gold, which was used in these experiments. The thermal flux,  $\phi_t$ , and epithermal flux parameter,  $\phi_e$ , are given by

$$\phi_t = \frac{1}{g\sigma_t G_{th}} \left[ R_b - R_{Cd} \left( 1 + \frac{g\sigma_t f_1}{G_{res} I_o} + \frac{\sigma_t w'}{G_{res} I_o} \right) \right] \quad (7)$$

$$\phi_e = \frac{R_{Cd}}{I_o G_{res}} \quad (8)$$

$g$  is the Westcott factor which accounts from departures from ideal  $1/v$  energy dependence of the cross section in the thermal range.  $\sigma_t$  is the thermal-averaged capture cross section.  $R_b$  and  $R_{Cd}$  are reaction rates for a bare foil and cadmium covered foil, respectively.  $f_1$  accounts for  $1/v$  activation in the 5kT to  $E_{Cd}$  energy range while  $w'$  accounts for non- $1/v$  behavior in the same range.  $G_{th}$  and  $G_{res}$  are thermal and resonance neutron self-shielding correction factors, respectively.  $I_o$  is the resonance integral. Though flux depression factors should normally be included when the activation foils are surrounded by a moderating medium, the present experiments were conducted in air and therefore moderation effects are negligible.

The epithermal component Equation (8) assumes that all neutrons above the Cd cutoff energy behave as slowing down neutrons with an energy-dependent flux that goes

as the inverse neutron energy (1/E-dependence). In reality, the fission spectrum neutrons also add to the neutron flux at fission neutron energies, so a simple 1/E flux spectrum underestimates the reaction rate for fast neutrons. However, since the fission spectrum-averaged cross section for radiative capture in  $^{197}\text{Au}$  (approx. 51 mb) is small compared to the resonance integral, this contribution is negligible. Nevertheless, the resonance self-shielding correction factor calculated in the analysis did include a superimposed Watt fission spectrum term. The resonance self-shielding correction factor is given by

$$G_{res} = \frac{\int_{E_{Cd}}^{\infty} \sigma_a(E) f(E) \phi(E) dE}{\int_{E_{Cd}}^{\infty} \sigma_a(E) \phi(E) dE} \quad (9)$$

where  $f(E)$  is the energy-dependent resonance self-shielding correction factor.  $\phi(E)$  was a superimposed 1/E+Watt fission spectrum weight function with an approximately 2:1 ratio of fast to epithermal neutrons. Although there is considerably less self-shielding in the fast energy range, inclusion of the Watt fission spectrum term only accounts for about a 1% difference in the value of  $G_{res}$  compare to the calculation only using the 1/E weight function. This is due to the small magnitude of the absorption cross section in that energy range. A similar argument can be made comparing the difference between the resonance integral and epi-Cd group cross section weighted by both 1/E and Watt spectrum terms. The resonance integral, by definition, only includes the 1/E term. Inclusion of the Watt term again only increases the group cross section by 1% of  $I_o$ . This can be taken to imply that the fast flux does not need to be known to accurately determine the epithermal flux parameter, at least up to a 2:1 fast to epithermal flux ratio. The authors will note that threshold nuclear reactions such as  $^{58}\text{Ni}(n,p)^{58}\text{Co}$  and multi-foil spectral unfolding techniques can be used to measure the fast flux.

**3.3.1. Experimental Procedure.** Based on the expected magnitude of the total flux at the MSTR beam port, gold activation foils were used for this characterization. Gold has a single stable isotope,  $^{197}\text{Au}$ , with a 98.7 barn cross section for radiative capture ( $^{197}\text{Au}(n,\gamma)\text{Au}^{198}$ ) [98, 99]. Although self-shielding in gold complicates the subsequent analysis somewhat, its large cross section makes it suitable for measuring low neutron fluences.  $^{198}\text{Au}$  undergoes  $\beta$ - decay with a 2.7 d half-life to Hg-198 releasing a 411.8 keV gamma in 96% of the beta decays [98, 99]. Six high-purity gold foils (Shieldwerx) of 25  $\mu\text{m}$  thickness were irradiated in each experiment. The masses of each foil are included in Table 3.1.

Table 3.1. Gold Foil Masses.

Foil	Mass (g)
1	0.124
2	0.116
3	0.122
4	0.114
5	0.112
6	0.062

Two sets of gold foils were prepared and activated at the pool wall opening of the MSTR beam port. Six bare Au foils were irradiated in the beam. The second set was irradiated under the same conditions apart from the insertion of a 1 mm thick cadmium (Cd) filter between the beamline opening and the foils. Cd has a large thermal cross

section but also exhibits an unusual energy dependence originating from a low-energy resonance allowing it to act, in some sense, as a high pass filter for neutron energy. If the thickness of the Cd filter is properly selected, it will allow the majority of neutrons above the so-called cadmium cutoff energy,  $E_{Cd}$ , to pass through and interact with the flux monitor. The cutoff depends on the thickness of the Cd filter and its value, in part, determines the tabulated values of  $f_1$  and  $w'$  used in Equation (7). Thus it is important to match the parameters in Equation (7) with the thickness of the filter used in the experiment. For the 1 mm thick cadmium filter used in this work and recommended in the ASTM standard, the Cd cutoff energy is  $E_{Cd} = 0.55$  eV. The cross section parameters for 25  $\mu\text{m}$  thick, high purity Au-197 at this Cd thickness are given in Table 3.2. It should be mentioned that the self-shielding parameters,  $G_{res}$  and  $G_{th}$  were calculated using the beam geometry factors from [28,29] and ENDF/B-VII nuclear data [30] rather than using the tabulated values provided in the ASTM standard, which are only valid in the case of an isotropic neutron flux.

Foils were suspended in front of the beam port opening in the array shown in Figure. 3.1. For the Cd filtered irradiations, a 1 mm sheet of Cd was placed between the foils and the beam port opening. Though the ASTM standard method calls for the Au foils to be encapsulated on all sides in 1 mm thick Cd boxes, the foils in these experiments were only shielded from thermal neutrons coming out of the beam port.

Epithermal and fast neutrons, in principle, could be transmitted through both filter and Au foil, backscatter and be moderated by some materials behind the foils in the experimental area, re-enter and finally be absorbed by the foils thereby resulting in an undesirable flux contribution in either the thermal or epithermal groups. This is possibly a

legitimate concern when the foils are mounted on any material with even weakly moderating properties. However, as the space behind the foils was essentially empty apart from approximately 2 m of air and a beam stop, the likelihood of the transmitted beam being scattered and reabsorbed by the foils is negligible.

Table 3.2. Cross Section Parameters of 25  $\mu\text{m}$  Thick Au Foil and a 1 mm Thick Cd Filter [98, 100-102].

Parameter	Value
$f_1$	0.468
$I_o$	1550 b
$w'$	0.0500
$G_{res}$	0.539
$g$	1.005
$G_{th}$	0.991

Irradiations were conducted at full reactor power (200 kW) for 4 hours. After irradiation, the foils were placed in a lead shielded High Purity Germanium Detector (HPGe, Canberra) to perform gamma spectroscopic analysis of the 411.8 keV  $^{198}\text{Au}$  photopeak. A traceable multi-isotope europium calibration source (containing  $^{152}\text{Eu}$ ,  $^{154}\text{Eu}$ , and  $^{155}\text{Eu}$ ) was used to calibrate the detector efficiency as a function of energy. Eight photopeaks from 40-1408 keV were used in the efficiency calibration. Interpolation on a best fit polynomial was used to estimate the efficiency at 411.8 keV. Calibration source and foil spectra were analyzed using Canberra analytical software application,

PROSPECT [103]. The detector efficiency,  $\varepsilon$ , for each Eu photopeak was determined using

$$\varepsilon = \frac{C}{\gamma A t_c} \quad (10)$$

where  $C$  is the net counts in a given photopeak,  $\gamma$  is the intensity of the gamma-ray for the photopeak,  $A$  is the source activity (known from the certificate of analysis and age of the source), and  $t_c$  is the live counting time. The detector-to-sample distance was chosen to keep the detector dead time below 10%. The actual dead times were on the order of 1%.

The activation rates,  $R$ , for each foil (bare and Cd covered) were determined by

$$R = \frac{C\lambda}{N\theta\gamma\varepsilon} \quad (11)$$

$$\theta = (1 - e^{-\lambda t_i})(e^{-\lambda t_d})(1 - e^{-\lambda t_c}) \quad (12)$$

where  $C$  now represents the number of counts for the 411 keV photopeak of  $^{198}\text{Au}$ .  $\lambda$  and  $\gamma$  are the decay constant and 411 keV gamma ray intensity for  $^{198}\text{Au}$ .  $N$  is the number density of target nuclei ( $^{197}\text{Au}$ ) calculated using Equation (5).  $\varepsilon$  is the efficiency interpolated to 411 keV from the Eu efficiency calibration.  $t_i$ ,  $t_d$  and  $t_c$  are the irradiation, decay and counting times, respectively. The number of counts in the 411 keV photopeak was determined from

$$C = G - B \quad (13)$$

$$B = \left(\frac{M}{2n}\right)(B_1 + B_2) \quad (14)$$

$C$  is the net peak area (number of net photopeak counts),  $G$  is the gross counts in the region of interest (ROI) with  $M$  channels, and  $B$  is the number of continuum

(background) counts in the same region of interest. The linear continuum counts,  $B$ , is calculated from the sample spectrum using Equation (14).  $B_1$  and  $B_2$  are the sums of  $n$  continuum channels to the left and right of the ROI region, respectively. The uncertainty in the number of counts was propagated from the uncertainties of the gross counts and continuum counts by taking the square root of the sum of the squared errors, assuming Poisson statistics. The uncertainty in the reaction rate included the uncertainty in the number of counts and the uncertainty in the efficiency calibration (about 5%). Other uncertainties that should, in principle, be included but were deemed to be too small to contribute to the final result include: dead-time correction factor; uncertainty in the irradiation, decay and count times; uncertainty in the foil mass; uncertainty in the gamma ray intensity; and the uncertainty in the decay constant. These were all insignificant when compared to the uncertainties from counting statistics and detector efficiency.

Once the reaction rates for each of the flux monitors was determined, Equations (7) and (8) were used to determine the thermal and epithermal flux at each location at the beam port opening. Uncertainties on the thermal and epithermal flux values were propagated from Equations (7) and (8). Contributions included uncertainties on the following parameters:  $R_b$ ,  $R_{Cd}$ ,  $G_{res}$ ,  $G_{th}$ ,  $\sigma_t$  and the ratio  $I_o/g\sigma_t$ . The uncertainties on the activation rates are discussed above. Other uncertainties were available from the nuclear data (i.e.  $\sigma_t$ ,  $I_o/g\sigma_t$ ) while the uncertainties on  $G_{th}$  and  $G_{res}$  were estimated by propagating the uncertainties in the correction factors described in [100, 101] The majority of the uncertainty of the final flux values was found to originate from the uncertainty in the energy interpolation on the detector efficiency calibration curve. Given that  $^{198}\text{Au}$  only exhibits a single strong photopeak, it may be possible to reduce this

contribution to the uncertainty by using a high-efficiency gamma ray detector such as a large volume NaI well detector.

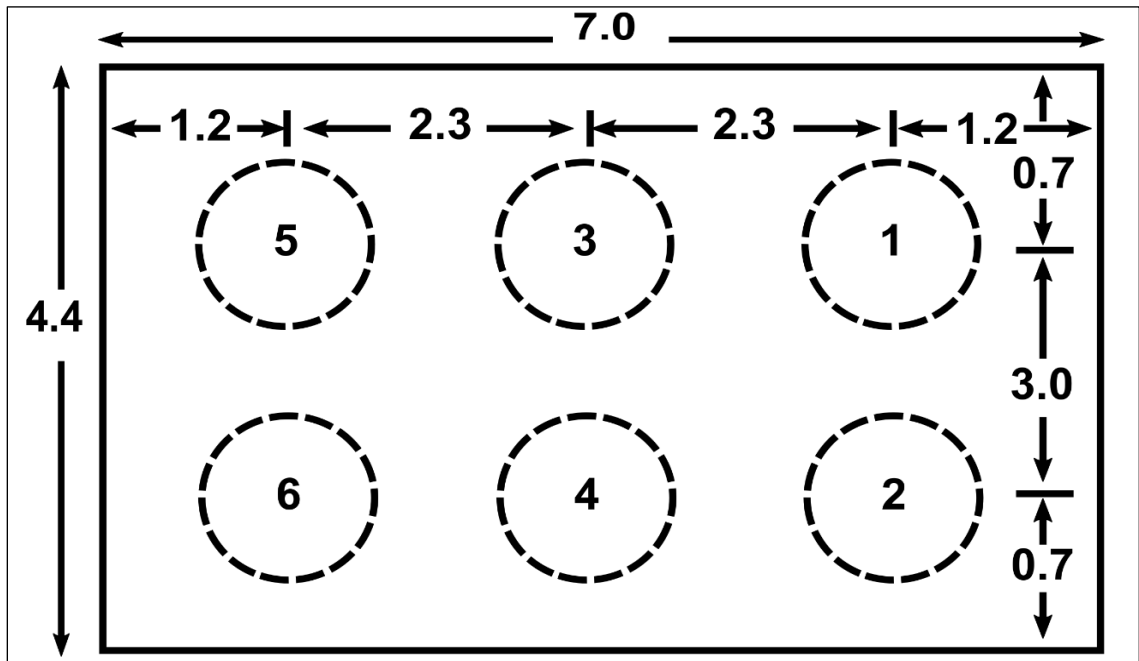


Figure 3.1. Gold Foil Positions. The Small Circles (1-6) Represent the Gold Foils. The Outer Rectangle is the Rectangular Opening. All Lengths are in cm.

**3.3.2. Monte Carlo N-particle Code.** The radiation transport code MCNP6 [104] was used to calculate the MSTR beam port neutron flux. MCNP is a general-purpose Monte Carlo radiation transport code to simulate transport and interactions of different types of particle radiation.

Neutrons, photons, electrons and many other particles can be transported individually or together for applications ranging from nuclear reactor criticality and neutronics calculations, to dose reconstruction, simulation of radiation detector response, shielding design, and high energy physics processes. In the Monte Carlo radiation

transport technique, the trajectory and interactions of an individual particle constitute a history. Many histories are simulated and aggregate statistical information is stored in the form of tallies which measure quantities such as flux, energy deposition, and current [105].

The MSTR model includes the reactor core, thermal column, fuel elements, grid plate, control rods, beam port, and pool water. A major limitation of the model is that it assumes fresh fuel while the current core configuration contains fuel elements with different burnup histories. Only limited information about the core-averaged fuel element burnup is available and the fission product inventory can only be roughly predicted from burnup calculations. Cells at the end of the beam port were modeled to simulate the neutron flux corresponding to the experiment position, as shown in Figure 3.1. An energy card (E card) with sixty-nine energy bins was included with the flux tallies. The energy bins ranged from  $10^{-10}$  to 18 MeV. An F4 tally, which calculates the cell-averaged flux, was used to obtain the neutron flux at each foil at the same positions as the experiment. The MSTR MCNP6 model uses the cross-section library ENDF/B-VI (.66c) for all isotopes.

The MCNP calculations were split into a pair of uncoupled simulations. In the first, the entirety of the reactor core and beam port was included in the cell and material definitions (Figure 3.2). This input deck was used for a criticality (KCODE) calculation. The KCODE criticality calculation was performed with 1 million particles per cycle for 5000 total active cycles with 50 passive cycles. All particles passing a surface plane near the beam tube surface were written into a surface source file using a Surface Source Write (SSW) card. A second input deck, which only comprised the beam port, pool wall

and part of the pool, and contained no fissile materials read in the histories tallied in the SSW card during the criticality calculation via a surface source read (SSR) card.

Approximately 10 billion source particles (NPS) were used to obtain the subsequent flux tallies. The advantage of this method is that it greatly reduces the computational effort required to pass statistical checks in the neutron flux tally at the experimental end of the beam line. Neutrons recorded by the surface source write, being near the beam port, are more likely to be transported down it. By breaking the problem into separate parts, one creates a more efficient fixed-source problem where a greater portion of particle histories contribute to the final flux tally at the beam port opening and a lower average time per history. With this approach, all transport calculations could be performed on a desktop computer with no additional variance reduction.

### **3.4. RESULTS AND DISCUSSION**

The experimental neutron flux values and the Monte Carlo simulation results are shown in Table 3.3. Thermal, epithermal and total (thermal+epithermal) flux values are tabulated with corresponding uncertainties for each foil. The experimental and calculated epithermal flux values were calculated by integrating the epithermal flux spectrum from the Cd cutoff (0.55 eV) to 100 keV, the transition energy between the slowing down region and the Watt fission spectrum. The MCNP calculations were found to consistently underestimate the experimental values for the thermal flux and total flux but overestimate the values for the epithermal flux. The variance between the experiment and the simulation is thought to be caused by a number of uncertainties and discrepancies

between the actual core and the MCNP model. Perhaps the most significant factor contributing to the discrepancies is the assumption of fresh fuel in the MCNP model.

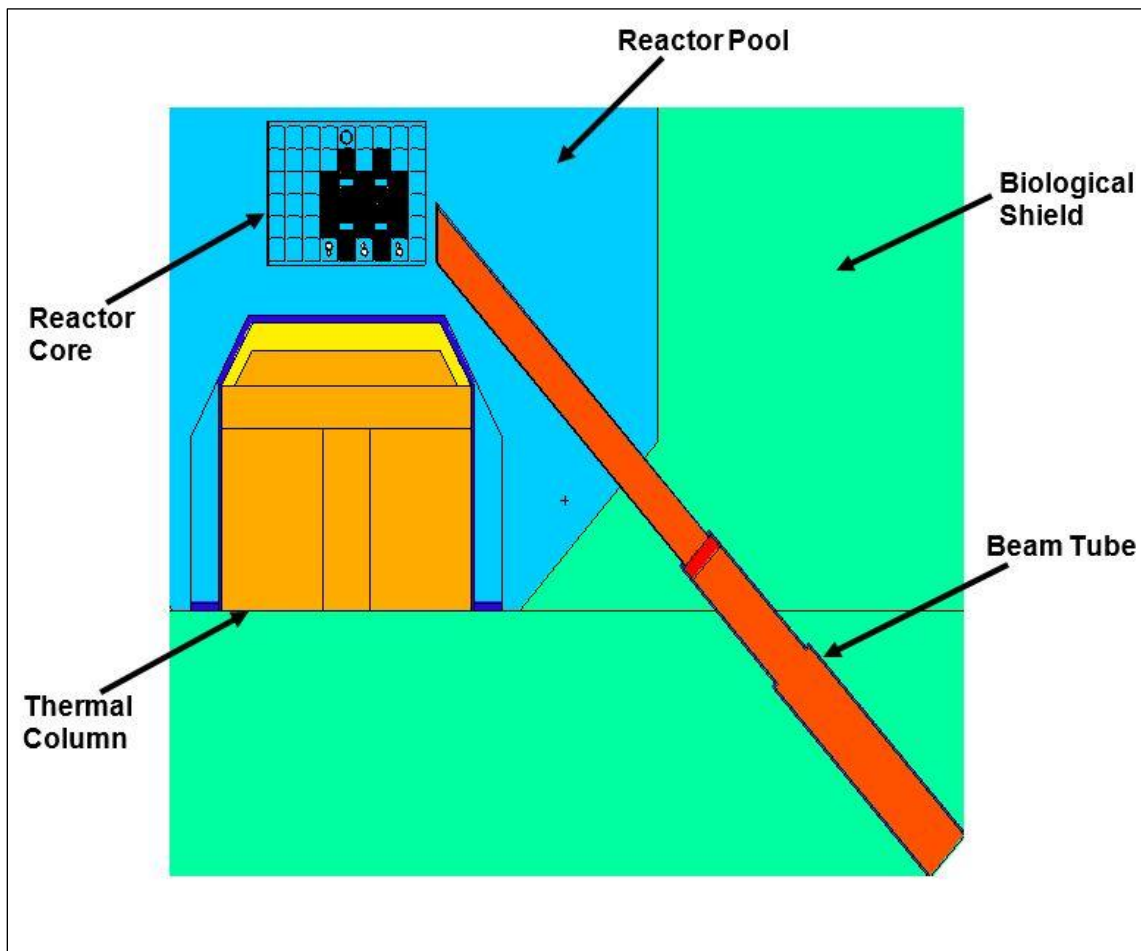


Figure 3.2. Top Down Cross Section of the MSTR.

The actual fuel elements, which vary in burnup, require a larger thermal neutron flux to produce the same element-averaged fission rate as a fresh fuel element. Thus the MCNP calculations, which assume fresh fuel, systematically underestimate the thermal neutron flux required to achieve a specified power level. At the same time, the fast flux, which is approximately proportional to the fission rate, and therefore to the power, is also

roughly proportional to the thermal flux times the macroscopic fission cross section. Therefore, as the fuel is burnt and as neutron poisons are added, the ratio of the fast flux to the thermal flux decreases (spectral softening). This is observed in Table 3.3 by comparing the ratios of fast to thermal flux in the MCNP calculation (fresh fuel) to the ratios of the experimental values (irradiated fuel).

Table 3.3. Experimental and MCNP Neutron Flux at the Gold Foils.

Foil	Exp. Thermal $\times 10^6 \text{ cm}^{-2} \text{ s}^{-1}$	Exp. Epi. $\times 10^5 \text{ cm}^{-2} \text{ s}^{-1}$	MCNP Thermal $\times 10^6 \text{ cm}^{-2} \text{ s}^{-1}$	MCNP Epi. $\times 10^5 \text{ cm}^{-2} \text{ s}^{-1}$	%Difference in (epi.+ thermal) flux
1	$7.9 \pm 0.4$	$9.9 \pm 0.4$	$5.2 \pm 0.09$	$17 \pm 1$	23%
2	$5.5 \pm 0.3$	$8.2 \pm 0.3$	$3.1 \pm 0.06$	$9.8 \pm 0.8$	35%
3	$7.6 \pm 0.4$	$7.5 \pm 0.3$	$4.1 \pm 0.08$	$13 \pm 1$	34%
4	$5.1 \pm 0.3$	$6.8 \pm 0.3$	$2.6 \pm 0.05$	$8.1 \pm 0.7$	41%
5	$5.0 \pm 0.3$	$5.6 \pm 0.2$	$2.6 \pm 0.05$	$8.1 \pm 0.7$	39%
6	$2.9 \pm 0.2$	$5.6 \pm 0.2$	$2.5 \pm 0.05$	$8.1 \pm 0.7$	3%

If, as a first approximation, one considers the systematic error in the total flux as constant flux correction factor (in this case 1.45), the average MCNP flux can be normalized to better agree with the average experimental flux. This is basically what is shown in Figure 3.3 except that the flux of each foil is normalized by the average flux over all foils. This is done for both the experimental and numerically simulated flux values. Apart from one outlier (foil 6), this resulted in better qualitative agreement with

the MCNP calculations. The experimental data and numerical predictions for foils 1-5 were all within 16% relative error of each other after this normalization was performed.

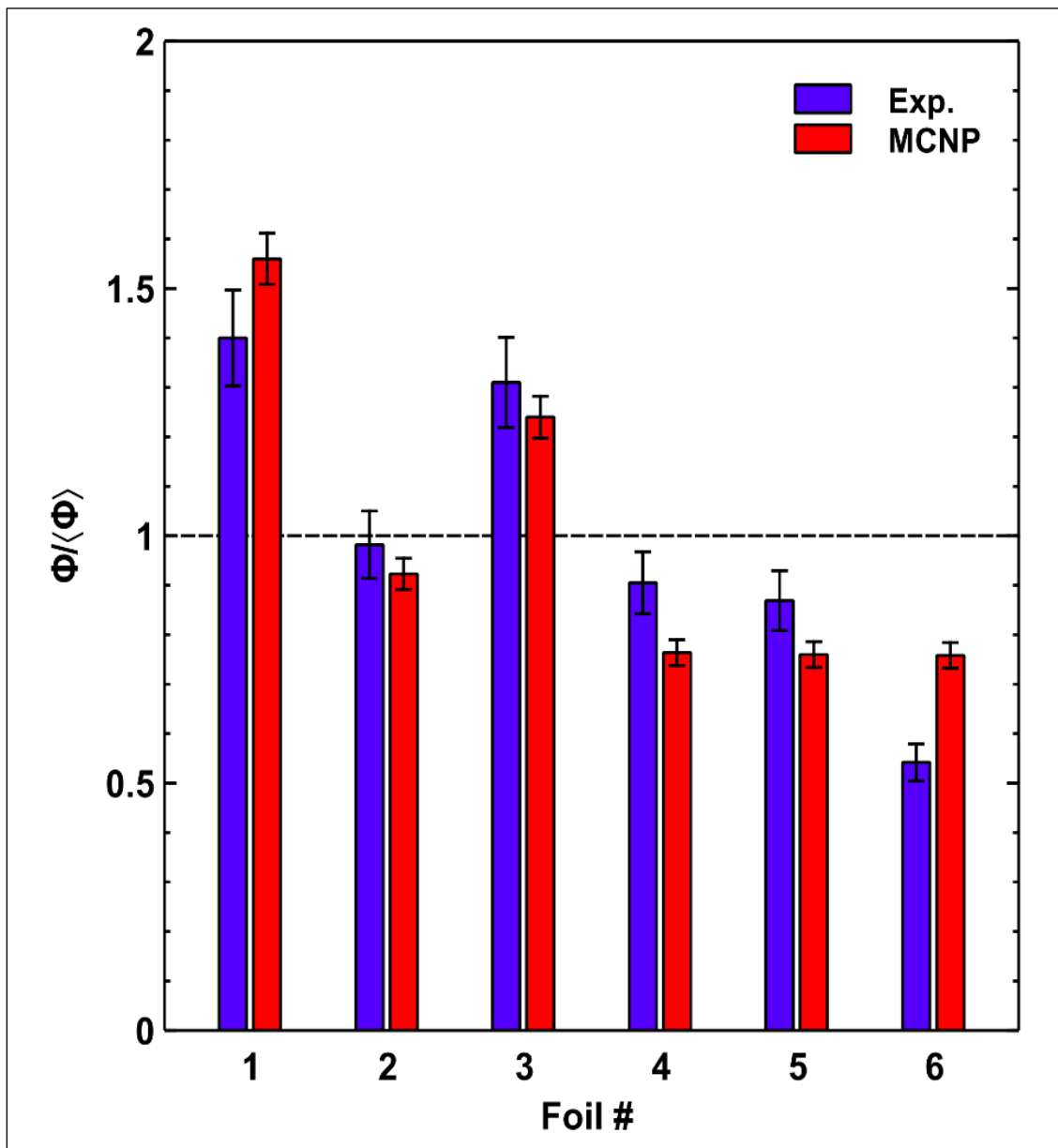


Figure 3.3. The Total Neutron Fluence per Activation Foil Normalized by the Average Fluence for all Foils. Comparison Between the Experimental (Blue) and MCNP Calculations (Red) Indicate Reasonable Qualitative Agreement in the Spatial Distribution of the Flux Across the Surface of the Beam Port Opening.

Additional discrepancies may result from differences in how reactor power is defined. At the MSTR, reactor power measurements are made with a pair of Compensated Ion Chambers positioned on either side of the core. Although they are calibrated to the reactor thermal power, it would be more accurate to say that they measure neutron flux at two particular points in the reactor pool that correlate well with reactor power. As such, the correspondence between measured reactor power and the power that factors into the burnup calculation through the fission rate is not exact. The effect of flux tilting from control rod burnup as well as rod shadow can result in (usually small) perturbations to the flux profile in the core relative to the ion chambers. Additional uncertainties in the experimental data not included in the present analysis could include variations in the foil thickness and Cd thickness, the reproducibility of the foil positioning in front of the beam port opening and variations in the flux profile between experiments due to neutron poison effects.

#### 4. EVALUATION OF NDP CAPABILITY AT MSTR

A model of a simple NDP system was developed for the Monte Carlo N-Particle code version 6 (MCNP6). The Monte Carlo simulations were based on a conceptual CAD model for the depth profiling system illustrated in Figure 4.1. The sides of the chamber body contains two aluminum windows for the neutron beam entrance and exit. Aluminum is chosen to avoid the production of long lived activation products. The detector and sample were located in a cylindrical steel vacuum chamber of 15 cm radius and 30 cm height. A small port is included for exchanging samples.

The actual MCNP model in the present work is a simplified version of the CAD model. Details about the chamber dimensions, number of viewports and flanges, vacuum conditions etc., while important in the construction and actual operation of such a system, are irrelevant to the radiation transport simulations. The MCNP model consists of a Si detector, boron containing sample, within the chamber body. The neutron beam is treated as a 0.0253 eV monodirectional disk source inside the chamber. The boron sample is located in the path of the neutron beam. The neutron flux from the source was normalized to the flux determined from experiment (Section 3). To cover the whole area of the sample, the thermal neutron beam has a radius of 3 cm. The active region of the charged particle detector was modeled as a 100  $\mu\text{m}$  thick Si cylinder, facing the sample on the side opposite the incident neutron beam. The sample, the beam, and the detector were placed in a line along the beam axis. A pulse height tally (F8) was used to mimic the response of an energy-sensitive detector and spectroscopy signal processing circuit. The F8 tally records deposited energy per alpha particle history and generates a histogram of

frequency vs. deposited energy. Neutron and alpha physics were included in the simulations. Both the regions inside and outside the chamber were modeled as void but the neutron and alpha importance outside of the chamber was 0 while inside it was 1.

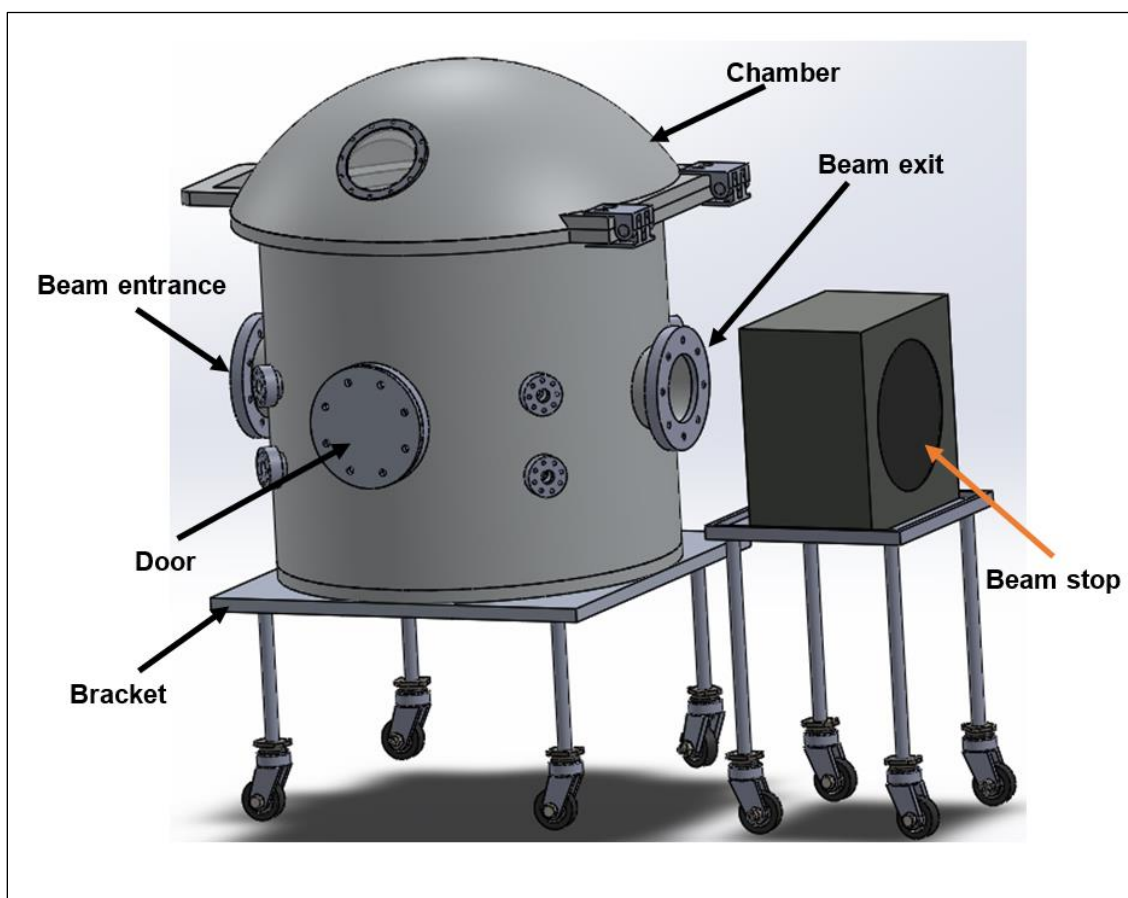


Figure 4.1. Basic Design of the NDP Instrument.

The first sample simulated was a borosilicate glass NIST standard (SRM-93a) was modeled. The standard is used for NDP channel energy calibration. SRM-93a is a 32.2 mm diameter by 6.3 mm thick wafer with a uniform distribution of 12.5 wt%  $B_2O_3$

throughout the sample depth. The alpha spectrum (F8 tally) of the NIST standard (SRM-93a) is shown in Figure. 4.2 with the  $\alpha_1$  and  $\alpha_2$  peaks indicated.

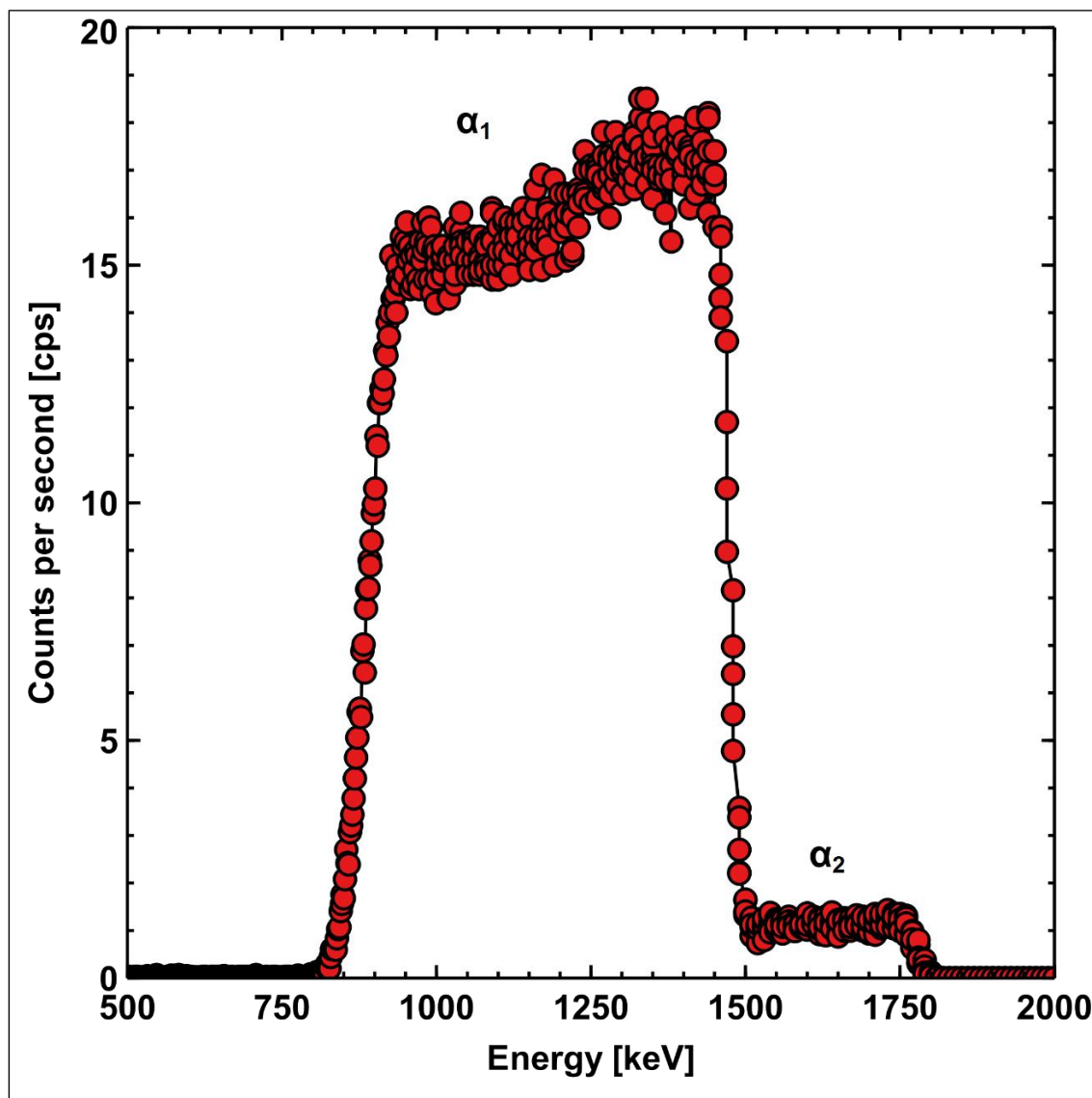


Figure 4.2. Alpha Energy Spectrum of the SRM-93a NIST Standard.

The second specimen studied comprised a silicon wafer with a borophosphosilicate glass (BPSG) film and second silicon layer deposited on top to

create a Si/BPSG/Si sandwich. The specimen dimensions were  $2\text{ cm} \times 2\text{ cm} \times 1\text{ mm}$ . The thickness of the BPSG layer was 850 nm and was composed of  $\text{P}_2\text{O}_5$ ,  $\text{B}_2\text{O}_3$ , and  $\text{SiO}_2$ . The Si top layer was 20 nm in thickness. Figure 4.3 shows the energy spectrum of the BPSG sample.

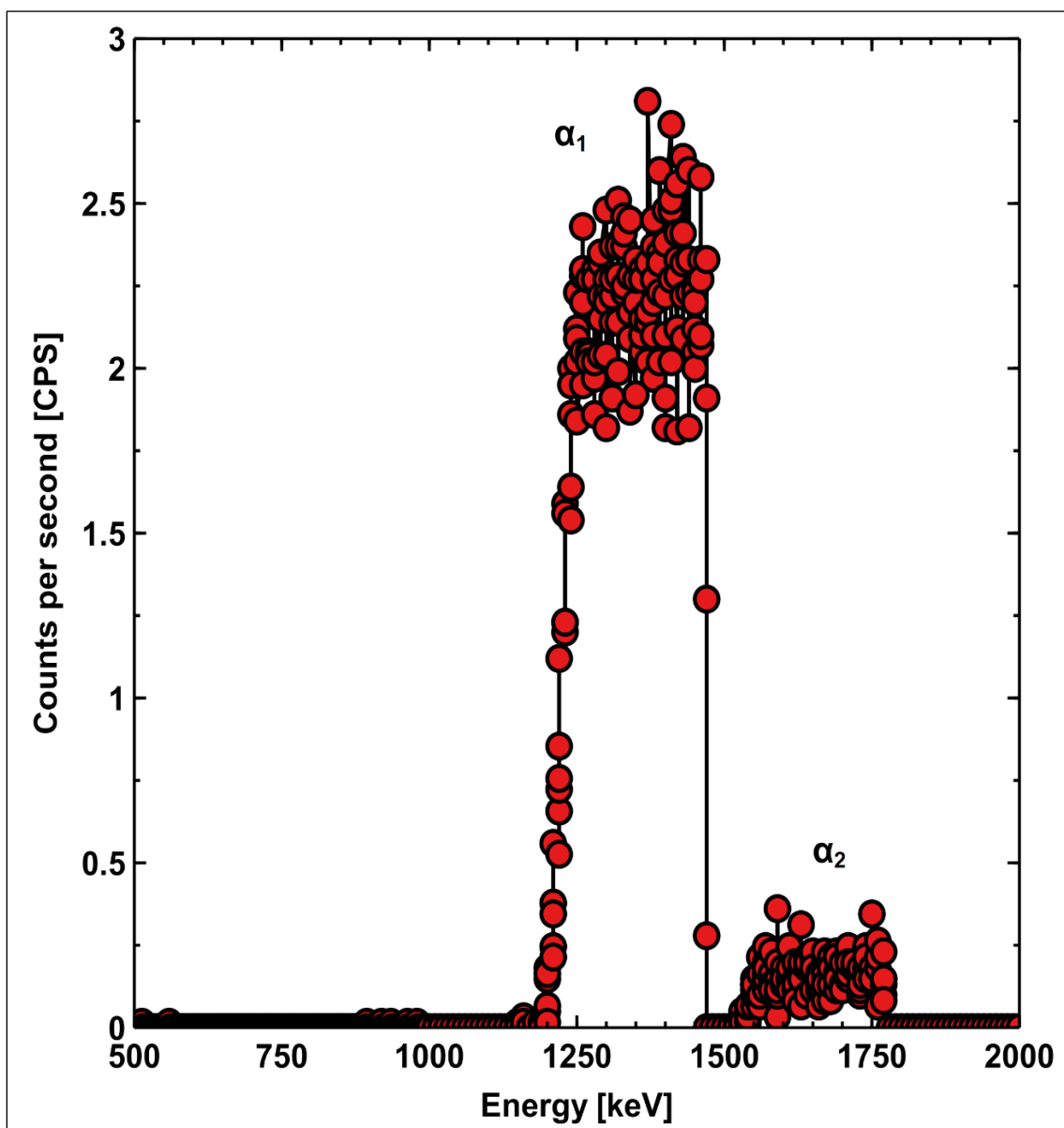


Figure 4.3. BPSG Alpha Energy Spectrum.

The depth profile of  $^{10}\text{B}$  was determined using the 1472 keV  $\alpha_1$  peak from the BPSG spectrum. The depths were obtained based on the residual energy versus path length calculated using the Stopping and Range of Ions in Matter (SRIM) program [106].

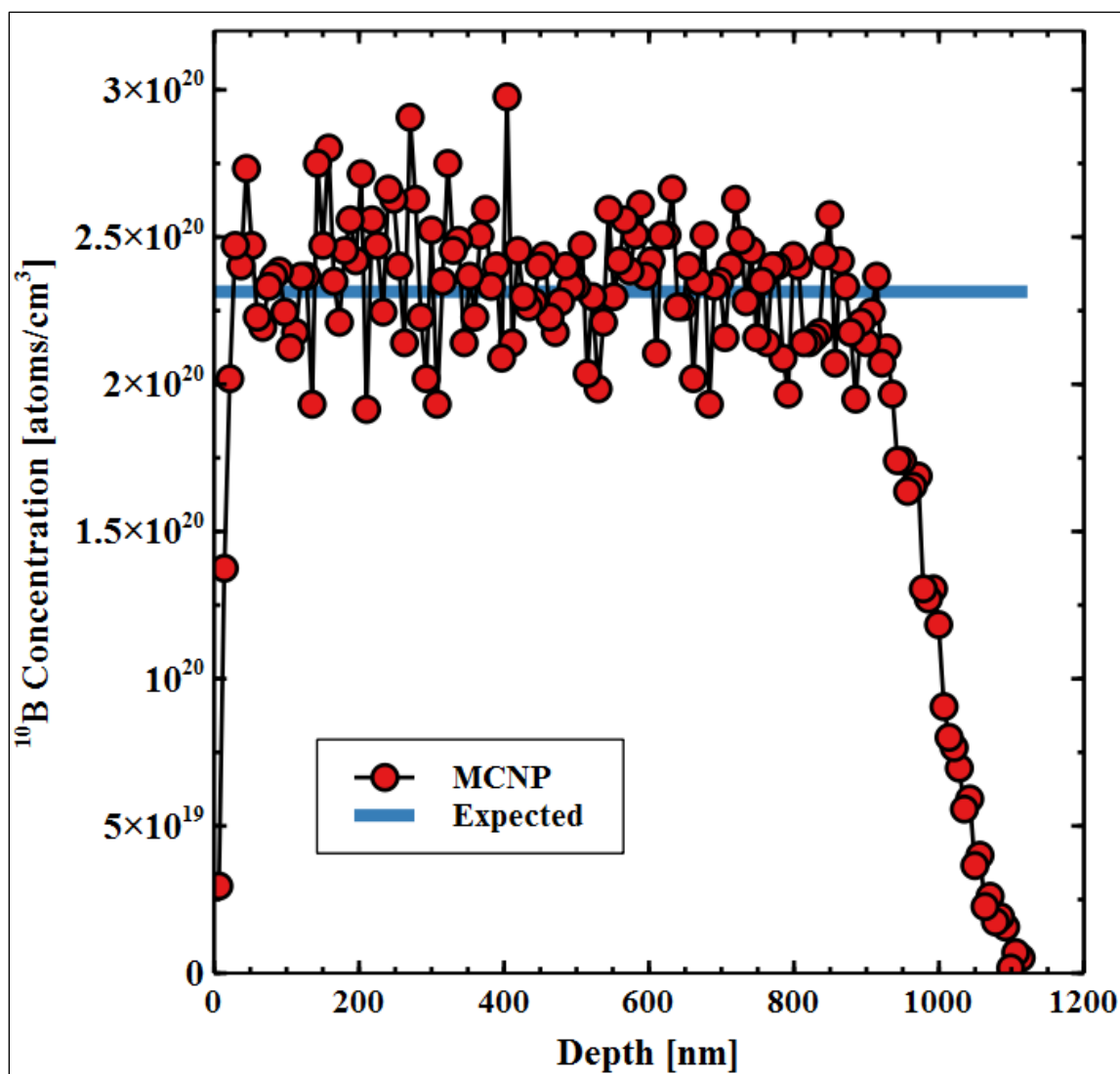


Figure 4.4. Concentration of BPSG as a Function of Depth Obtained from MCNP.

Figure 4.4 shows the resulting depth profile obtained from analyzing the MCNP F8 tally. The calculated depth showed excellent agreement with the expected boron

concentration to a depth of about 800 nm. Beyond this, straggling effects and other non-linearities not considered in the stopping tables result in an underestimate of the boron concentration.

The SRM 93a standard has a count rate of 2 cps per atomic percent per channel [CPS/at%/channel]. This implies that for such a specimen, an acquisition time of about 1 hour at full power would be sufficient to achieve a relative uncertainty of <1% assuming Poisson statistics. The BPSG sample had a predicted count rate of ~1.5 counts per second per atomic percent per channel [CPS/at%/channel]. Because of the slightly lower boron concentration, 2 hours at full power would be sufficient to achieve a relative uncertainty of <1% assuming Poisson statistics. It is worth noting that in both specimens the boron concentration was not at trace levels. Therefore, NDP measurements at the MSTR beam port would probably be infeasible for trace boron measurements due to the relatively low neutron flux.

Despite the low flux compared to higher power research reactors, these results indicate that the MSTR beam port is likely adequate for some boron Neutron Depth Profiling analysis. Quantitative profiling is possible within a few hours. A major disadvantage of the current core configuration is the lower neutron flux at the beam port. The MSTR fuel is further from the beam tube in the current core configuration (see Figure 1.7). However, if the MSTR fuel is moved back towards the beam tube as shown in Figure 1.8, characterization can be done within shorter time. Indeed, previous measurements at the beam port for an older configuration yielded a total flux of  $10^8 \text{ cm}^{-2} \text{ s}^{-1}$ . With such a flux, trace analysis is more within reach.

## 5. AUTOMATED DATA PROCESSING OF NEUTRON DEPTH PROFILING SPECTRA USING AN ARTIFICIAL NEURAL NETWORK

### 5.1. OVERVIEW

This purpose of this section is to investigate the applicability of ANNs in automated analysis of Neutron Depth Profiling data. An advantage of such an approach would be to eliminate the need for reference to a specific stopping power table or formula. The Monte Carlo N-Particle version 6 (MCNP6) radiation transport code [104] was used to model neutron and alpha transport in a NDP system. In the model, a NIST standard was included and used to compare the ANN predictions with traditional data analysis using stopping tables. The ANN model was trained with data sets generated from MCNP simulations. Each simulation calculated the NDP alpha energy spectrum from a specimen with a randomly generated boron depth profile. The trained ANN was used for automated analysis of the boron concentration within the SRM2137 standard.

### 5.2. METHODOLOGY

The methodology of the traditional and automated models using MCNP6 and ANN are illustrated below.

**5.2.1. Modeling.** To compare the performance of the data analysis procedures using the ANN model and the traditional method (stopping tables), an analog of the NIST standard, SRM-2137, was modeled in MCNP6.

SRM-2137 is a single crystal silicon substrate implanted with  $^{10}\text{B}$ , often used for testing the performance of both NDP system and in the concentration calibration of Secondary Ion Mass Spectrometry (SIMS) systems. The continuous boron depth profile

was approximated in MCNP by stacking 10 nm thick Si layers with varying boron concentration.

**5.2.2. Artificial Neural Network.** A supervised back-propagation neural network (BPNN) was used. In a BPNN, the connection weights for the input, hidden, and output layers of the network are iteratively adjusted to minimize the overall error of the prediction with respect to a reference result [107]. Figure 5.1 shows the structure of the BPNN used to analyze NDP spectra. This model uses the Levenberg-Marquardt (LM) algorithm. Each neuron in each layer is interconnected with all neurons in the previous layer and the following layer. Each bin of the input alpha spectra (histograms) was mapped onto [0,1] by normalizing the spectra. 96 energy bins corresponding to the  $\alpha_1$  energy peak were used in the input data sets. Tangent sigmoid functions were used to map the output of the hidden layer neurons onto [0,1]. The input datasets (training, validation and testing) were generated from MCNP simulations of NDP spectra of 300 randomly generated specimens. Each specimen contained 10 layers of Si with random concentrations of  $^{10}\text{B}$  added. The boron concentrations were uniformly sampled from the range  $6.8 \times 10^{16}$  to  $8.5 \times 10^{19} \text{ cm}^{-3}$ . Each layer was 35 nm thick. The training data input consisted of 96 neurons corresponding to the number of channels in the input data, the hidden layer contains 50 neurons and the output layer contains 10 neurons corresponding to the 10 layers of the specimen.

Validation prevents overfitting when the network tends to memorize insignificant details of the training data [108]. To develop the ANN model, the MCNP dataset of the NDP system was divided into three subsets: training, validation, and testing in proportions of 70%, 15%, and 15%, respectively.

The testing dataset was used to evaluate the performance of the ANN model at different learning stages. Training stops when the error of the testing set increases.

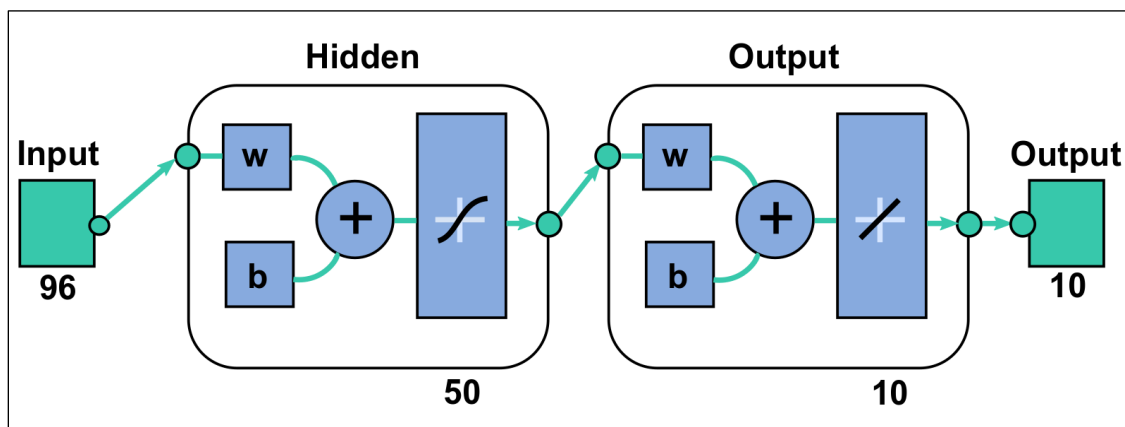


Figure 5.1. Artificial Neural Network Design for Analyzing  $^{10}\text{B}$  NDP Spectra.

### 5.3. RESULTS AND DISCUSSION

Figure 5.2 shows the alpha energy spectrum of the SRM-2137 standard. Alpha peaks can be seen at 1472 keV and 1776 keV.

The depth profile of  $^{10}\text{B}$  was determined using the 1472 keV  $\alpha_1$  peak from the SRM-2137 spectrum. The energy-to-depth conversion was based on the residual energy versus path length calculated using stopping tables from the Stopping and Range of Ions in Matter (SRIM) program [109].

The ANN developed in MATLAB using the Levenberg-Marquardt (LM) algorithm was trained with the aforementioned MCNP generated spectra. The performance of the network was evaluated using the Mean Squared Error (MSE) obtained during training and validation processes. Figure 5.3 shows the ANN predicted boron content (output), versus the actual boron content (target). The R value was 0.98223 for all

data sets, while the R values for training, validation and testing were 0.997, 0.97069, and 0.92562, respectively.

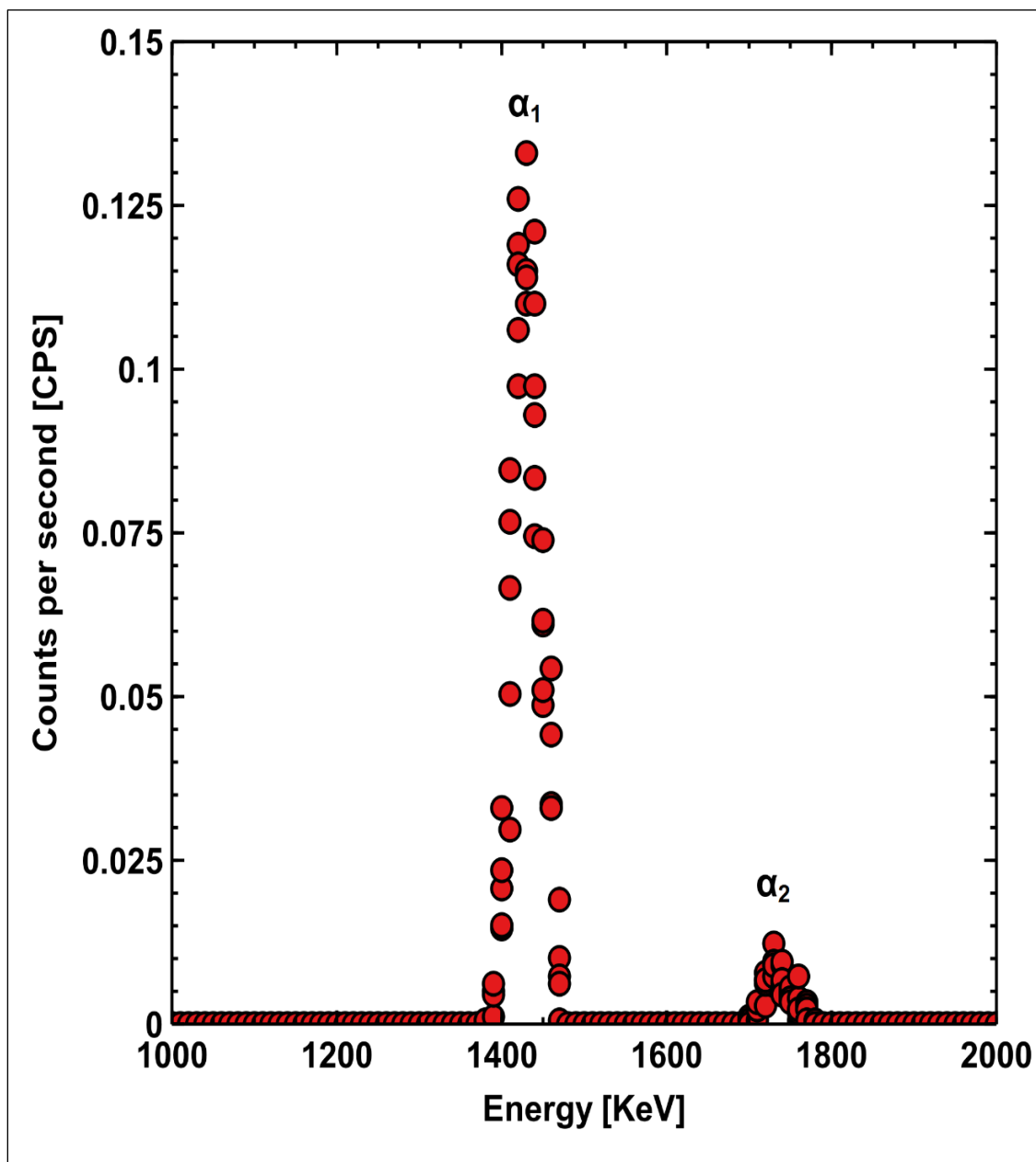


Figure 5.2. The Alpha Energy Spectrum of NIST Standard SRM-2137.

The performance of the model is shown in Figure 5.4. The validation process was stopped once the MSE was minimized.

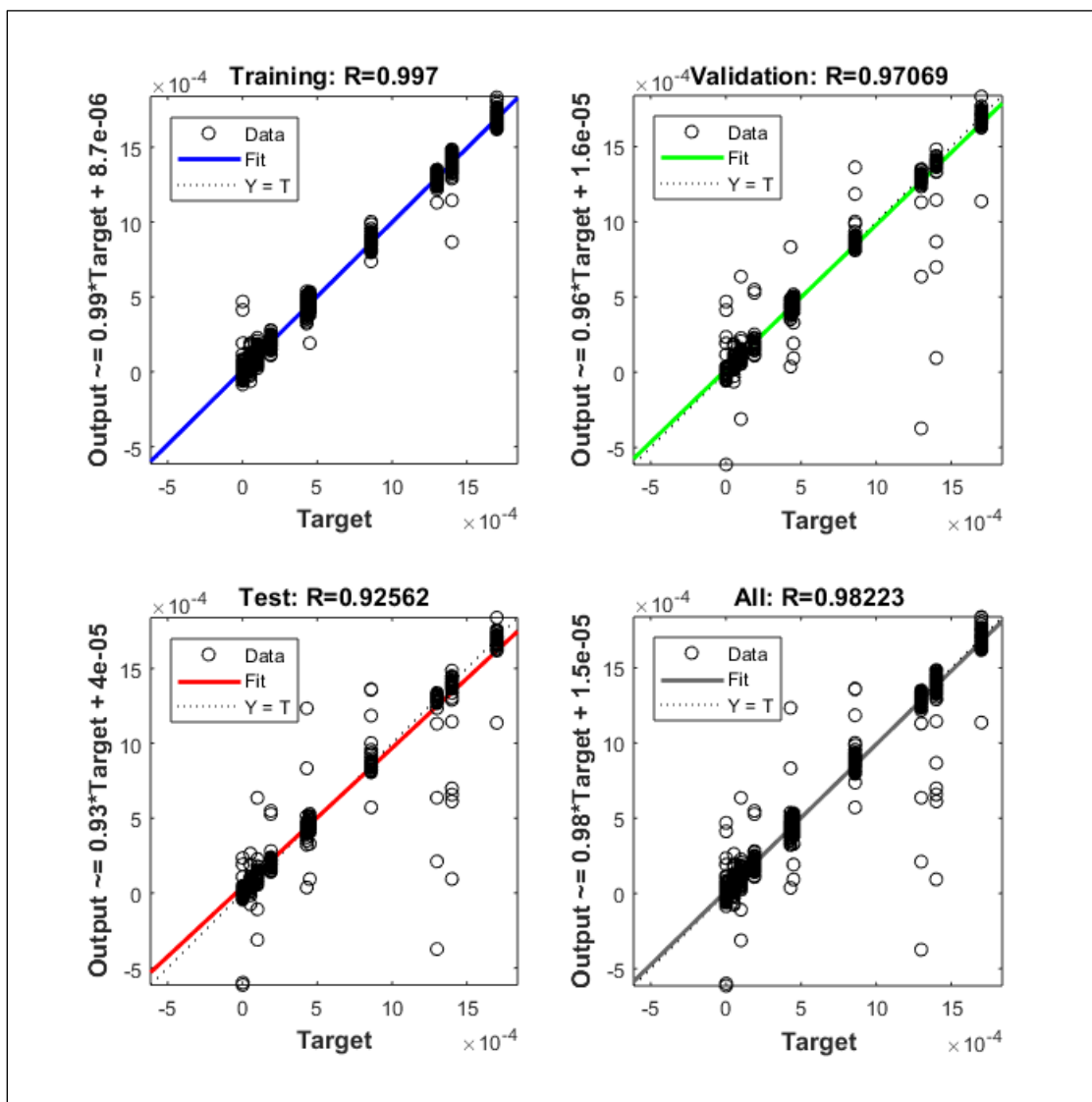


Figure 5.3. Crossplot of Predicted and Actual Datasets of the Boron Samples for Training, Validation, Testing, and all Datasets.

Figure 5.5 shows the boron depth profile in the SRM-2137 standard. The profile was determined using both the traditional method of relating depth to energy loss using

stopping tables and with the proposed ANN method. The results of both methods can be compared to the accepted profile (black curve). Both methods give comparably accurate results with the ANN method slightly overestimating the concentration and the traditional method slightly underestimating the concentration.

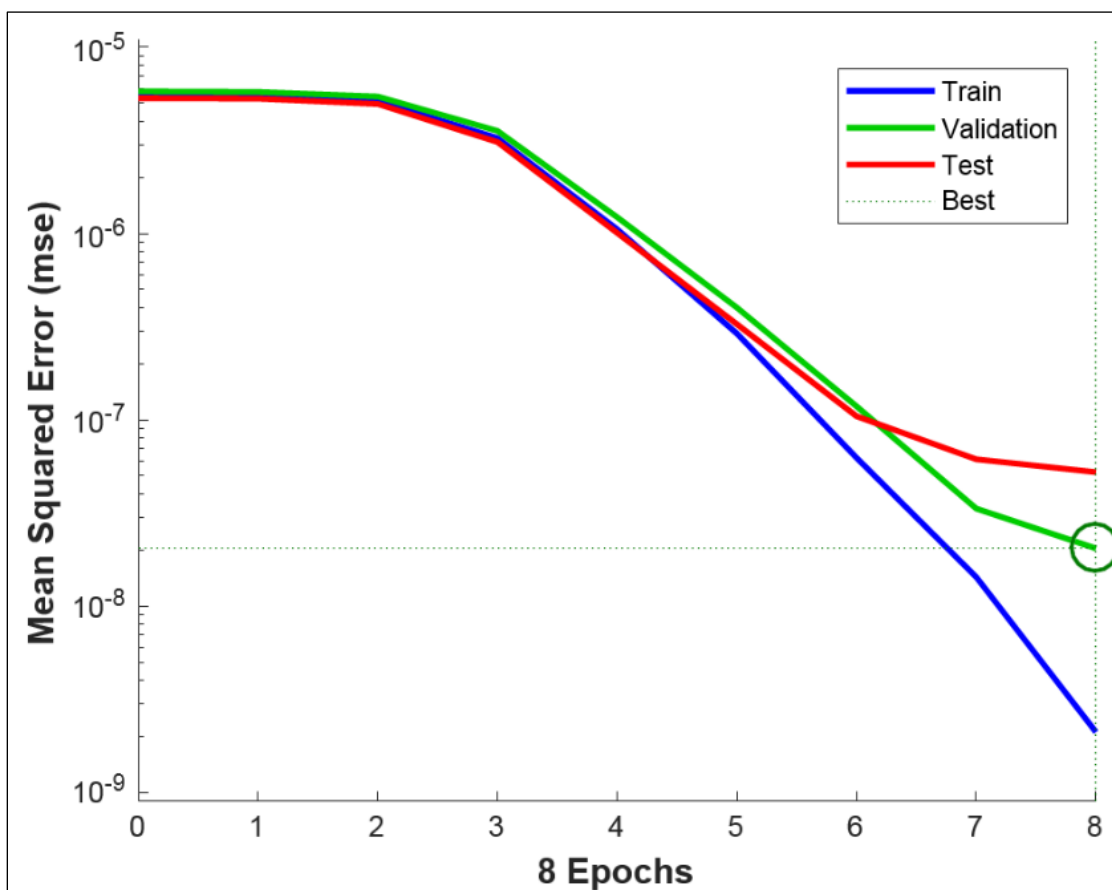


Figure 5.4. Mean Squared Error Values During Training.

Further improvement of the ANN result may be possible with additional training. It is interesting to note that the ANN method does not rely on stopping tables. The stopping power appears only indirectly through the radiation transport calculations. Therefore, energy loss physics in the radiation transport calculations could, in theory,

bias the ANN. On the other hand, the physics of the energy loss is more “complete” in the simulations in the sense that straggling, backscattering and solid angle effects are implicitly accounted for in the simulations.

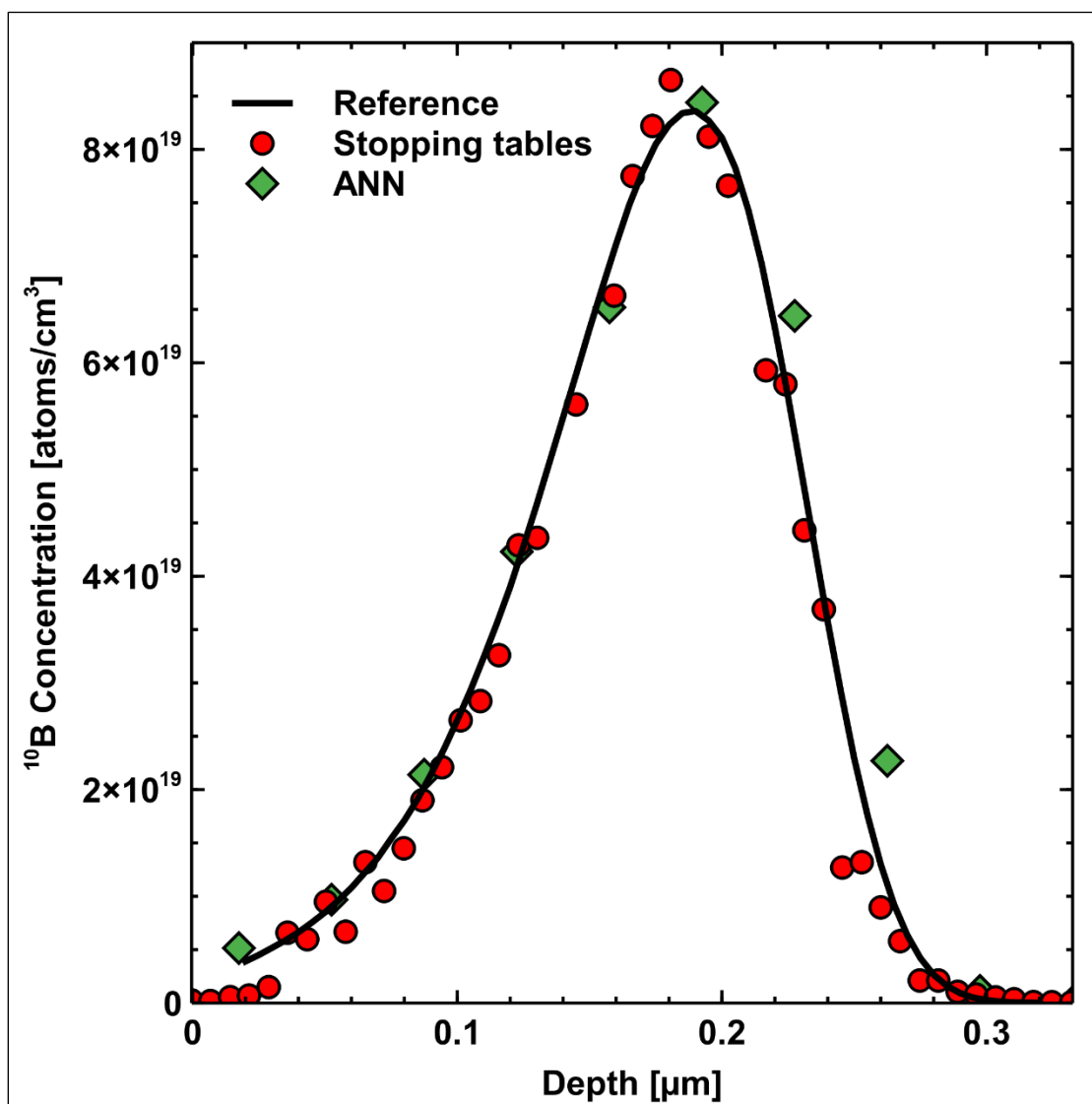


Figure 5.5. The Boron Depth Profile for SRM-2137. The Black Curve is the Accepted Profile for the Reference. The Red Circles Represent the Depth Profile Resulting from MCNP Generated Alpha Spectra Processed with Stopping Tables. The Green Diamonds Represent the Depth Profile Resulting from MCNP Generated Spectra Processed with the ANN.

It would be possible, in principle, to train the ANN with experimental data provided the set of specimens was large and already well characterized. This would also train the ANN to automatically adjust for other instrumental parameters such as dead time, detector resolution, detector nonlinearities and imprecisions in apparatus geometry.

## **6. NIXE: NEUTRON DEPTH PROFILING COUPLED WITH PARTICLE INDUCED X-RAY EMISSION**

### **6.1. OVERVIEW**

As mentioned in Section 1, a NDP measurement produces the depth profile of a specific isotope of a specific element in the surface of a specimen. Though the element (say boron or lithium) can be profiled by assuming the isotope is present in its natural abundance, little to no information about the distribution of other elements in the matrix can be gained. This section proposes a way to use secondary radiation emitted during the NDP measurement to obtain such additional information. This technique is coupled Neutron Depth Profiling with Particle Induced X-Ray Emission. Hereafter it is called NDP-PIXE or NIXE for short.

As mentioned in Sections 1 and 2, in a PIXE measurement, a charged particle undergoes stopping as travels through the material. The charged particle interacts with other atoms in the surrounding matrix, transferring energy to core shell and valence electrons through ionization collisions and collective excitation processes. The energies and intensity of the characteristic X-rays produced through charged particle-induced core shell ionization is related to the elemental composition of the material. The main difference between traditional PIXE and NIXE is that in PIXE the particle is produced via an external source (e.g. alpha emitter or ion beam) while in NIXE the particle is generated internally.

Table 6.1 below lists some of the possible reactions for NDP analysis. Monte Carlo radiation transport simulations of charged particle generation and transport in an NDP apparatus was coupled with an analytical model describing characteristic X-ray

generation to predict the coincidence count rates of alpha particles and characteristic K-shell X-rays of Si, P, Na, and O a layered glass material. The objective of this work is to demonstrate the feasibility of combining NDP and PIXE (NIXE) into a compound non-destructive analytical technique.

Table 6.1. Possible Nuclear Reactions for NDP Analysis.

Reaction	Energy of Emitted Particles [keV]	Approximate Range in Silicon [ $\mu\text{m}$ ]	Cross Section [b]
${}^3\text{He}(n,p){}^3\text{H}$	572	7.2	5333
${}^6\text{Li}(n,\alpha){}^3\text{H}$	2055	7.3	940
${}^{10}\text{B}(n,\alpha){}^7\text{Li}$	1472	5.2	3837
${}^{14}\text{N}(n,p){}^{14}\text{C}$	584	7.4	1.83
${}^{17}\text{O}(n,\alpha){}^{14}\text{C}$	1413	5.0	0.24
${}^{33}\text{S}(n,\alpha){}^{30}\text{Si}$	3081	12.5	0.19
${}^{35}\text{Cl}(n,p){}^{35}\text{S}$	598	7.6	0.49

## 6.2. THEORY

In an NDP apparatus, a thermal neutron is captured by a target nucleus producing a light charged particle (e.g. p,  $\alpha$ , t, h). As the charged particle exits the material, it loses energy through stopping (primarily in the form of electronic stopping for swift light ions). The measured energy is then used to determine the particle's starting depth through stopping tables or calculations. In the following discussion the particle is referred to as an alpha particle but the analysis is fairly general and could apply to other swift light ions. Suppose the alpha particle is produced at a depth  $x$  from the exiting surface of the specimen (see Figure 6.1). If it leaves the specimen at an angle  $\lambda$  relative to the surface

normal and strikes a charged particle detector, the kinetic energy measured by the detector is given by

$$E(L) = E\left(\frac{x}{\cos \lambda}\right) = f^{-1}\left(\frac{x}{\cos \lambda}\right) \quad (15)$$

$f$  is a monotonic function describing the distance the particle with initial energy  $E_0$  has traveled after it has slowed to an energy of  $E$  (i.e. after it has lost  $E_0 - E$ ). Assuming that the particle is at an energy where electronic energy loss dominates and straggling is relatively minor, the distance traveled can be approximated by

$$l = f(E) \cong \int_E^{E_0} \frac{dE}{S(E)} \quad (16)$$

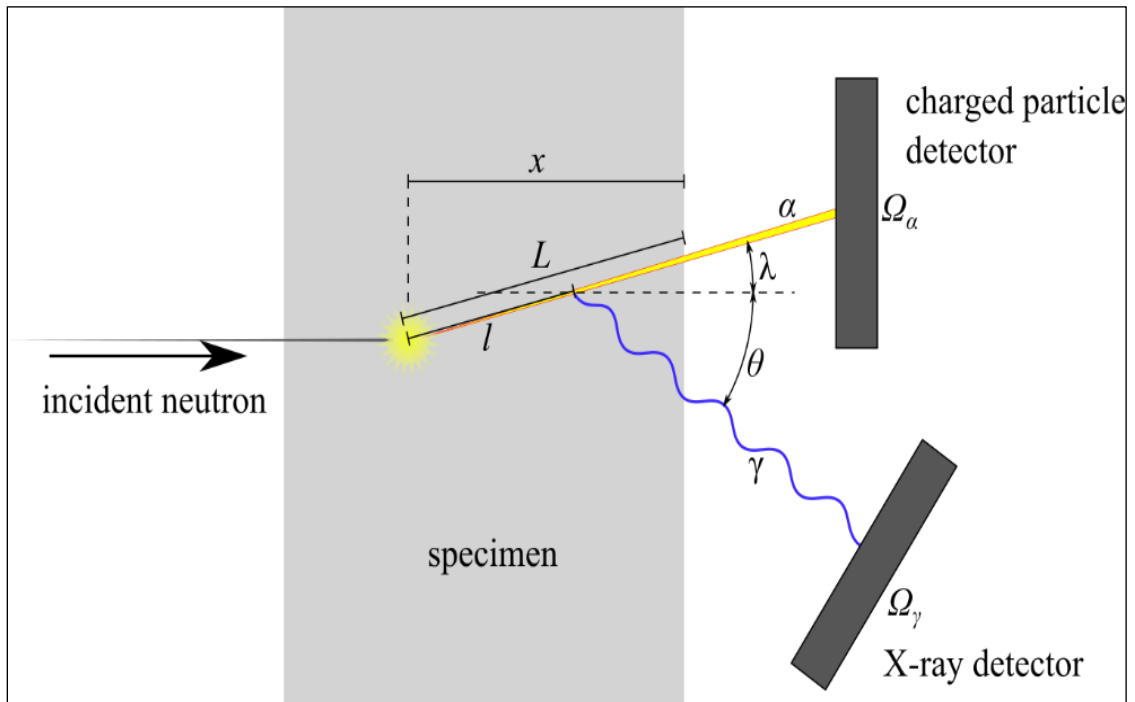


Figure 6.1. Depiction of the NDP and PIXE Acquisition Process.

The rate at which charged particles in the energy interval  $(E, E + dE)$  reach the charged particle detector is

$$R(E)dE = \frac{\Omega_\alpha}{4\pi} A\sigma_t\phi_t(x)N(x)\delta(L - f(E))dx \quad (17)$$

the first term,  $\frac{\Omega_\alpha}{4\pi}$ , accounts for the probability that a particle, isotropically emitted, reaches the detector.  $A$  is the area of the neutron beam,  $\sigma_t$  is the thermal averaged neutron absorption cross section and  $\phi_t$  is the thermal neutron flux.  $N(x)$  is the depth-dependent target number density (the NDP depth profile in other words). The delta function accounts for the one-to-one energy-depth relationship (again ignoring straggling).

Implicitly, it is assumed that the detector solid angle  $\Omega_\alpha$  and specimen area are sufficiently small that a single value of  $L$  may be used. Alternatively one could write an expression in terms of a differential solid angle,  $d\Omega_\alpha$ . In that case, angular dependence also appears in both  $L$  and  $\lambda$  and the entire rate must be integrated over all solid angles. For the sake of simplicity, it is assumed that the solid angle and sample area are both small enough to approximate those terms as constants. Substituting in  $x$  for  $L$  gives

$$R(E)dE = \frac{\Omega_\alpha}{4\pi} A\sigma_t\phi_t(x)N(x)\delta\left(\frac{x}{\cos\lambda} - f(E)\right)dx \quad (18)$$

Using the composition formula for delta functions gives

$$R(E)dE = \frac{\Omega_\alpha}{4\pi} A\sigma_t \cos\lambda \phi_t(\cos\lambda f(E))N(\cos\lambda f(E))dx \quad (19)$$

Over the micrometer depths that charged particles can be detected, the neutron flux should not vary greatly (except for exceptionally strong absorbers). Therefore it is reasonable to ignore the depth dependence on the flux entirely

$$R(E)dE = \frac{\Omega_\alpha}{4\pi} A\sigma_t \cos \lambda \phi_t N(\cos \lambda f(E)) dx \quad (20)$$

$\phi_t$  is now taken to mean the flux on the detector side of the specimen.

Given that

$$x = L \cos \lambda = f(E) \cos \lambda \quad (21)$$

$$dx = \cos \lambda \frac{df}{dE} dE = \frac{\cos \lambda dE}{S(E)} \quad (22)$$

The differentials can be made to cancel so that

$$R(E) = \frac{\Omega_\alpha}{4\pi} A\sigma_t \cos^2 \lambda \phi_t N(\cos \lambda f(E)) \frac{1}{S(E)} \quad (23)$$

Thus, provided one knows the depth-dependent target density, a table of  $f$  values as a function of energy, the neutron flux, the detector solid angles, the rate at which the particles deposit energy in the detector can be estimated. In practice, most charged particle energy spectroscopy systems use multichannel analyzers to acquire spectra. The count rate in a given channel with average energy  $E_i$  and channel width  $\Delta E$  is

$$C_i \approx \frac{\Omega_\alpha}{4\pi} A\sigma_t \cos^2 \lambda \phi_t N_i \frac{1}{S_i} \Delta E \quad (24)$$

$$N_i = N(x_i) = N(\cos \lambda f_i) \quad (25)$$

$$f_i = f(E_i) \quad (26)$$

$$S_i = S(E_i) \quad (27)$$

Equation (24) may be used to estimate the count rate for a given specimen at a reactor beam port with a known thermal neutron flux.

Turning the attention to characteristic X-rays, the goal in the following derivation is to show that it is possible to acquire the elemental depth profile using PIXE if given prior knowledge of the origin of the alpha particle inducing the X-ray signal. Through

coincidence counting one can simultaneously profile a particular element (such as B or Li) and also use a detected alpha particle to tag characteristic X-rays collected within a coincidence time window and correlate those X-rays with a particular depth range for the interaction.

Suppose a charged particle passing through a thin slab of thickness  $dl$  has an energy  $E$ . As it passes through the slab, it will ionize some of the core shell electrons in the atoms in the slab. If element  $i$  has atomic number density,  $n_i$ , then the number of electrons ejected from shell  $s$  (i.e. number of K, L, M-shell holes) of element  $i$  is given by

$$\#e_s^- = n_i \sigma_{i,s}(E) dl \quad (28)$$

$\sigma_{i,s}$  is the  $s$ -shell ionization cross section. It depends on the ion specie and energy.

If the slab is thick then one must integrate this expression over the length of the ion's trajectory. The total rate,  $R_{i,s}$ , of  $s$ -shell ionization for a charged particle born at depth  $x$  and traveling a length  $L$  before reaching the specimen surface is

$$R_{i,s}(x) = \int_0^L n_i(l) \sigma_{i,s}(E) dl \quad (29)$$

Transforming from variable  $l$  to energy  $E$

$$R_{i,s}(x) = \int_0^L n_i(f(E)) \sigma_{i,s}(E) \frac{df}{dE} dE = \int_{f^{-1}\left(\frac{x}{\cos \lambda}\right)}^{E_0} n_i(f(E)) \sigma_{i,s}(E) \frac{dE}{S(E)} \quad (30)$$

The above expressions are not unlike the integrals appearing in the X-ray yield in traditional PIXE apart from the fact that the yield now depends on depth  $x$ . A matrix attenuation term could also be included in this integral but is ignored here for simplicity.

The X-ray photopeak yield for such an event can then be determined by multiplying by the fluorescence yield,  $\omega_s$ , the X-ray detector solid angle,  $\Omega_\gamma$ , and detector efficiency  $\varepsilon_s$ .

$$C_{i,s}(x) = \frac{\Omega_\gamma}{4\pi} \omega_s \varepsilon_s R_{i,s}(x) \quad (31)$$

This expression gives the X-ray counts for a particle traveling along a known path. For a system where both alpha and X-ray detectors are set up in a coincidence circuit such that X-rays are only counted when an alpha particle is detected, Equation (31) gives the expectation value of the number of s-shell X-ray counts per alpha count in element  $i$ .  $x$  is determined from the energy of the alpha particle deposited in its detector through stopping tables (NDP). Naturally, due to the stochastic nature of the process, many such coincident events must be acquired and X-ray spectra sorted into to  $x$  bins to approximate  $C_{i,s}(x)$  as a histogram. It is worthwhile to note that the derivative of  $C_{i,s}(x)$  gives the depth profile of the elements,  $n_i$

$$\frac{dC_{i,s}(x)}{dx} = \frac{\Omega_\gamma}{4\pi} \omega_s \varepsilon_s \frac{dR_{i,s}(x)}{dx} \quad (32)$$

$$\frac{dR_{i,s}(x)}{dx} = \frac{1}{\cos \lambda} n_i \left( \frac{x}{\cos \lambda} \right) \sigma_{i,s} \left( f^{-1} \left( \frac{x}{\cos \lambda} \right) \right) \frac{\frac{df^{-1} \left( \frac{x}{\cos \lambda} \right)}{dx}}{S \left( f^{-1} \left( \frac{x}{\cos \lambda} \right) \right)} \quad (33)$$

$$n_i \left( \frac{x}{\cos \lambda} \right) = \frac{\cos \lambda S \left( f^{-1} \left( \frac{x}{\cos \lambda} \right) \right)}{\frac{\Omega_\gamma}{4\pi} \omega_s \varepsilon_s \frac{df^{-1} \left( \frac{x}{\cos \lambda} \right)}{dx} \sigma_{i,s} \left( f^{-1} \left( \frac{x}{\cos \lambda} \right) \right)} \times \frac{dC_{i,s}(x)}{dx} \quad (34)$$

Though not particularly amenable to hand calculations, the above expression can be discretized and tabularized and solved using a computer. Doing this therefore gives the elemental depth profile. One conspicuous omission here is that in a nuclear reaction

involving the production of a light charged particle, another charged particle is emitted at 180 degrees to the detected particle. This energy is also deposited in the opposite direction of the detected charged particle and can also be expected to contribute to the X-ray yield. For example the 1.47 MeV alpha emitted in the  $^{10}\text{B} (n,\alpha)^7\text{Li}$  reaction also comes with a 840 keV  $^7\text{Li}$  nucleus emitted in the opposite direction. Though the Li nucleus will not travel as far, it can have a sizable contribution to the X-ray yield. As such the above expression should be modified to include the effect of the heavier charged particle. Lacking  $^7\text{Li}$  impact ionization cross sections, the numerical analysis to follow ignores the contribution to the light yield from  $^7\text{Li}$ .

### 6.3. METHODOLOGY

MCNP6 model of NDP was used to have two different elemental depth profiling. The data analysis of the PIXE is discussed below.

**6.3.1. Monte Carlo Radiation Transport.** Numerical predictions of the alpha particle energy spectrum from a layered glass specimen was obtained using the same MCNP6 model described in Sections 4 and 5 apart from the sample definition.

The sample was 2  $\mu\text{m}$  in thickness and composed of three layers of equal thickness and stopping power but different material compositions. The layer compositions are described in Table 6.2.

**6.3.2. Data Analysis.** The average charged particle energy as a function of distance traveled Equation (16) was calculated from stopping tables.

This information along with the simulated charged particle spectrum was used to determine the depth profile of the target nuclide. This same information, along with alpha

impact K-shell ionization cross sections and fluorescence yields was used to calculate the X-ray yields for K-shell ionization of each element and hence their depth profiles. The target material stopping power was determined using the Stopping and Range of Ions in Matter (SRIM) code of Ziegler et al. [106]. This code was used to calculate the stopping and range tables of the helium ions. In the analysis of the PIXE response a single stopping power curve was assumed for all layers of the specimen.

Tabulated ionization cross sections for each element were interpolated over a fine mesh of alpha energies. These data and the K-shell fluorescence yields were obtained from quasi-empirical PIXE data [110-112]. The expected yield of each element was calculated using the tabulated data, the element number density, depth-vs-energy relationship, and the alpha spectrum count rate through Equation (34). Angle cosines and geometric efficiency factors were taken to be unity. The X-ray counts were calculated using the energy interpolated from only the  $\alpha_1$  energy peak and the X-ray yield. Such a technique, while possible in theory, should have reasonable coincident counting statistics to be a practical quantitative technique.

Table 6.2. Sample Thickness and Composition.

Glass sample	Thickness ( $\mu\text{m}$ )	Composition and mass fraction
Borosilicate glass	0.67	$\text{B}_2\text{O}_3$ (0.2) $\text{SiO}_2$ (0.8)
Borophosphosilicate glass (BPSG)	0.67	$\text{P}_2\text{O}_5$ (0.2) $\text{B}_2\text{O}_3$ (0.2) $\text{SiO}_2$ (0.6)
Sodium borosilicate glass	0.67	$\text{Na}_2\text{O}$ (0.7) $\text{B}_2\text{O}_3$ (0.2) $\text{SiO}_2$ (0.1)

A number of factors will naturally influence this. These include: detector solid angles, material stopping power, composition and neutron flux. In fact, the two most important factors relating to the sensitivity of the technique and speed of spectral acquisition are  $C_{i,s}(x)$  and  $R(E)$ . These factors determine the ratio of coincidence counts to the total rate of alpha counts as well as the total acquisition time. Given the above expressions it is illustrative to use them to simulate the NIXE depth profile from a hypothetical measurement.

#### 6.4. RESULT AND DISCUSSION

Figure 6.2 shows the alpha energy spectrum generated from the pulse height light tally of alpha particles from  $^{10}\text{B}$  neutron interactions in the sample material. The spectrum contains both 1.47 MeV and 1.77 MeV alpha signals. The count rate was based on a beam port thermal neutron flux of about  $5 \times 10^6 \text{ cm}^{-2} \text{ s}^{-1}$ . This value is on the lower end of thermal neutron flux available at research nuclear reactors.

Figure 6.3 shows the K-shell coincident X-ray count rate per detected alpha particle for the K-shell X-rays of Si, O, P and Na. In other words given a detected alpha particle, Figure 6.3 gives the X-ray count rates as a function of measured alpha particle kinetic energy. The X-ray yield increases with the measured alpha energy for energies less than about 0.9 MeV paralleling the lower energy edge of the raw alpha spectrum Figure 6.2.

Above 0.9 MeV the yield decreases with energy. This is due to the fact that the alpha particle path length to the surface of the specimen decreases with increasing detected alpha energy. The shorter the path length, the less ionization and hence lower the

X-ray yield. . The highest counts of K-shell X-rays for Si, P, Na, and O were  $1.5 \times 10^3$ ,  $2.0 \times 10^2$ ,  $1.8 \times 10^4$ , and  $1.8 \times 10^5$ , respectively.

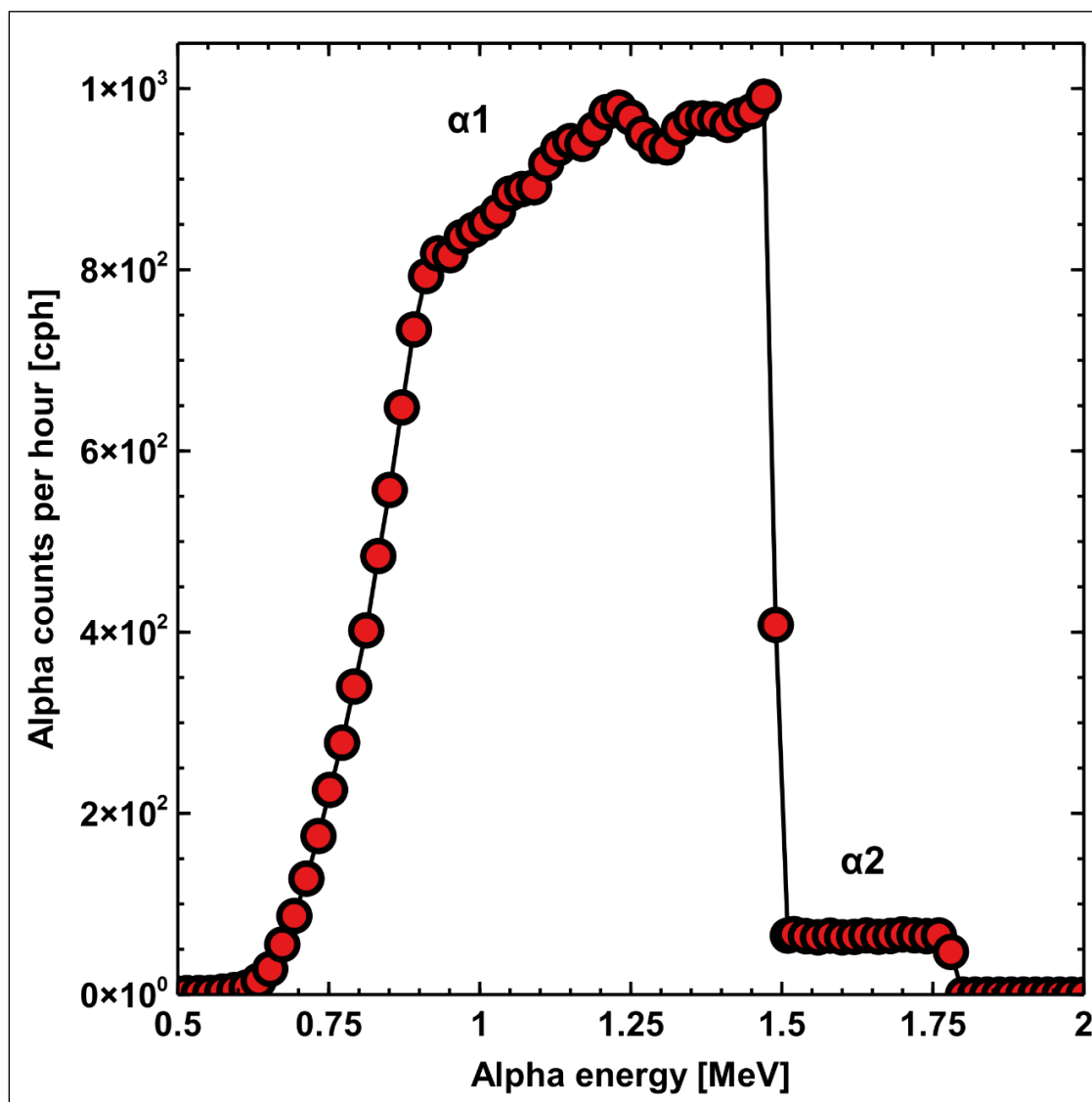


Figure 6.2. Alpha Spectrum from Boron NDP of a Multilayer Glass Specimen.

The wide range of K-shell yields can be mostly ascribed to difference in the magnitudes of the K-shell ionization cross sections and fluorescence yields, though

differing atomic number densities of the constituent elements also contribute to the different yields.

Figure 6.4 shows the depth profiles for each element in the sample. These were calculated by post-processing the MCNP alpha spectrum Figure 6.2 and the predicted coincidence count rates Figure 6.3 with Equation (34). The expected number densities (i.e. data input into the MCNP cell and material data cards) are overlaid for comparison. Conversion from alpha energy to depth was obtained using the stopping tables from SRIM. The uncertainties on the number densities depend on, among other things, the counting statistics of both the alpha spectrum and X-ray spectra. Because the number density of Equation (34) depends on the derivative in the number of X-ray counts with respect to depth, there is an inherent tradeoff between depth resolution and precision. In order to achieve less than 1% relative error in the depth profile, the difference in the number of coincidence events between any two consecutive energy channels would need to be at least 10,000, assuming Poisson counting statistics and ignoring other sources of systematic and random error. Given the alpha particle count rates of Figure 6.2 and using the relatively fine 20 keV energy resolution (hence depth resolution) of Figure 6.3, it would be possible to achieve relative uncertainties of between 1-10% in the Na and O depth profiles with acquisition times on the order of a few hours.

The Si and P profiles would likely require days owing to their lower coincidence count rates. One could, however, combine counts from multiple bins to achieve faster convergence of the depth profile, effectively trading shorter acquisition times for coarser depth resolution. At the extreme, one would simply sum up all coincident events to determine the average composition from the surface of the material to a depth of about

the stopping range of the alpha particle. More sophisticated data processing techniques (e.g. entropy minimization, machine learning) might also be considered for NIXE data analysis.

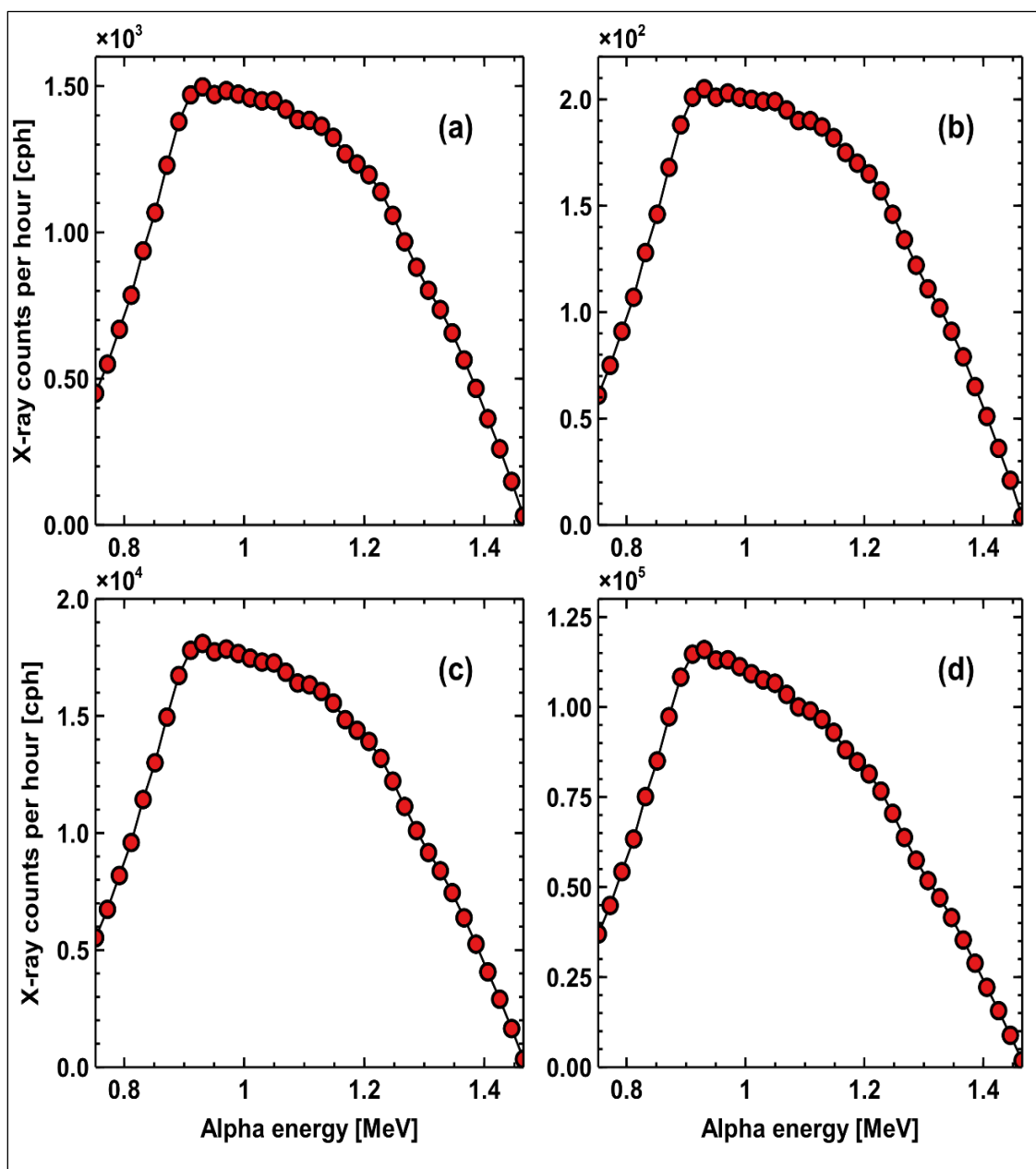


Figure 6.3. K-Shell Coincidence Count Rate for (a) Si (b) P (c) Na and (d) O.

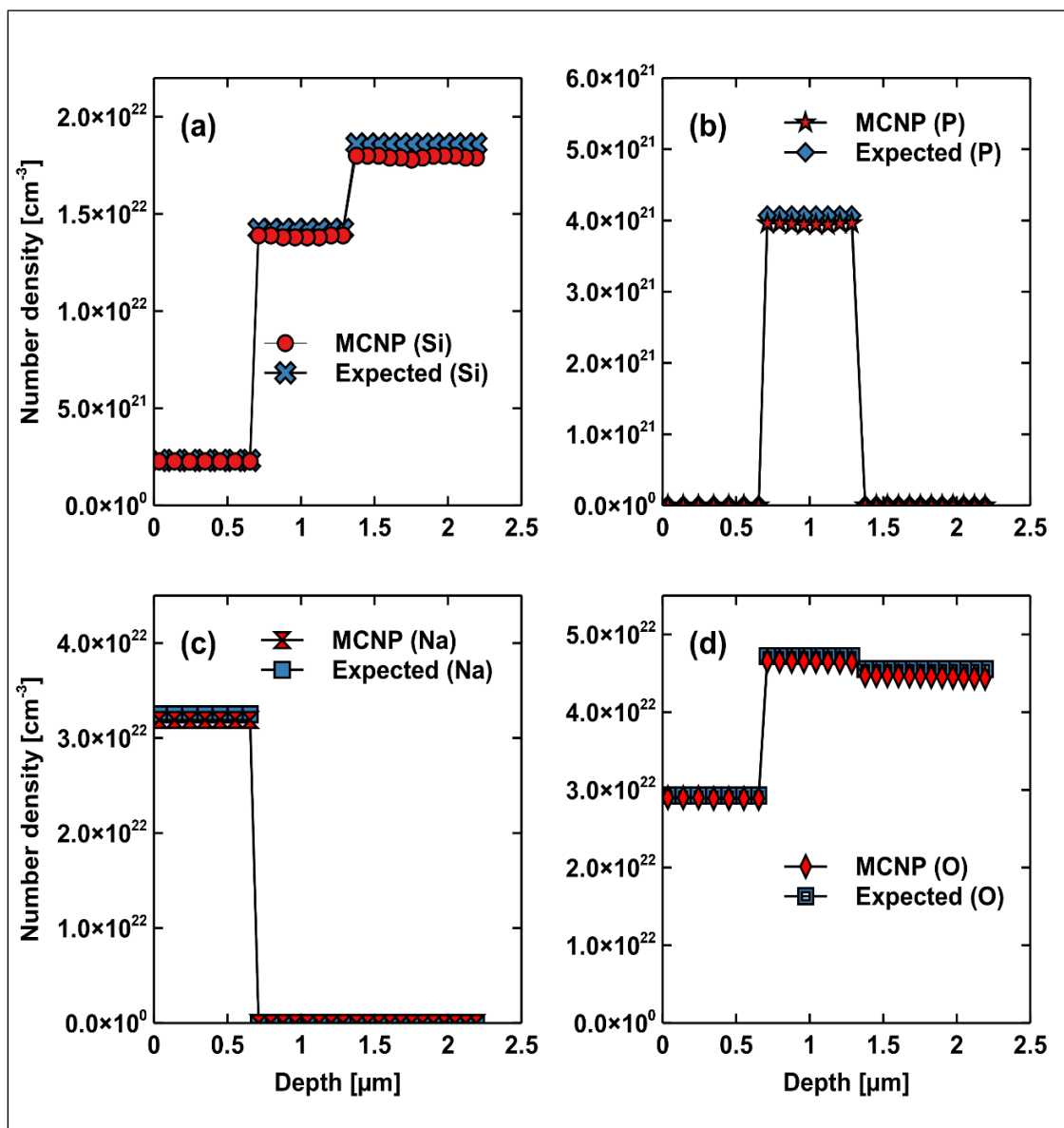


Figure 6.4. Depth Profile of (a) Si (b) P (c) Na and (d) O.

It should be kept in mind that the count rates of Figure 6.2 are also normalized to a very modest neutron flux of  $5 \times 10^6 \text{ cm}^{-2} \text{ s}^{-1}$ . This value is based on recent measurements at the beam port of the Missouri S&T research reactor (MSTR). The configuration of the fuel element at the time of those measurements was not optimized to provide a large flux

at the beam opening. Many other neutron beam port facilities can achieve orders-of-magnitude higher thermal flux [6, 84, 113].

Thus coincidence count rates and acquisition time are dependent on the available flux at the NDP facility in question as well as the specimen characteristics (ionization cross sections and neutron cross sections), detector efficiencies and desired depth resolution. Nevertheless, under favorable conditions, PIXE coupled to NDP appears to be a potentially practical non-destructive technique. More numerical modeling work and sensitivity analysis should be done to further investigate the possibility of incorporating this technique into current NDP systems for different materials.

## 7. CONCLUSIONS

This dissertation explores several concepts related to the design of a proposed Neutron Depth Profiling system for the Missouri University of Science and Technology Nuclear Reactor (MSTR). This involved first determining if such a system would exhibit high enough count rates to be of practical use. Original contributions to the technique were also put forth. These include a new experimental technique, NIXE, which couples Neutron Depth Profiling with Particle Induced X-Ray Emission and a new data processing approach using Machine Learning.

The thermal and epithermal neutron flux of the MSTR beam port and its spatial distribution was determined using Neutron Activation Analysis of bare and cadmium filtered gold activation foils. The experimental results were compared to Monte Carlo radiation transport predictions of the beam port flux using the MCNP6 transport code. While the spatial distribution of the flux was found to be in reasonable qualitative agreement, the MCNP total flux predictions were systematically lower than the experimental results by about 29%, on average. The discrepancy is largely attributed to the assumption of fresh fuel in the core in the MCNP model. The results could be potentially improved by considering the burnup level of the fuel elements.

Based on the experimentally measured and calculated flux values, and Monte Carlo simulations of alpha spectra, it appears that an NDP apparatus at the MSTR beam port would be of practical use for characterizing certain boron containing materials within a reasonable acquisition time and with low uncertainty from counting statistics. Such an apparatus would likely be limited for trace elemental analysis in MSTR's current core

configuration. Increasing the beam port flux, however, should be possible by reverting to an older core configuration. Future work will be needed to repeat the simulations for other commonly analyzed element such as Li.

A concept for coupling Neutron Depth Profiling (NDP) with Particle Induced X-Ray Emission (PIXE) to provide additional elemental depth profiling capabilities to a traditional thermal neutron-based NDP instrument is presented. The simple addition of an X-ray spectroscopy detector in coincidence with the NDP charged particle spectroscopy system are relatively minor modifications that could be used to gain the NIXE capability. Calculations involving numerical radiation transport simulations and an analytical model describing X-ray production using tabulated ionization cross sections and fluorescence data were used to emulate K-shell X-ray production as a function of coincident alpha particle energy. Monte Carlo simulations in MCNP6 were used to calculate the alpha energy spectrum. The expected and calculated depth profiles were found to be in good agreement though the ability to perform accurate and precise measurements is expected to be constrained by a combination of neutron flux, desired depth resolution, acquisition time and sample composition. Future computational and experimental work will be needed to better understand the technical limitations with such a technique as well as to demonstrate it with real data.

Neutron Depth Profiling spectra from randomly generated non-uniform samples containing boron were simulated in MCNP6 . The randomly generated sample spectra were used to train an Artificial Neural Network. The depth profile of boron within NIST standard SRM-2137, was used to demonstrate the performance of the NDP system and validate the use of MCNP for these simulations. The determined depth profiles of  $^{10}\text{B}$

obtained using the ANN processing method and the traditional method with stopping tables both showed good agreement with the reference profile provide from NIST. Both methods had comparable accuracy. With additional training the ANN may possess several advantages over the traditional processing method.

Despite being nearly 50 years old, NDP is a technique with untapped potential. It has mainly been limited to boron analysis in semiconductors and lithium analysis in battery materials. However, by exploiting the secondary radiations that are naturally emitted during an NDP measurement, additional complimentary information about a specimen can be obtained. This work adds to and advances NDP to extend its range of analytical capabilities.

**BIBLIOGRAPHY**

1. Welsh, J., et al., Studies in neutron depth profiling. *Journal of radioanalytical and nuclear chemistry*, 1993. 167(1): p. 111-119.
2. Gautier, B., et al., Deconvolution of SIMS depth profiles of boron in silicon. *Surface and interface analysis*, 1996. 24(11): p. 733-745.
3. Ünlü, K. and B.W. Wehring, Neutron depth profiling applications at The University of Texas research reactor. *Journal of Radioanalytical and Nuclear Chemistry*, 1997. 217(2): p. 273-278.
4. Ziegler, J., G. Cole, and J. Baglin, Technique for determining concentration profiles of boron impurities in substrates. *Journal of Applied Physics*, 1972. 43(9): p. 3809-3815.
5. Vineyard, G.H. and L. Falicov, National facilities for research in the physics of condensed matter. *Review of scientific instruments*, 1984. 55(4): p. 620-630.
6. Turkoglu, D., et al., Characterization of a new external neutron beam facility at the Ohio State University. *Journal of Radioanalytical and Nuclear Chemistry*, 2012. 291(2): p. 321-327.
7. Çetiner, S., K. Ünlü, and R. Downing, Development of time-of-flight neutron depth profiling at Penn State University. *Journal of radioanalytical and nuclear chemistry*, 2007. 271(2): p. 275-281.
8. Mulligan, P., L. Cao, and D. Turkoglu, A multi-detector, digitizer based neutron depth profiling device for characterizing thin film materials. *Review of Scientific Instruments*, 2012. 83(7): p. 073303.
9. Richardson, B., et al., Modeling and validation of approach to criticality and axial flux profile experiments at the Missouri S&T Reactor (MSTR). *Nuclear Engineering and Design*, 2012. 245: p. 55-61.
10. Akyurek, T., et al., Portable spectroscopic fast neutron probe and  $^3\text{He}$  detector dead-time measurements. *Progress in Nuclear Energy*, 2016. 92: p. 15-21.
11. Sinha, V., A. Srivastava, and H.K. Lee, A novel method for NDT applications using NXCT system at the Missouri University of Science & Technology. *Nuclear Instruments and Methods in Physics Research Section A: Accelerators, Spectrometers, Detectors and Associated Equipment*, 2014. 750: p. 43-55.

12. Grant, E., et al., Internet accessible hot cell with gamma spectroscopy at the Missouri S&T nuclear reactor. *Nuclear Engineering and Design*, 2011. 241(8): p. 3306-3316.
13. MSTR, 2012–2013. Annual Progress Report for the Missouri University of Science and Technology Reactor. Nuclear Regulatory Commission.
14. Bonzer, W. and C. Carroll, Safety Analysis Report for The Missouri University of Science and Technology Reactor-Revision 2. Rolla, MO, 2008.
15. Hevesy, G.v. and H. Levi, Action of slow neutrons on rare earth elements. *Nature*, 1936. 137(3457): p. 185.
16. Soete, D. de, Gijbels, R., & Hoste, J. (1972). Neutron activation analysis. London: Wiley-Interscience.
17. Knoll, G.F., Radiation detection and measurement. 2010: John Wiley & Sons.
18. N. Tsoulfanidis, Measurement and Detection of Radiation, Third Edition. CRC Press, Nov. 2013.
19. G. Gilmore, Practical Gamma-ray Spectroscopy. John Wiley & Sons, Sept. 2011.
20. <http://nmi3.eu/neutron-research/techniques-for-chemical-analysis.html>, The NMI3 information portal. Accessed: June 2017.
21. William, D.E. and E.V. Diane, Radiochemistry and Nuclear Methods of Analysis. 1991, John Wiley and Sons Inc.
22. Marsland, S., Machine learning: an algorithmic perspective. 2011: Chapman and Hall/CRC.
23. McCulloch, W.S. and W. Pitts, A logical calculus of the ideas immanent in nervous activity. *The bulletin of mathematical biophysics*, 1943. 5(4): p. 115-133.
24. Sha, W. and K. Edwards, The use of artificial neural networks in materials science based research. *Materials & design*, 2007. 28(6): p. 1747-1752.
25. Bender, E.A., Mathematical methods in artificial intelligence. 1996.
26. Shahin, M.A., H.R. Maier, and M.B. Jaksa, Data division for developing neural networks applied to geotechnical engineering. *Journal of Computing in Civil Engineering*, 2004. 18(2): p. 105-114.

27. Thawornwong, S. and D. Enke, The adaptive selection of financial and economic variables for use with artificial neural networks. *Neurocomputing*, 2004. 56: p. 205-232.
28. Ceryan, N., U. Okkan, and A. Kesimal, Prediction of unconfined compressive strength of carbonate rocks using artificial neural networks. *Environmental earth sciences*, 2013. 68(3): p. 807-819.
29. Demuth, H.B., et al., *Neural network design*. 2014: Martin Hagan.
30. Gurney, K., *An introduction to neural networks*. 2014: CRC press.
31. Haykin, S.S., et al., *Neural networks and learning machines*. Vol. 3. 2009: Pearson Upper Saddle River.
32. Møller, M.F., A scaled conjugate gradient algorithm for fast supervised learning. *Neural networks*, 1993. 6(4): p. 525-533.
33. Rihawy, M. and D. Halloum, Characterization and application of in-vacuum PIXE/EBS system for the direct elemental analysis of thick solid biological samples. *Applied Radiation and Isotopes*, 2018. 133: p. 14-21.
34. Antoszewska, M., et al., PIXE from thin films and amorphous alloys induced by medium energy heavy ions. *Nuclear Instruments and Methods in Physics Research Section B: Beam Interactions with Materials and Atoms*, 2013. 310: p. 27-31.
35. Tsuboi, Y., et al., Characterization of thin films for biomaterial applications using PIXE and RBS. *Nuclear Instruments and Methods in Physics Research Section A: Accelerators, Spectrometers, Detectors and Associated Equipment*, 1994. 353(1-3): p. 597-600.
36. Antoszewska-Moneta, M., R. Brzozowski, and M. Moneta, Modification of thin films induced by slow heavy ions analysed with PIXE and SRIM. *The European Physical Journal D*, 2015. 69(3): p. 77.
37. Santos, M.S., et al., PIXE analysis applied to characterized water samples. 2011.
38. Calligaro, T., PIXE in the study of archaeological and historical glass. *X-Ray Spectrometry: An International Journal*, 2008. 37(2): p. 169-177.
39. Müller, K., R. Henkelmann, and H. Boroffka, The determination of low dose boron implanted concentration profiles in silicon by the  $(n, \alpha)$  reaction. *Nuclear Instruments and Methods*, 1975. 129(2): p. 557-559.

40. Biersack, J., et al., The use of neutron induced reactions for light element profiling and lattice localization. *Nuclear instruments and Methods*, 1978. 149(1-3): p. 93-97.
41. Downing, R., et al., Neutron depth profiling at the National Bureau of Standards. *Nuclear Instruments and Methods in Physics Research*, 1983. 218(1-3): p. 47-51.
42. Downing, R., et al., Neutron depth profiling: overview and description of NIST facilities. *Journal of research of the National Institute of Standards and Technology*, 1993. 98(1): p. 109.
43. Downing, R., J. Maki, and R. Fleming, Analytical applications of neutron depth profiling. *Journal of Radioanalytical and Nuclear Chemistry*, 1987. 112(1): p. 33-46.
44. Biersack, J. and D. Fink, Implantation of Boron and Lithium in Semiconductors and Metals, in *Ion Implantation in Semiconductors*. 1975, Springer. p. 211-218.
45. Ünlü, K. and B.W. Wehring, Neutron depth profiling at the University of Texas. *Nuclear Instruments and Methods in Physics Research Section A: Accelerators, Spectrometers, Detectors and Associated Equipment*, 1994. 353(1-3): p. 402-405.
46. Whitney, S., et al., Advancement of light-element neutron depth profiling at the University of Texas. *Journal of Radioanalytical and Nuclear Chemistry*, 2008. 276(1): p. 257-261.
47. Chen-Mayer, H.H., G.P. Lamaze, and S.K. Satija. Characterization of BPSG films using Neutron Depth Profiling and Neutron/X-ray Reflectometry. in *AIP Conference Proceedings*. 2001. AIP.
48. Lamaze, G.P., et al., Neutron depth profiling with the new NIST cold neutron source. *Surface and interface analysis*, 1997. 25(3): p. 217-220.
49. Çetiner, S., K. Ünlü, and R. Downing, Development and applications of time-of-flight neutron depth profiling (TOF-NDP). *Journal of Radioanalytical and Nuclear Chemistry*, 2008. 276(3): p. 623-630.
50. Schweikert, E. and J. Welsh, New approaches for neutron depth profiling. *Journal of radioanalytical and nuclear chemistry*, 1994. 180(2): p. 255-262.
51. Tun, Z., et al., Cold-neutron depth profiling as a research tool for the study of surface oxides on metals Special Issue on Neutron Scattering in Canada. *Canadian Journal of Physics*, 2010. 88(10): p. 751-758.

52. Vacík, J., et al., Pulse-shape discrimination in neutron depth profiling technique. *Nuclear Instruments and Methods in Physics Research Section B: Beam Interactions with Materials and Atoms*, 1998. 142(3): p. 397-401.
53. Havranek, V., et al., Neutron depth profiling by large angle coincidence spectrometry. *Nuclear Instruments and Methods in Physics Research Section B: Beam Interactions with Materials and Atoms*, 1993. 73(4): p. 523-530.
54. Lamaze, G.P., et al., In situ measurement of lithium movement in thin film electrochromic coatings using cold neutron depth profiling. *Surface and interface analysis*, 1999. 27(7): p. 644-647.
55. Whitney, S., S. Biegalski, and G. Downing, Benchmarking and analysis of <sup>6</sup>Li neutron depth profiling of lithium ion cell electrodes. *Journal of radioanalytical and nuclear chemistry*, 2009. 282(1): p. 173.
56. Nagpure, S.C., et al., Neutron depth profiling technique for studying aging in Li-ion batteries. *Electrochimica Acta*, 2011. 56(13): p. 4735-4743.
57. Liu, D.X., et al., In situ quantification and visualization of lithium transport with neutrons. *Angewandte Chemie International Edition*, 2014. 53(36): p. 9498-9502.
58. Rosenblatt, F., The perceptron: a probabilistic model for information storage and organization in the brain. *Psychological review*, 1958. 65(6): p. 386.
59. Nguyen, D. and B. Widrow. Improving the learning speed of 2-layer neural networks by choosing initial values of the adaptive weights. in 1990 IJCNN International Joint Conference on Neural Networks. 1990. IEEE.
60. Ghal-Eh, N., P. Ahmadi, and V. Doost-Mohammadi, A quantitative PGNAA study for use in aqueous solution measurements using Am–Be neutron source and BGO scintillation detector. *Nuclear Instruments and Methods in Physics Research Section A: Accelerators, Spectrometers, Detectors and Associated Equipment*, 2016. 808: p. 123-127.
61. Skrypnyk, A.I., artificial neural networks in gamma-spectrum based radionuclide identification. *Telecommunications and Radio Engineering*, 2016. 75(12).
62. Ferreira, F., V. Crispim, and A. Silva, Detection of drugs and explosives using neutron computerized tomography and artificial intelligence techniques. *Applied Radiation and Isotopes*, 2010. 68(6): p. 1012-1017.
63. Varley, A., et al., Development of a neural network approach to characterise <sup>226</sup>Ra contamination at legacy sites using gamma-ray spectra taken from boreholes. *Journal of environmental radioactivity*, 2015. 140: p. 130-140.

64. Medhat, M., Artificial intelligence methods applied for quantitative analysis of natural radioactive sources. *Annals of Nuclear Energy*, 2012. 45: p. 73-79.
65. Kardan, M., et al., Fast neutron spectra determination by threshold activation detectors using neural networks. *Radiation measurements*, 2004. 38(2): p. 185-191.
66. Doostmohammadi, V., D. Sardari, and A. Nasrabadi, Combined application of Monte Carlo method and neural networks to simulate qualitative prompt gamma neutron activation analysis. *Journal of radioanalytical and nuclear chemistry*, 2009. 283(2): p. 403-407.
67. Zadeh, E.E., et al., Application of artificial neural network in precise prediction of cement elements percentages based on the neutron activation analysis. *The European Physical Journal Plus*, 2016. 131(5): p. 167.
68. Sang, H.-f., et al., Detection of element content in coal by pulsed neutron method based on an optimized back-propagation neural network. *Nuclear Instruments and Methods in Physics Research Section B: Beam Interactions with Materials and Atoms*, 2005. 239(3): p. 202-208.
69. Roentgen, W., *Sitzungsber. der Wurgburgev Physik-Medic, Gesellsch, Jahrg. 1895. Ann. Dev. Phys*, 1898. 64(1).
70. Birks, L., et al., Excitation of characteristic x rays by protons, electrons, and primary x rays. *Journal of Applied physics*, 1964. 35(9): p. 2578-2581.
71. Chadwick, J., J. Chadwick, *Phil. Mag.* 25, 193 (1913). *Phil. Mag.*, 1913. 25: p. 193.
72. Khan, J., D. Potter, and R. Worley, Proposed Method for Microgram Surface Density Measurements by Observation of Proton-Produced X Rays. *Journal of Applied Physics*, 1966. 37(2): p. 564-567.
73. Van Rinsvelt, H., R. Lear, and W. Adams, Human diseases and trace elements: Investigation by proton-induced x-ray emission. *Nuclear Instruments and Methods*, 1977. 142(1-2): p. 171-180.
74. Johansson, T.B., R. Akselsson, and S.A. Johansson, Proton-induced x-ray emission spectroscopy in elemental trace analysis, in *Advances in X-ray Analysis*. 1972, Springer. p. 373-387.
75. Johansson, T.B., R. Akselsson, and S.A. Johansson, X-ray analysis: elemental trace analysis at the 10– 12 g level. *Nuclear Instruments and Methods*, 1970. 84(1): p. 141-143.

76. Watson, R., J. Sjurseth, and R. Howard, An investigation of the analytical capabilities of X-ray emission induced by high energy alpha particles. *Nuclear Instruments and Methods*, 1971. 93(1): p. 69-76.
77. Flocchini, R., et al., Sensitivity versus target backings for elemental analysis by alpha excited X-ray emission. *Nuclear Instruments and Methods*, 1972. 100(3): p. 397-402.
78. Garcia, J., R. Fortner, and T. Kavanagh, Inner-shell vacancy production in ion-atom collisions. *Reviews of Modern Physics*, 1973. 45(2): p. 111.
79. Johansson, S.A. and T.B. Johansson, Analytical application of particle induced X-ray emission. *Nuclear Instruments and Methods*, 1976. 137(3): p. 473-516.
80. Adelfang, P. and I.G. Ritchie. Overview of the status of research reactors worldwide. in *The 25th international meeting on reduced enrichment for research and test reactors (RERTR)*, Chicago, Illinois. 2003.
81. Shu, F., V. Ramakrishnan, and B.P. Schoenborn, Enhanced visibility of hydrogen atoms by neutron crystallography on fully deuterated myoglobin. *Proceedings of the National Academy of Sciences*, 2000. 97(8): p. 3872-3877.
82. Li, R.-d., et al., Development of neutron depth profiling at CMRR. *Nuclear Instruments and Methods in Physics Research Section A: Accelerators, Spectrometers, Detectors and Associated Equipment*, 2015. 788: p. 1-4.
83. Bencardino, R., G. Giorginis, and D. Sapundjiev, Preparation of 6 LiF deposits and characterisation via Monte Carlo simulations and Neutron Depth Profiling. *Nuclear Instruments and Methods in Physics Research Section A: Accelerators, Spectrometers, Detectors and Associated Equipment*, 2013. 709: p. 72-75.
84. Robinson, J.A., M.R. Hartman, and S.R. Reese, Design, construction and characterization of a prompt gamma activation analysis facility at the Oregon State University TRIGA® reactor. *Journal of radioanalytical and nuclear chemistry*, 2010. 283(2): p. 359-369.
85. Babcock, E., et al., Using neutron methods SANS and PGAA to study evolution of structure and composition of Alkali-doped Polybenzimidazole membranes. *Journal of Membrane Science*, 2019.
86. Micieli, D., et al., A comparative study of reconstruction methods applied to neutron tomography. *Journal of Instrumentation*, 2018. 13(06): p. C06006.
87. Hindasyah, A., D. Sudiana, and D. Gunawan, A Novel Technique for Removal of High Density White Spot Noise from Digital Neutron Radiographic Images. *Atom Indonesia*, 2018. 44(3).

88. Moxom, J., A.G. Hathaway, and A.I. Hawari. Out of core testing of the North Carolina State University PULSTAR reactor positron beam. in Nuclear Science Symposium Conference Record, 2007. NSS'07. IEEE. 2007. IEEE.
89. Xu, Q., et al. Positron beam facility at Kyoto University Research Reactor. in Journal of Physics: Conference Series. 2014. IOP Publishing.
90. Craft, A.E., B.A. Hilton, and G.C. Papaioannou, Characterization of a Neutron Beam Following Reconfiguration of the Neutron Radiography Reactor (NRAD) Core and Addition of New Fuel Elements. Nuclear Engineering and Technology, 2016. 48(1): p. 200-210.
91. Bărbos, D., et al. The prompt gamma neutron activation analysis facility at ICN—Pitesti. in AIP Conference Proceedings. 2008. AIP.
92. Révay, Z., et al., Construction and characterization of the redesigned PGAA facility at The University of Texas at Austin. Nuclear Instruments and Methods in Physics Research Section A: Accelerators, Spectrometers, Detectors and Associated Equipment, 2007. 577(3): p. 611-618.
93. Morgan, S.W., J.C. King, and C.L. Pope, Beam characterization at the neutron radiography reactor. Nuclear Engineering and Design, 2013. 265: p. 639-653.
94. Greenberg, R.R., P. Bode, and E.A.D.N. Fernandes, Neutron activation analysis: a primary method of measurement. Spectrochimica Acta Part B: Atomic Spectroscopy, 2011. 66(3): p. 193-241.
95. ASTM E720 – 16, 2016. Standard Guide for Selection and Use of Neutron Sensors for Determining Neutron Spectra Employed in Radiation-Hardness Testing of Electronics. ASTM International, West Conshohocken, PA. [www.astm.org](http://www.astm.org).
96. ASTM E721-16, 2016. Standard Guide for Determining Neutron Energy Spectra from Neutron Sensors for Radiation-Hardness Testing of Electronics. ASTM International, West Conshohocken. [www.astm.org](http://www.astm.org).
97. McElroy, W., et al., A computer-automated iterative method for neutron flux spectra determination by foil activation. 1967, Air Force Weapons Laboratory.
98. ASTM E262 – 13, 2013. Standard Test Method for Determining Thermal Neutron Reaction Rates and Thermal Neutron Fluence Rates by Radioactivation Techniques1. ASTM International, West Conshohocken, PA. [www.astm.org](http://www.astm.org).
99. Baum, E.M., Knox, H.D., Miller, T.R., 2002. Nuclides and Isotopes: Chart of the Nuclides. KAPL.

100. Fleming, R.F., Neutron self-shielding factors for simple geometries. *International Journal of Applied Radiation and Isotopes*, 1982. 33(11): p. 1263-1268.
101. Lindstrom, R.M. and R.F. Fleming, Neutron self-shielding factors for simple geometries, revisited. *Chem. Anal*, 2008. 53: p. 855-859.
102. Chadwick, M., et al., ENDF/B-VII. 1 nuclear data for science and technology: cross sections, covariances, fission product yields and decay data. *Nuclear data sheets*, 2011. 112(12): p. 2887-2996.
103. ASTM E181 – 17, 2017. *Standard Test Methods for Detector Calibration and Analysis of Radionuclides*. ASTM International, West Conshohocken, PA. [www.astm.org](http://www.astm.org).
104. Pelowitz, D., MCNP6 user's manual version 1.0 Report LA-CP-13-00634 Los Alamos National Laboratory. 2013.
105. Goorley, T., et al., Initial MCNP6 release overview. *Nuclear Technology*, 2012. 180(3): p. 298-315.
106. Ziegler, J.F., M.D. Ziegler, and J.P. Biersack, SRIM—The stopping and range of ions in matter (2010). *Nuclear Instruments and Methods in Physics Research Section B: Beam Interactions with Materials and Atoms*, 2010. 268(11): p. 1818-1823.
107. Haykin, S., *Neural networks: a comprehensive foundation*, 1999. Mc Millan, New Jersey, 2010: p. 1-24.
108. Smith, M., *Neural networks for statistical modeling*. 1993: Thomson Learning.
109. Ziegler, J.F., SRIM-2003. *Nuclear instruments and methods in physics research section B: Beam interactions with materials and atoms*, 2004. 219: p. 1027-1036.
110. Wang, Y. and M.A. Nastasi, *Handbook of modern ion beam materials analysis*. 2009: Materials Research Society Warrendale, PA.
111. Paul, H. and O. Bolik, Fitted empirical reference cross sections for K-shell ionization by alpha particles. *Atomic data and nuclear data tables*, 1993. 54(1): p. 75-131.
112. Hubbell, J., et al., A review, bibliography, and tabulation of K, L, and higher atomic shell x-ray fluorescence yields. *Journal of Physical and Chemical Reference Data*, 1994. 23(2): p. 339-364.

113. Park, B.G., G.M. Sun, and H.D. Choi, Development of cold neutron depth profiling system at HANARO. Nuclear Instruments and Methods in Physics Research Section A: Accelerators, Spectrometers, Detectors and Associated Equipment, 2014. 752: p. 20-26.

## VITA

Mubarak Mohammed Albarqi received his BS degree in electrical engineering in May 2009 from Umm Alqura University in Makkah, Saudi Arabia. He earned his Master of Science in Nuclear Engineering from Missouri University of Science and Technology in December 2014. He earned his Doctor of Philosophy in Nuclear Engineering from Missouri University of Science and Technology in in July 2019.